A Multimodal Micro Air Vehicle for Autonomous Flight in Near-Earth Environments

A Thesis

Submitted to the Faculty

of

Drexel University

by

William Edward Green

in partial fulfillment of the

requirements for the degree

of

Doctor of Philosophy in Mechanical Engineering

May 2007

Acknowledgments

There are many people I would like to thank for their never-ending support throughout my long journey as a doctoral student. First and foremost, I'd like to express my sincere appreciation to my Ph.D. advisor, Dr. Paul Oh, for his guidance, support and wisdom. Dr. Oh was always willing to meet individually whether it was to guide me in the right research direction, fine-tune one of my conference papers or fellowship applications, or approve a relentless supply of funds to purchase various sensors, electronics, and other parts which ultimately led to the success of my research. In addition, I would like to thank my thesis advisory committee. Dr. Bor-Chin Chang, Dr. Alan Lau, Dr. Ajmal Yousuff, and Dr. Andrew Hicks have all provided much support and invaluable advice which have steered me along the path towards graduation.

I would like to extend special thanks to Dr. Geoffrey Barrows for his advice, support, and sincere willingness to help with my optic flow experiments. I am equally as grateful for all of the quaternion knowledge and wisdom Noel Hughes has shared with me over the last year. Finally, I would like to thank Brian DiCinti for his expert piloting skills and willingness to help with experiments whenever asked. Without the support of these people, a lot of my research accomplishments would not have been possible.

I would like to thank the faculty and staff of the Mechanical Engineering and Mechanics (MEM) Department and College of Engineering. I want to extend special thanks to Dr. Mun Choi, who always put my concerns and the concerns of all graduate students as a top priority. In addition, he has provided a lot of support and motivation throughout my time at Drexel. I would also like to thank Dr. Alan Lau for his guidance, especially in the last few months. I would like to extend special thanks to Kathie Donahue who, despite the turnstile of people constantly arriving in front of

her desk, was always willing to help with any of my concerns. Finally, I would like to thank the rest of the MEM staff (current and former) including Jessica Atchison, Colleen Rzucidlo, Joanne Ferroni, Stephanos Karas, George Ciarrocchi, and anyone else I may have forgotten.

I am also grateful for all the help and support of my friends and colleagues in the MEM Department. In particular, a lot of my research was made possible due to the assistance of members from the Drexel Autonomous Systems Laboratory (DASL). I would like to equally thank Vefa Narli, Keith Sevcik, and Rares Stanciu for all of their excellent advice and ideas whenever I came across a research roadblock. In addition, I would like to thank Shrey Shah and Jason Collins for their assistance in the majority of my initial experiments. I am grateful to all of them for taking time out of their busy schedules to lend a hand. I would also like to thank the rest of my colleagues in DASL as well as the MEM department, namely Kate Allen, Karthik Bala, Kivilcim Buyukhatipoglu, Mike Foster, Shailesh Gangoli, Connie Gomez, Ashu Gupta, James Hing, Mert Sasoglu, Lauren Shor, and Greg Tholey. I will miss everyone at Drexel and will remain forever in debt to the people and the university.

I would like to thank my extended family and friends for all of their support throughout my graduate studies. I would especially like to thank my mom and dad who have endured the backlashes of interaction with me after spending countless hours in the lab. Their endless love and encouragement are responsible for all of the successes in my life. I would also like to thank my sister, Lori, and her husband, Brian, for their love and support. I am also grateful to my friends outside of Drexel for forcing me to think about things other than unmanned aircraft.

Last but certainly not least, I would like to thank my fiance, Blake, for her love, support, and patience especially over the last (very demanding) year. Her constant encouragement and faith in me have helped get me to the point I am today.

Table of Contents

List of Tables

List of Figures

Abstract

A Multimodal Micro Air Vehicle for Autonomous Flight in Near-Earth Environments

William Edward Green

Advisor: Paul Yu Oh, Ph.D.

Reconnaissance, surveillance, and search-and-rescue missions in near-Earth environments such as caves, forests, and urban areas pose many new challenges to command and control (C2) teams. Of great significance is how to acquire situational awareness when access to the scene is blocked by enemy fire, rubble, or other occlusions. Small bird-sized aerial robots are expendable and can fly over obstacles and through small openings to assist in the acquisition and distribution of intelligence. However, limited flying space and densely populated obstacle fields requires a vehicle that is capable of hovering, but also maneuverable. A secondary flight mode was incorporated into a fixed-wing aircraft to preserve its maneuverability while adding the capability of hovering. An inertial measurement sensor and onboard flight control system were interfaced and used to transition the hybrid prototype from cruise to hover flight and sustain a hover autonomously. Furthermore, the hovering flight mode can be used to maneuver the aircraft through small openings such as doorways. An ultrasonic and infrared sensor suite was designed to follow exterior building walls until an ingress route was detected. Reactive control was then used to traverse the doorway and gather reconnaissance. Entering a dangerous environment to gather intelligence autonomously will provide an invaluable resource to any C2 team. The holistic approach of platform development, sensor suite design, and control serves as the philosophy of this work.

1. Introduction

1.1 Motivation

Unmanned Aerial Vehicles (UAVs) such as the Predator and Global Hawk have been used extensively in Bosnia since 1995 and more recently in Iraq and Afghanistan for intelligence, surveillance and reconnaissance (ISR) gathering (see Figure 1.1a-b). These large-scale UAVs fly at high altitudes (e.g. 8-20 kms) in vast open airspace. Typically, flight routes are preprogrammed Global Positioning System (GPS) waypoints and can be modified and updated in mid-flight. The success of these UAV drones resulted in a congressional mandate in 2001 which stated that one-third of all deep strike aircraft are to be unmanned by the year 2010. In addition, UAV support at the tactical level seemed like a promising extension of the Predator and Global Hawk programs.

Providing support at the tactical level meant that the platform size of their predecessors had to be scaled down dramatically such that it could be transported with minimal effort. Such a platform, when equipped with a wireless imaging device, could be rapidly deployed to provide close range (e.g. over-the-hill) surveillance and reconnaissance in real-time. AeroVironment's Pointer UAV is one of the most successful platforms of this size regime (see Figure 1.1c). With a 2.75 meter wingspan and a gross takeoff weight of 4.3 kg, the Pointer UAV is hand-launched and has an endurance of ninety minutes. Initially controlled as a remotely piloted vehicle, it has since been upgraded (and renamed Puma) to autonomously follow preprogrammed waypoint routes. Even though the UAV flies at extremely low altitudes (e.g. 30-152 meters), the flight control system (FCS) does not possess any collision avoidance capabilities; its only responsibilities are to stabilize the aircraft and keep it on course with

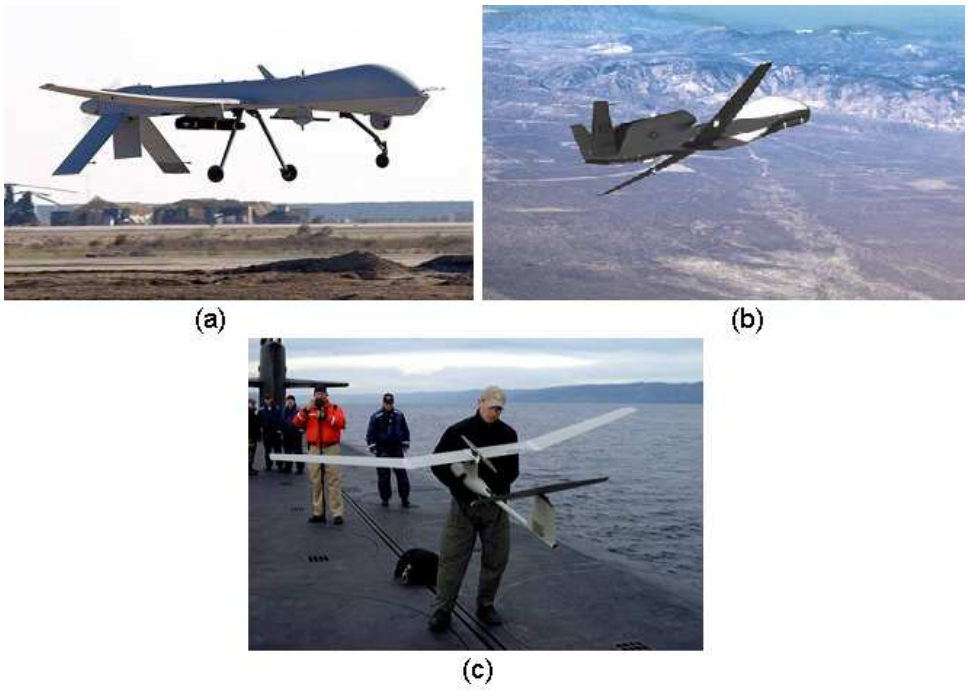

Figure 1.1: (a) Northrop Grumman's Global Hawk high altitude UAV. Reprinted from *www.af.mil*. (b) General Atomics' Predator medium altitude UAV. Reprinted from *www.af.mil*. (c) AeroVironment's Pointer UAV, used for close range reconnaissance. Reprinted from *www.afa.org/magazine/feb2006*.

its predefined target. However, the success of miniature UAVs, or mini-UAVs, like the Pointer in conjunction with recent homeland security missions have resulted not only in a paradigm shift in flight control system responsibilities, but also in platform requirements.

Homeland security and disaster mitigation efforts leading to the paradigm shift have been occurring in unforeseen environments which include caves, tunnels, forests, cities, and even inside urban structures. Ground-based robots have had many successes in these closed quarter environments [38], however, they move slowly, have trouble traversing rugged terrain, and can still put the operator at risk. As such, there is a need for mini-UAV platforms to be scaled down even further to maneuver through cluttered terrain. Originally defined by the Defense Advanced Research

Projects Agency (DARPA) as being less than 15 cm in length, width, and height, the term Micro Air Vehicle (MAV) has since evolved to include platforms ranging from insect-sized to bird-sized. MAVs can be designed for compactness (e.g. capable of fitting in a single backpack) and maneuverability to provide surveillance and reconnaissance in more cluttered environments. However, their small size imposes a limit on payload capacity. This makes autonomous attitude regulation and navigation extremely challenging tasks.

To climb the ladder of autonomy, the flight control system must first be able to regulate the aircraft's attitude using feedback from inertial sensors. In addition, it must process proximity sensor data to detect imminent collisions and maneuver the aircraft around them. With faint or nonexistent GPS signals, limited payload capacities, and densely populated obstacle fields, such tasks require unconventional platforms and sensing technologies to achieve them autonomously.

1.2 Preliminary Design Specifications

Complete UAV autonomy in near-Earth environments requires a novel platform in conjunction with sophisticated sensing, control, and collision avoidance methodologies. The platform's size, weight, payload capacity, flight speed, maneuverability, and endurance all have significant roles when designing a vehicle that can fly through cluttered areas. Sensors have to be small, lightweight, and robust to changing environmental conditions such as lighting levels.

1.2.1 Airframe

When choosing between different platform configurations such as fixed or rotary wing, the flying environment is of primary importance. Near-Earth environments include urban areas, caves, and tunnels and thus a vehicle is needed that can fly both

outdoors and in closed quarters. Therefore, the platform must be small enough to fly through narrow openings such as doorways [1]. As such, the platform's width in its primary flight configuration should be less than this baseline dimension. For fixed wing aircraft and helicopters, this results in a wingspan and rotor diameter of under 0.9 meters, respectively.

The platform's cruise velocity and weight are also critical parameters. For closed quarters, a cruise velocity of 2 m/s (or less) was desired based on sensor performance and aircraft maneuverability. That is, with a collision avoidance maneuver estimated to take one second, a sensor would have to detect an approaching obstacle two meters in advance. This was assumed to be reasonable since most small scale ultrasonic (e.g. MaxSonar EZ-1) and infrared (e.g. Sharp GP2Y0A02YK) proximity sensors have maximum ranging capabilities close to two meters. Furthermore, the MAV must have enough substance such that it is controllable in windy conditions (i.e. 5-10 m/s).

Flight characteristics such as maneuverability and endurance are equally as important when selecting a MAV platform. When entering hostile or structurally unsafe environments, a *dash* capability is desired in order to avoid enemy fire or falling debris. Additionally, the MAV will most likely be launched from a remote location and thus will require high endurance capabilities.

The airframe design specifications laid out thus far do not reveal an optimal platform configuration. For example, maneuverability and endurance are well known characteristics of fixed wing aircraft. However, designing a fixed wing MAV to fly at speeds of less than 2 m/s and also being capable of flying outdoors in windy conditions may not be feasible. A helicopter or other rotary wing vehicle has the ability to hover but because the lift is provided solely by the main rotor, the endurance is

[1] A standard doorway is 0.9 meters in width and will be used as a baseline.

less than their fixed wing counterparts. One possible solution is a hybrid platform which incorporates the advantages between fixed and rotary wing vehicles, and would meet all design specifications. For example, a fixed wing airframe with a secondary flight mode for hovering preserves the endurance and maneuverability characteristics of fixed wing aircraft while incorporating the advantages of helicopters for flight in cluttered spaces.

1.2.2 Sensing

Upon designing a platform which is capable of flying in near-Earth environments, different sensing techniques will be investigated for autonomous flight. The first is the sensing for low level attitude control. Before high level control strategies such as navigation and collision avoidance can be looked at, the aircraft must be capable of autonomous attitude regulation. The constraint on the size of the platform also imposes a limitation on the payload capacity. Therefore, attitude measurement must be performed with a lightweight sensor, such as Micro-Electro-Mechanical Systems (MEMs) gyros and accelerometers, and be robust to drift vulnerabilities. In addition to attitude regulation, altitude hold in the absence of GPS will also be examined.

For high-level sensing, biomimetic principles will be investigated. Flying insects and bats perform a variety of tasks in complex environments by using their natural sensing capabilities. Flying insects make heavy use of vision, especially optic flow, for perceiving the environment [15]. Optic flow refers to the apparent movement of texture in the visual field relative to the insect's velocity. In comparison, bats emit ultrasonic pulses to determine the distance to nearby obstacles and other bats when flying in and around caves [44]. With optic flow and ultrasonic sensing, efficient and robust navigational sensor suites for MAVs can be developed by mimicking the natural behaviors of insects and bats.

1.3 Thesis Organization

The rest of this work is organized in the following manner:

Related Work. Chapter 2 reviews the relevant platform configurations including fixed, flapping, and rotary wing vehicles as well as vertical takeoff and landing aircraft. In addition, the autonomous capabilities of each platform is described. Finally, an analysis of the research literature is performed along with a summary of this work's contributions.

Prototype Design. Chapter 3 details the fixed wing MAV prototype and describes its secondary flight mode for hovering like a helicopter. Manual operation of the aircraft, including hovering and the transition between flight modes, is also described.

Aircraft Attitude Representation. Chapter 4 presents an alternative approach to the representation of the aircraft's orientation. Conventional approaches such as Euler angles cannot be used because of the singularities present at pitch angles of ninety degrees. As such, quaternions will be used to describe the aircraft orientation and calculate the angular errors to drive the aircraft to a commanded flight mode.

Attitude Control of the Hybrid Platform. Chapter 5 details the onboard flight control system, attitude sensor, and control algorithm used in the experiments portion of this chapter. Also, the experimental procedures and results for autonomous hovering and the transition from cruise to hover flight are described. Finally, flight data is presented and analyzed during each experiment.

Sensing and Control in Near-Earth Environments. Chapter 6 discusses high-level sensing and control and details various sensors for collision avoidance and navigation in near-Earth environments. Optic flow, ultrasonic, and infrared sensors as well as laser scanners and rangers are evaluated. An infrared and ultrasonic sensor suite is developed and interfaced with the onboard flight control system. An embedded, multimodal control algorithm is used to autonomously achieve a mission in a near-

Earth environment.

Conclusions and Future Work. Finally, Chapter 7 summarizes the work presented in this thesis. Furthermore, this chapter also discusses some promising new areas of research relevant to autonomous MAV flight in near-Earth environments.

2. Related Work

In this chapter, several different platform configurations and sensing techniques are detailed including fixed, flapping, and rotary wing aircraft as well as optic flow and LADAR for collision avoidance. The chapter concludes with an analysis of the research literature.

2.1 Fixed-Wing

One of the most common platform configurations for small unmanned aircraft is a fixed wing design. Because lift is generated by the airfoil and not directly by the gas or electric powered engine, the fixed wing configuration ranks high in endurance. They are also highly maneuverable and capable of a *dash* maneuver to avoid enemy fire or falling debris in dangerous environments. There are several research groups looking at fixed wing platforms [10] [37] [27], but the most relevant to near-Earth environments are discussed in this section.

2.1.1 AeroVironment Black Widow

Funded by DARPA, AeroVironment Inc. developed the Black Widow Micro Air Vehicle (MAV) into one of the most successful prototypes of this size regime. During this time frame, there was a big push from DARPA to develop a MAV less than 15 cm in length, width, and height. Because the Black Widow was among the first vehicles of this magnitude, there was no design standards (e.g. propeller dimensions, wing configuration, airframe materials, etc.). AeroVironment therefore utilized a design process known as a Multidisciplinary Design Optimization (MDO) Matrix. The MDO, which originated in the automobile industry, was used to incorporate

Figure 2.1: AeroVironment, Inc.'s Black Widow is flown under human-control from a remote location. The human pilots the MAV by looking at raw video transmitted from the wireless camera onboard the MAV. Reprinted from [16].

many different combinations of motors, batteries, propellers, etc. and output the most optimal configuration. The net result was a 15-cm, disc-shaped, fixed wing platform which flies at speeds of 15 m/s and is capable of carrying a 2 gram wireless video camera [16]. The wireless images are fed back to the control station and viewed by the pilot to remotely fly the aircraft (see Figure 2.1).

While the design of the Black Widow was remarkable, its two gram payload capacity eliminates any possibility for additional attitude or navigational sensors. Furthermore, the 15 m/s cruise velocity makes flying in cluttered environments unrealistic.

2.1.2 NRL Micro Tactical Expendable (MITE)

The goal of the Naval Research Lab (NRL) was to develop a micro air vehicle for Navy-specific applications. They were not funded by DARPA and were therefore, not constrained by the 15 cm platform dimension. The NRL began developing prototypes of the Micro Tactical Expendable (MITE) Micro Air Vehicle in 1996 [30]. The MITE

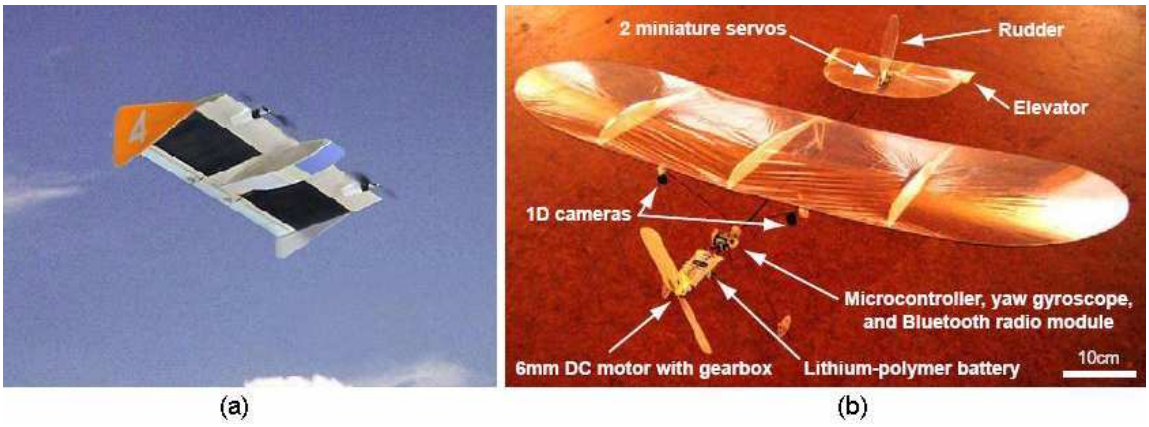

Figure 2.2: (a) NRL's MITE MAV design was one of the first MAV prototypes. Reprinted from [39]. (b) EPFL's Microflyer is designed for flight indoors and is capable of flying at speeds of less than 2 m/s. Reprinted from [63].

consisted of a dual-propeller, fixed-wing platform which after being hand-launched, had an endurance of 20 minutes at speeds of 5 to 10 m/s (see Figure 2.2a). Depending on the payload requirements of the mission, the wingspan ranged from 20 to 45 cm enabling it to carry a wireless camera up to 30 grams in weight.

In addition to developing a platform to transmit wireless video back to a remote location, the NRL began looking at autonomous MAV navigation. At that time, typical autopilot systems weighed in excess of 4 pounds which easily exceeded the payload capacity of MAVs. Unconventional approaches were required to create a sensor suite small enough for MAVs to perceive their environment. The NRL looked at different types of sensors, including vision-based methods but was unable to come up with a solution within the payload constraints of the aircraft. Additionally, while the cruise velocity was significantly less than the Black Widow, 5 m/s is still too fast for flight in near-Earth environments.

2.1.3 EPFL Microflyer

Zufferey et al from Ecole Polytechnique Federale de Lausanne (EPFL) have designed a fixed wing vehicle for flight indoors. Figure 2.2b shows the prototype which weighs 30 grams and can fly at speeds of less than 2 m/s. Its slow flight speed enabled it to maneuver around dense obstacle fields found inside urban structures. EPFL is also one of the leading research groups in the development of optic flow sensing for collision avoidance indoors. Combining optic flow sensing with their extremely lightweight platform, Zufferey et al demonstrated autonomous flight inside a gymnasium [62]. However, the experiment was performed in an artificially textured environment (i.e. alternating white and black sheets were used as walls). Walls are often homogeneous and have little texture. Although impressive, this method on its own is not sufficient in more realistic environments. Furthermore, near-Earth environments also include outdoor areas and a lightweight platform like the Microflyer cannot be controlled in any type of wind.

2.1.4 BYU UAV

Beard et al from Bringham Young University are also developing a vehicle to fly in urban areas. They are using a flying wing platform to evaluate different sensing techniques (see Figure 2.3). In [22], the flying wing was equipped with a Laser Detection and Ranging (LADAR) sensor to detect obstacles in front of the aircraft and ADNS optical flow sensors (found in optical computer mouses) for lateral collision avoidance. An experiment was described where the UAV was programmed to fly a GPS waypoint route which passed directly through an urban structure on campus. The building was detected by the LADAR sensor and the flight control system redirected the flight path around the building. This experiment was impressive, but the flying wing platform must maintain flight speeds of greater than 10 m/s to remain

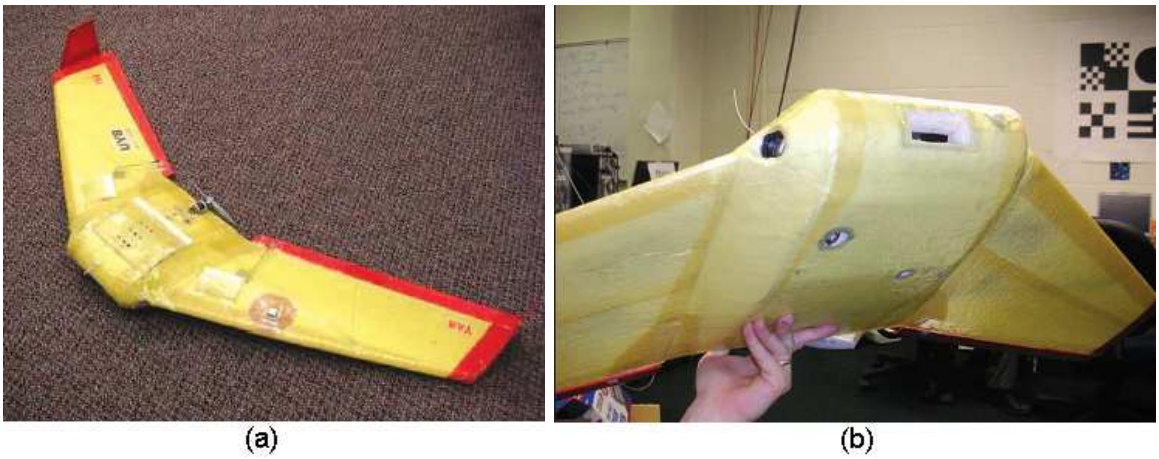

Figure 2.3: (a) BYU's flying wing MAV is used as a testing platform for autonomous collision avoidance in urban environments. (b) Optic flow and LADAR sensors are mounted on the belly of the aircraft. Reprinted from [22].

airborne. Furthermore, the platform has a wingspan of 1.2 meters and thus would not be able to fit through small openings such as doorways. Beard et al are currently looking into more suitable aircraft. They have just begun testing a fixed wing aircraft which is capable of vertical takeoff and landing (VTOL) [31].

2.2 Flapping Wing

Introducing a motor to the base of the fixed wing platform (i.e. where the wing meets the fuselage) for rotation enables the flying motion of insects and birds to be mimicked. Theoretically, the flapping motion creates more lift than a fixed wing and can be leveraged to hover the vehicle. Again there are many groups investigating this type of platform [46] [36], but only two of the most relevant are described in this section.

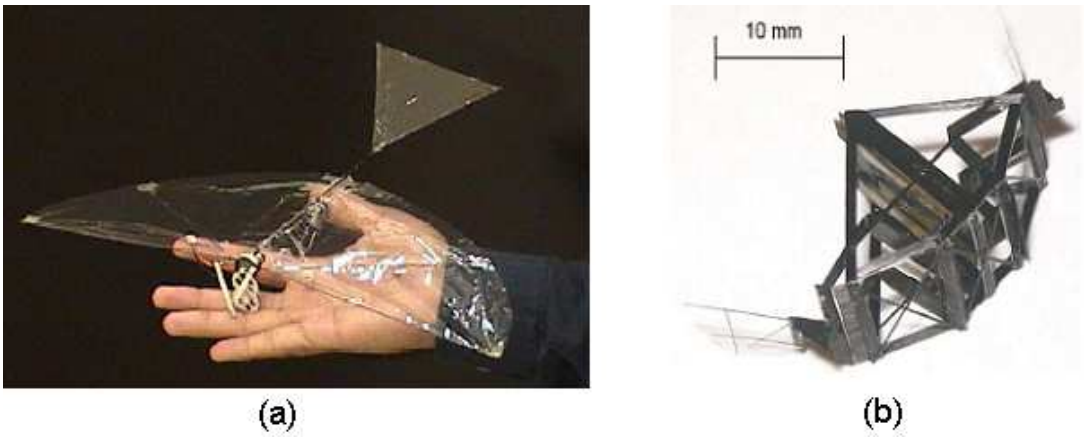

Figure 2.4: (a) The University of Delaware's Sparrow II mimics a hummingbird with its mechanism for biaxial wing rotation. Reprinted from [34]. (b) UC Berkeley's Micromechanical Flying Insect (MFI) weighs just 0.1 grams and has a wingspan of 50 mm. Reprinted from [55].

2.2.1 UD MHP

Agrawal et al out of the University of Delaware are working on a Mechanical Hummingbird Project (MHP), where the goal is to develop a flapping wing MAV that generates enough lift to hover like a hummingbird. Working towards this goal, the group has created some novel designs. Figure 2.4a shows their most successful Sparrow II prototype which has a 50 cm wingspan and weighs in at 50 grams. The simulations of their next generation MHP prototype show that the wing design generates enough lift to hover, however, the prototype has not yet been tested in tether-free flight [34]. Although the mechanism for biaxial wing rotation is quite impressive, it is currently limited to forward flight. Furthermore, they have focused their research effort solely on platform design and currently have no autonomous capabilities.

2.2.2 UCB Micromechanical Flying Insect

On an even smaller scale, Fearing et al from UC Berkeley are developing a Micromechanical Flying Insect (MFI). The idea is that hundreds of these insect-sized

robots can be released to cover more ground than a single unmanned aircraft. Figure 2.4 shows the MFI prototype which has a mass of just 0.1 grams and a wingspan of 25 mm [11]. While flight experiments have shown promising results, the MFI project still remains in the developmental stages. Furthermore, it is hard to imagine sensors at that scale which will enable autonomous flight in the near future.

2.3 Rotary Wing

Rotary wing is another traditional platform for small UAVs. Rotorcraft include everything from single rotors to quadrotors [8] [13] [14] [29] [35] [47], as well as ducted fan engines [6]. The main advantage of rotary wing aircraft is their ability to hover, however, they typically cannot fly for long periods of time because the main engine must balance the weight of the vehicle. Two notable rotary wing research groups are discussed in this section.

2.3.1 ANU X4-Flyer

Mahony et al out of the Australian National University have developed a quadrotor vehicle with vertical takeoff and landing (VTOL) capabilities (see Figure 2.5a). The X4-Flyer uses differential throttle control between the front and rear motors to control pitch and similarly between the left and right motors to control yaw [25]. Altitude is controlled by collectively increasing the thrust to all four motors. With an overall dimension of 0.7 meters, the platform is small enough to fit through a standard doorway. The aircraft was designed as a testbed for visual servoing algorithms and was used to demonstrate position-controlled hovering by servoing on a ground fiducial. While this experiment showed great promise in the absence of GPS, nothing outside the realm of visual servoing has been investigated. Furthermore, the MAV is not maneuverable and is limited by its low cruise velocity when flying outdoors.

Figure 2.5: (a) ANU's X4-Flyer is a quadrotor platform using differential thrust for attitude adjustment. Reprinted from [23]. (b) UC Berkeley's RMAX UAV is used as a testbed for implementing collision avoidance and navigation algorithms in urban environments. Reprinted from [50].

2.3.2 UCB UAV

Sastry et al from UC Berkeley have been developing control strategies for tasks such as landing [49] and navigation [50] in near-Earth environments. The platform used is a commercial off-the-shelf Yamaha RMAX helicopter and is equipped with a SICK laser scanner (see Figure 2.5b). The Yamaha RMAX is a robust platform to use as a sensor testbed, but is not capable of traversing realistic urban environments. Furthermore, UAVs which can navigate in near-Earth environments will most likely not be able to carry a 4.5 kg payload such as the SICK sensor. Smaller laser scanners such as the 160 gram Hokuyo exist, but are designed for use indoors and lack in performance when compared to its SICK counterpart [48].

2.4 Tailsitters

The concept of a fixed wing platform which can takeoff and land vertically has been around for decades. However, the transition from cruise flight to the vertical

orientation was too difficult for a human pilot. With unmanned aircraft, however, this challenge is eliminated. There are only a few research groups outside the ones discussed in this section investigating fixed wing aircraft which can transition into vertical flight as a viable platform [33]. The most well known is from the University of Sydney and is discussed below.

2.4.1 Sydney T-Wing

Stone et al from the University of Sydney have designed a fixed wing vertical take-off and landing vehicle (see Figure 2.6). The aircraft is capable of taking off vertically, performing a *stall-tumble* maneuver to transition from vertical to cruise flight, and then transitioning back to the vertical configuration to land the aircraft [56]. The prototype has a wingspan of over 2 meters, weighs 30 kg and has counter-rotating propellers on each wing to minimize the motor's reactive torque. This platform is very similar to the solution described in this thesis, however, most of the research effort at the University of Sydney has focused on platform design. It wasn't until August of 2006, that they were able to achieve an untethered autonomous hover. Furthermore, it is extremely oversized for flight in near-Earth environments.

2.5 Conclusions

After surveying the literature, it seems there are two separate communities working towards the same goal. The first group appears to be focusing on platform design such as the University of Delaware's MHP project while the other is focusing on sensing and control like in the case of the Berkeley Yamaha RMAX. Very few people are looking at the two areas in parallel. An important contribution of this thesis is to bridge the gap between the two communities. As such, the overall philosophy of this work is to take a holistic approach towards the development of a robotic aircraft

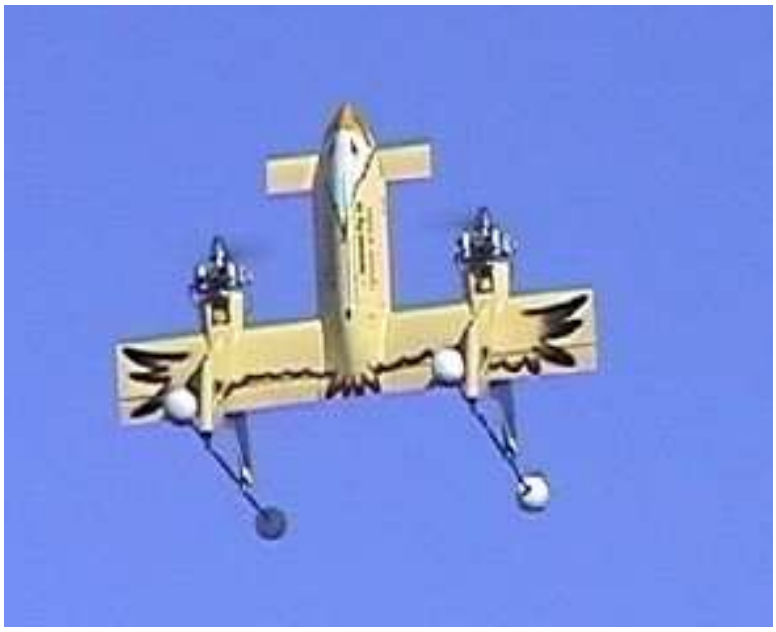

Figure 2.6: The University of Sydney's T-Wing concept vehicle combines the endurance advantages of fixed wing aircraft with the vertical takeoff and landing capabilities of helicopters. Reprinted from [56].

capable of autonomous flight in near-Earth environments. This encompasses both the development of a well suited platform as well as sensor suite and control system design. These contributions and others our outlined in this section.

2.5.1 Thesis Contributions

The work contained in this thesis spans a variety of disciplines including aerodynamic and dynamic analysis, sensor suite and control system design, and robotics and can be broken down into four major contributions:

- the development of a fixed wing micro air vehicle with a secondary flight mode for hovering (Chapter 3).
- a control methodology enabling high angle of attack maneuvers (e.g. transition from cruise to hover flight) while avoiding singularities (Chapter 4).

- the design of an onboard flight control system allowing the experimental implementation of autonomous hovering and the autonomous transition between flight modes (Chapter 5).
- mimicking bat and insect flight stratagems in order to perform autonomous tasks such as wall following and doorway detection (Chapter 6).

3. Prototype Design

This chapter describes the selection of a suitable platform for flight in near-Earth environments. The feasibility of slow flying fixed wing aircraft is first investigated and a MAV is prototyped. After realizing that hovering capabilities are most likely needed, a fixed and rotary wing hybrid platform is developed. Also described is a human pilot's procedure for hovering the hybrid aircraft and making the transition from cruise flight to hover mode. These methods will eventually be mimicked by the flight control system to perform the maneuvers autonomously.

3.1 CQAR Prototype

Aerial robots capable of flying in closed quarters must be small and capable of flying slowly. Such robots, dubbed Closed Quarter Aerial Robots (CQAR, pronounced "seeker") by the authors in [42], require specific design considerations as laid out in Section 1.2

- *wingspan of less than 0.9 meters*
- *cruise velocity of 2 m/s or less*
- *capable of flying outdoors in light to moderate winds*
- *high maneuverability and endurance*

Neither fixed or rotary wing platforms meet all of the preliminary design specifications; however, the feasibility of fixed wing aircraft was further investigated because of the promising results in [41]. When dealing with fixed wing aircraft, there is a tradeoff between platform weight, W, and cruise velocity, V. It can be seen from

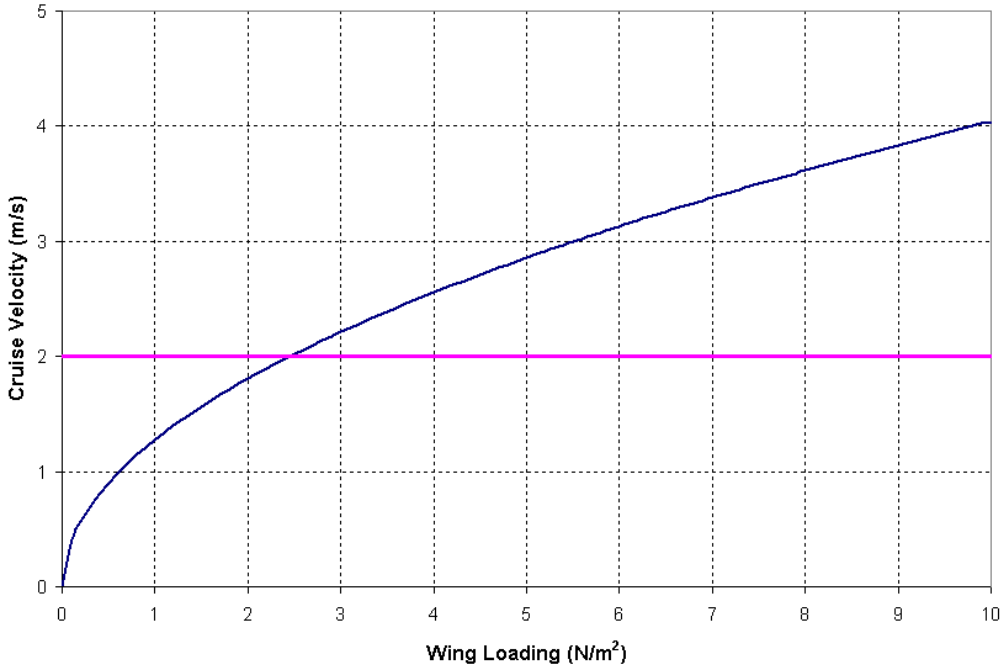

Figure 3.1: The minimum cruise velocity is plotted against a range of wing loading values.

Equation (3.1) that the minimum cruise velocity is higher for heavier aircraft

$$V = \sqrt{\frac{2W}{\rho S C_L}} \tag{3.1}$$

where ρ is the air density, S is the wing area, and C_L is the coefficient of lift. This tradeoff can be problematic for the design of a slow flying, fixed wing micro air vehicle. Figure 3.1 shows a plot of the minimum cruise velocity versus wing loading (W/S), assuming an air density at sea level and an estimated lift coefficient equal to one. The net result and the first hypothesis of this thesis is that a fixed wing aircraft with a wing loading of less than 2.5 N/m^2 will be able to maneuver in near-Earth environments.

These design specifications were used to develop the first prototype. In order for the aircraft to fly outdoors in light to moderate wind, it was estimated that a gross takeoff weight of 50 grams was needed. With a 2.5 N/m^2 wing loading, this resulted in a wing area of

$$\frac{W}{S} \leq 2.5 \Longrightarrow S \geq 0.1962 m^2 \tag{3.2}$$

To help visualize the parameters needed to achieve this, a graph was generated which showed various wingspans, chord lengths, and their resulting areas for rectangular-shaped wings (see Figure 3.2). It can be seen from the graph that the wing with a 0.225 meter chord is the only option which yields a 0.1962 m^2 wing area and a wingspan under 0.9 meters. However, a wingspan just under 0.9 meters is not desirable because it leaves little room for error when flying through a standard doorway. Therefore, to maximize the wing area while minimizing the platform size, a wingspan of 0.7 meters was selected as the design goal. From the graph in Figure 3.2, it can be seen that this results in a wing area of approximately 0.16 m^2 for a 0.225 meter wing chord. Using the aforementioned wing area, the aircraft must weigh 41 grams or less to achieve a wing loading of 2.5. The net effect is that a fixed wing MAV must be constructed which weighs less than 41 grams in order to fly at a 2 m/s cruise velocity.

To meet this weight restraint, an airframe was constructed out of light building materials such as balsa, carbon fiber, and mylar. A 60 cm long carbon fiber tube with a 1.5 mm outer diameter was used as the fuselage. The built-up wing and tail frames were formed with 1.5 mm thick balsa wood and covered with 3 micron mylar. Finally, the avionics, such as the motor, propeller, receiver, and lithium polymer battery, were mounted to the airframe (see Figure 3.3). The resulting prototype weighed 28 grams, carried 13 grams of payload, and was capable of flying at 2 m/s (see Figure 3.4a).

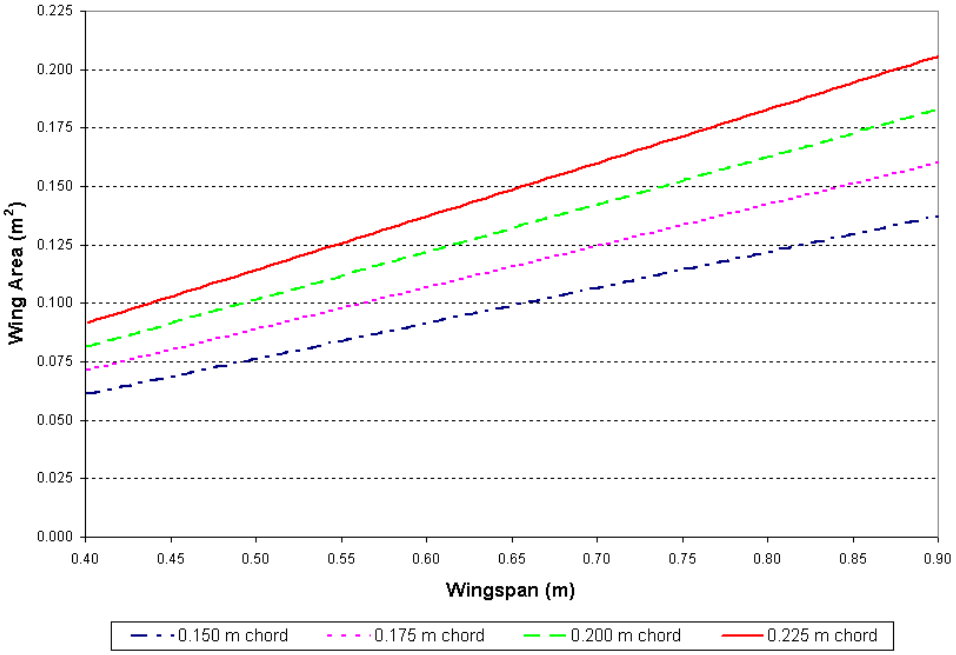

Figure 3.2: Wing area versus wingspan for four different wing chord lengths.

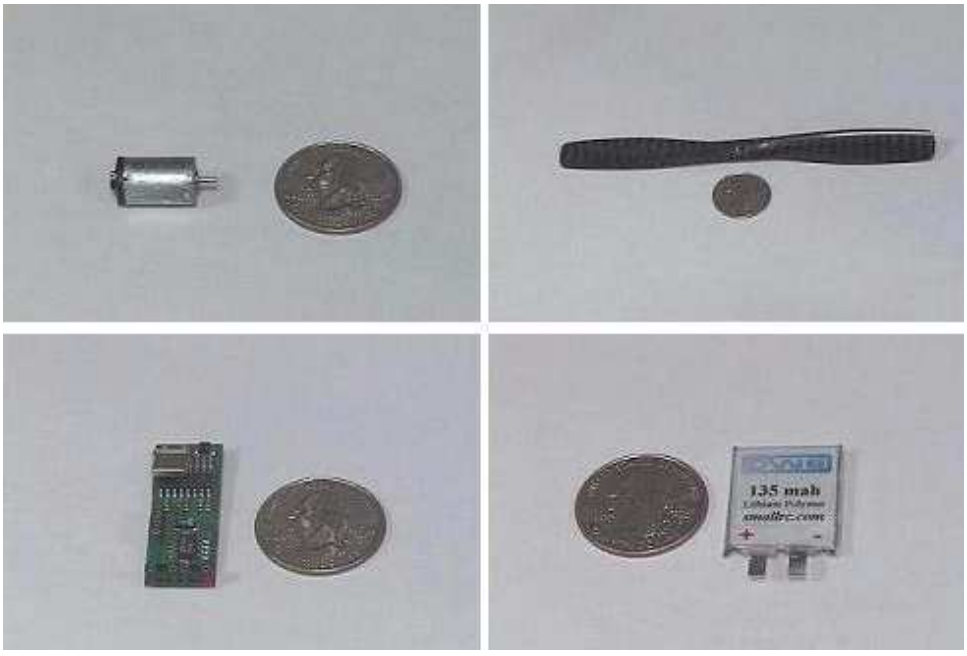

Figure 3.3: The motor, propeller, receiver, and lithium polymer battery used on the CQAR prototype.

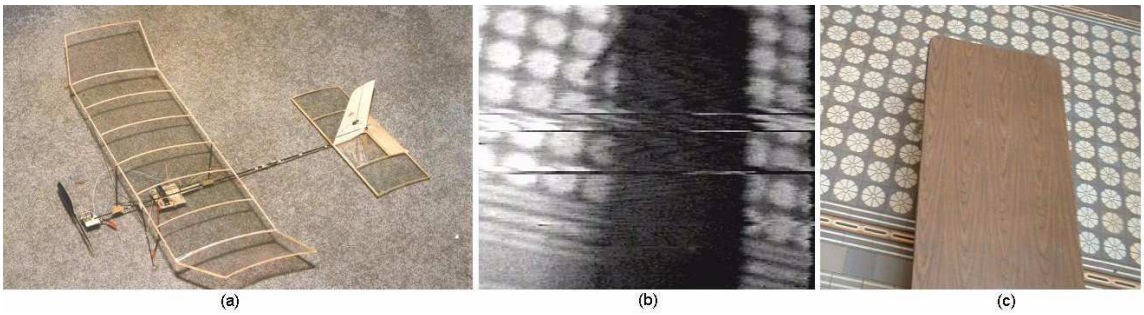

Figure 3.4: (a) The CQAR prototype, equipped with an onboard wireless camera, can acquire video and transmit images. (b-c) Such images, although noisy, compare well with regular cameras.

After several flight tests and experiments indoors, it was concluded that the CQAR prototype was able to fly extremely well inside urban structures with sparse obstacles. For example, the aircraft flew for more than 20 minutes while capturing surveillance video of a 10 x 10 meter, three-story atrium (see Figure3.4b-c). However, the prototype wasn't able to navigate in more densely populated obstacle fields as efficiently. Furthermore, the 41 gram prototype could not fly effectively in winds greater than 2 m/s. This demanded a heavier MAV with hovering capabilities and high maneuverability.

3.2 Hybrid Prototype

Integrating the endurance and agility of fixed-wing aircraft with hovering capabilities of rotorcraft has been realized in the radio-controlled (RC) community through a maneuver known as prop-hanging. During a prop-hang, the longitudinal axis of the fuselage is completely vertical and the thrust from the motor balances the weight of the aircraft. Leveraging this maneuver, a fixed-wing platform was prototyped with an additional flight mode for hovering [19].

3.2.1 Airframe

When designing the airframe of a hybrid aircraft, the most important attributes are the elevator and rudder areas. When hovering, the only airflow over the control surfaces is due to propeller wash. To compensate for this decrease in airflow when compared to conventional cruise flight, the elevator and rudder surface areas must be increased. Elevator and rudders typically occupy 20% of the horizontal and vertical stabilizers of remote-controlled (R/C) aircraft, respectively [51]. However, for a hybrid aircraft, the control surfaces should take up at least 50-60% of the stabilizer's surface area.

Using a R/C trainer aircraft as a template for stability, a fixed wing platform was designed with a 0.9 meter wingspan and a wing area of 0.227 square meters. The airframe was cut out of 3 mm depron foam and then laminated with 2 $oz./in^2$ carbon fiber cloth for durability. The carbon fiber also served to add weight to the airframe such that it could be controlled in windy conditions. The resulting airframe weighed 300 grams excluding avionics. It should be noted that the 0.9 meter wingspan was permissible because the aircraft will be traversing cluttered environments in the hovering orientation. That is, the aircraft can move through an opening such as a doorway with the wing plane parallel to its direction of motion. Therefore, the critical dimension is the overall height of the aircraft (i.e. from top to bottom) and not the wingspan.

3.2.2 Avionics

The most important design characteristic for the hybrid prototype is a thrust-to-weight ratio (T/W) greater than one. That is, the power system must generate enough thrust to balance the aircraft's weight when hovering. This is shown theoretically using Figure 3.5, which describes the forces acting on the MAV during a hover. The

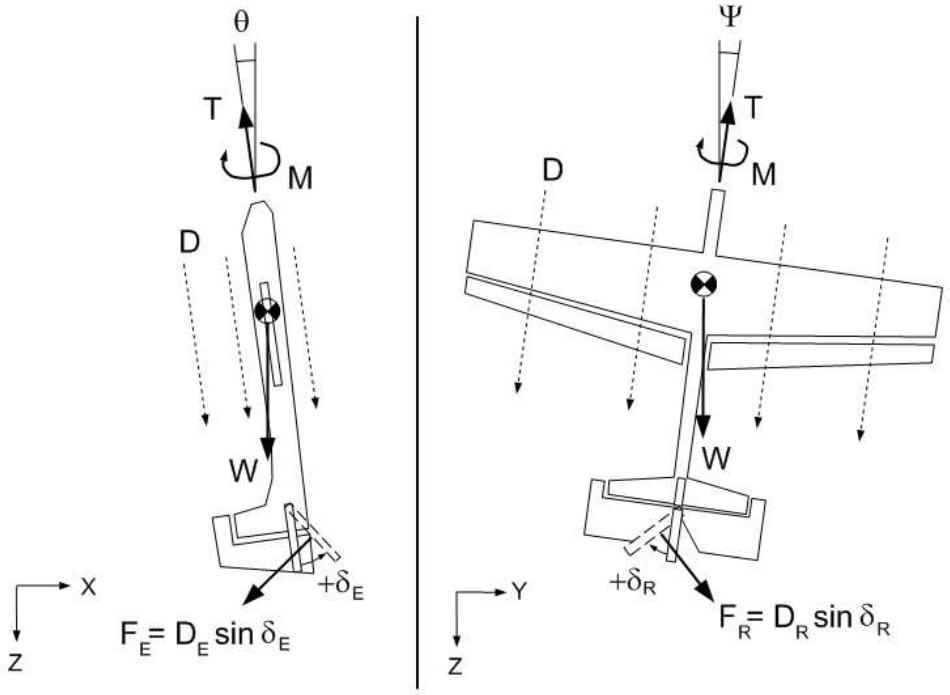

Figure 3.5: When in a hovering attitude, the elevator and rudder control surfaces are used to regulate the pitch and yaw angles, respectively.

forces generated by elevator (F_E) and rudder (F_R) deflection regulate the aircraft's pitch and yaw attitude, respectively, and are functions of the drag force, D, and control surface deflection angle, δ. The aircraft's altitude is modified by controlling the thrust force, T. Finally, the motor's reactive torque, M, can be countered with aileron deflection. If the hovering flight mode is represented as the global and body axes are aligned (i.e. $\theta = \psi = 0$), it can be seen by summing the forces in the vertical direction

$$(-T + D + F_E sin\delta_E + F_R sin\delta_R) cos\psi cos\theta + W = ma_Z \tag{3.3}$$

that the thrust force must equal the sum of the aircraft's weight and drag forces when in dynamic equillibrium (i.e. $\theta = \psi = \delta_E = \delta_R = a_z = 0$).

In order to select a motor which provides enough thrust, the overall weight of the

aircraft (including avionics) must be estimated. Table 3.1 below shows the estimated weight of the aircraft components, where the fields marked with asterisks are estimates and are not known before selecting a motor.

Table 3.1: Airframe and avionics weight estimates before selecting motor.

Components	Weight [g]
Airframe	300
Receiver	8
Servos (4)	36
LiPo Battery	75*
Brushless Motor/Gearbox	80*
Speed Controller	10*
Payload	75*
Total	**584**

The total estimated weight of the aircraft is roughly 600 grams. In order to incorporate extra thrust, a safety factor, and drag effects, a thrust-to-weight ratio of 1.5:1 was chosen as the design goal. Therefore, a motor should be selected which yields 900 grams of thrust in order to achieve a T/W of 1.5:1. A Himax brushless motor with a voltage constant (i.e. K_v) of 4200 was chosen. With a 12 x 6 propeller and a gear ratio of 6.6:1, the resulting setup yielded 875 grams of thrust. Figure 3.6 shows the prototype in its hovering attitude. With an 11.1 V, 1320 mAh lithium polymer battery, it can fly in cruise mode for 25 minutes at speeds ranging from 5-20 m/s. Hovering requires more power and as a result, the aircraft can only fly in this mode for about 10-12 minutes. These flight times can be increased, however, if larger battery capacities are used.

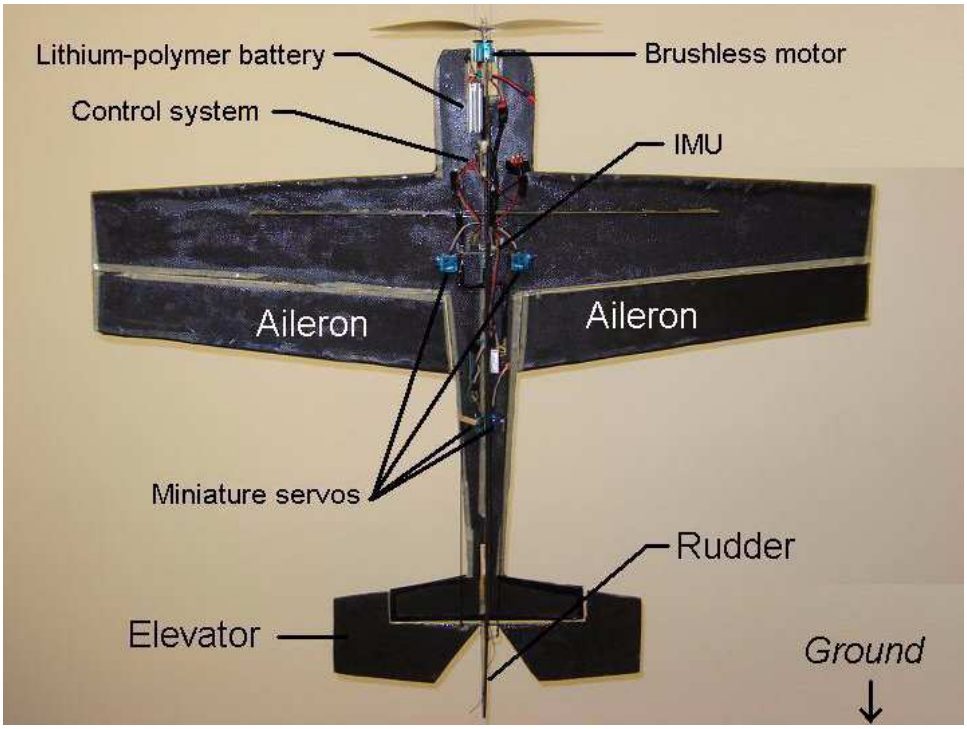

Figure 3.6: Our hybrid prototype weighs 600 grams, has a 1 m wingspan, and has a speed range of 0 to 20 m/s.

3.3 Manual Control

The unique capabilities of the prototype make it extremely difficult for a human pilot to fly. The pilot must have experience flying both fixed and rotary wing aircraft and must also have a feel for how the rudder and elevator deflection mimic a helicopter's cyclic control. The following section describes how a human pilot transitions between the cruise and hover flight modes and also how hovering is sustained.

3.3.1 Transitioning Between Flight Modes

The most critical aspect of the hybrid design is the transition from cruise to hover flight, which can also be used as a secondary collision avoidance maneuver (see Figure 3.7). During this phase, there exists an angle-of-attack, α, for which the wings

Figure 3.7: Our MAV prototype with a 1 meter wingspan manually transitions from cruise flight (top left) through the stall regime (top middle) and into a hovering position (top right) to avoid a collision with a basketball net.

are no longer a contributing factor to the lift component (i.e. stall). To achieve the transition, the aircraft has to leverage its momentum and essentially overpower its way through the stall regime. The high thrust-to-weight ratio built into the design helps to ensure that the momentum is not lost through the transition. Furthermore, as the aircraft is transitioning from cruise flight (minimum thrust) to the hovering flight mode, the throttle must be increased to balance the weight of the aircraft. The transition back to cruise mode first requires vertical acceleration to give the plane some momentum and then the elevator is deflected to pitch the aircraft forward into cruise mode. However, there may be circumstances when a vertical acceleration is not feasible (e.g. indoors with a low ceiling). In this case, the aircraft can be pitched forward first and then given increased throttle to pull out of stall.

3.3.2 Hovering

After transitioning into the hovering mode, the attitude must be sustained by constantly adjusting four channels of a radio-controlled transmitter. The most critical task the expert human pilot has is to maintain the aircraft's vertical orientation by adjusting the rudder and elevator deflection angles. Also, the throttle position must be modified to balance the weight of the aircraft. Once the stick position is found

to hold the plane at a constant altitude, it remains relatively constant as the aircraft is not gas powered and therefore maintains the same weight throughout the flight. Finally, the MAV's reaction to the motor torque results in the plane rotating about the vertical axis when hovering. This is known as torque rolling and can sometimes be countered with aileron control. All of these efforts must be done simultaneously which makes hovering a challenging task.

3.4 High-Alpha Representation

Automating the hovering flight mode and the transition into it requires the aircraft orientation to be accurately represented. This cannot be achieved with conventional methods such as Euler angles because of the singularities present during these high-alpha flight modes and maneuvers. Therefore, alternative methods must be investigated to represent the aircraft's attitude at large pitch angles. The following chapter discusses these different approaches in more detail.

4. Aircraft Attitude Representation

There are many different ways to represent the attitude of a rigid body in three-dimensional (3D) space. In the aircraft community, some of the more common methods include Euler angles, axis angle, and direction cosines. However, these methods are either vulnerable to singularities at critical orientations (e.g. an Euler pitch angle equal to ninety degrees) or computationally inefficient when representing rotations. To avoid these drawbacks, quaternions will be used as an alternative approach. Each of these methods and the algorithms for hovering and the cruise-to-hover transition will be discussed in the ensuing sections of this chapter.

4.1 Euler Angles

Euler angles are the most widely used approach for representing aircraft attitude because of their simplicity and intuitiveness. They describe the orientation of a rigid body in 3D space by three consecutive rotations. There are twelve different rotation combinations, but the aircraft community typically uses the $\psi \rightarrow \theta \rightarrow \phi$ sequence, which represents the aircraft's yaw, pitch, and roll respectively [40]. Euler angles have many advantages over other attitude representations, but their major drawback is the singularities present at pitch angles of $\pm$ 90 degrees. This can be seen in Equation (4.1) which describes the Euler rates ($\dot{\phi}$, $\dot{\theta}$, $\dot{\psi}$) as a function of the body angular velocities p, q, and r

$$\dot{\phi} = p + (qsin\phi + rcos\phi)/tan\theta \tag{4.1a}$$

$$\dot{\theta} = qcos\phi - rsin\phi \tag{4.1b}$$

$$\dot{\psi} = (qsin\phi + rcos\phi)sec\theta \tag{4.1c}$$

Equation (4.1) is integrated to find the Euler angles at the next time step; however, it can be seen that as the Euler pitch angle, θ, approaches $\pm$ 90 degrees, Equations (4.1a) and (4.1c) go to infinity. This makes the integration of the roll and yaw rates indeterminate and is commonly referred to as gimbal lock.

4.2 Axis Angle

The axis angle method is another way to represent aircraft orientation through rotation. The parameters used are an axis of rotation, e, which is commonly referred to as the eigenaxis or Euler axis, and the angle of rotation, θ, about that axis. The eigenaxis is parameterized as e_x, e_y, and e_z, and thus a 45 degree rotation about the y axis (i.e. pure pitch) would be represented by

$$(axis, angle) = (\begin{bmatrix} 0 \\ 1 \\ 0 \end{bmatrix}, \frac{\pi}{4}) \tag{4.2}$$

As in the Euler angle representation, the axis angle method also suffers from singularities. This can be seen in Equation (4.3) which shows the relationship between the change in the axis angle parameters with respect to time and the angular rates in the body frame [45]

$$\begin{Bmatrix} \dot{\Theta} \\ \dot{e}_x \\ \dot{e}_y \\ \dot{e}_z \end{Bmatrix} = \begin{bmatrix} 2e_x & 2e_y & 2e_z \\ C/S(-e_x e_x + 1) & -e_x e_y C/S - e_x & -e_x e_z C/S + e_y \\ -e_x e_y C/S + e_z & C/S(-e_y e_y + 1) & -e_y e_z C/S - e_x \\ -e_x e_z C/S - e_y & -e_y e_z C/S + e_x & C/S(-e_z e_z + 1) \end{bmatrix} \begin{Bmatrix} p \\ q \\ r \end{Bmatrix} \tag{4.3}$$

where $C = cos\frac{\Theta}{2}$ and $S = sin\frac{\Theta}{2}$. It can be seen from Equation (4.3) that when

the rotation angle, Θ, approaches 0 or nπ where n=1,2,3,..., the eigenaxis rates approach infinity. In this case, the integration of Equation (4.3) to find the eigenaxis is indeterminate.

4.3 Direction Cosines

Direction cosines can be used to represent aircraft orientation via the following matrix [21]

$$\begin{Bmatrix} x \\ y \\ z \end{Bmatrix} = \begin{bmatrix} C_\psi C_\theta & S_\psi C_\theta & -S_\theta \\ (-S_\psi C_\phi + C_\psi S_\theta S_\phi) & (C_\psi C_\phi + S_\psi S_\theta S_\phi) & C_\theta S_\phi \\ (S_\psi S_\phi + C_\psi S_\theta C_\phi) & (-C_\psi S_\phi + S_\psi S_\theta C_\phi) & C_\theta C_\phi \end{bmatrix} \begin{Bmatrix} X \\ Y \\ Z \end{Bmatrix} \tag{4.4}$$

where x, y, and z represent the components of an orientation vector in the body frame and X, Y, and Z describe an orientation vector in the global frame. C_x and S_x are used to represent $cos(x)$ and $sin(x)$ respectively.

Unlike Euler angles and axis angle representation, the Direction Cosines Matrix (DCM) does not suffer from singularities. However, it requires nine parameters to represent a rotation and therefore occupies more than twice the space required by Euler angles or the axis angle method. Furthermore, successive rotations are determined through matrix multiplication making the DCM inefficient in computation time when compared to other methods.

4.4 Quaternions

Quaternions provide yet another means of representing attitude and performing transformations between orthogonal, Cartesian coordinate systems [43]. They are most commonly used in the spacecraft [61] [59] and gaming industries [32]. The value of quaternions can be attributed to their compactness and freedom from singularities.

It was shown that Euler angles can represent attitude with just three parameters (e.g. roll, pitch, and yaw), but are singular at pitch angles of ninety degrees. Directional cosines are not vulnerable to singularities, but require nine matrix parameters compared to just four for quaternions. The characteristics of quaternions make them ideal for representing the orientation of vehicles which perform large angular maneuvers such as spacecraft. Although they are rarely used for attitude control of fixed-wing aircraft, quaternions serve as a promising approach for regulating the hovering flight mode of the hybrid prototype.

4.4.1 Definition

A quaternion is similar to the axis angle representation and consists of four parameters. The first three components represent the vector part of the quaternion and the fourth component represents the scalar portion. They are defined by

$$q_1 = e_x sin(\Theta/2) \tag{4.5a}$$

$$q_2 = e_y sin(\Theta/2) \tag{4.5b}$$

$$q_3 = e_z sin(\Theta/2) \tag{4.5c}$$

$$q_4 = cos(\Theta/2) \tag{4.5d}$$

where e_x, e_y, and e_z represent the eigenaxis, or Euler axis, and Θ gives the scalar angle of rotation about that axis. The eigenaxis is multiplied by the sine of half the rotation angle and the cosine of this angle is taken to represent the scalar component. These slight modifications are what differentiates quaternions from the axis angle method and also eliminates the mathematical singularities at large angles of attack.

Unit quaternions are used to represent the attitude of a rigid body in three-

dimensional space. Therefore, the four parameters in Equation (4.5) must satisfy the following constraint equation

$$q_1^2 + q_2^2 + q_3^2 + q_4^2 = 1 \tag{4.6}$$

4.4.2 Quaternion Rotations

Similar to the direction cosine matrix where successive rotations are described through multiplication, the products of quaternions can also be used to represent rotations. The multiplication of two quaternions, q_A and q_B, is defined by the following equation [59]

$$\begin{aligned} q_A \otimes q_B = (q_{A1}i + q_{A2}j + q_{A3}k + q_{A4}) \otimes (q_{B1}i + q_{B2}j + q_{B3}k + q_{B4}) = \\ (q_{A1}q_{B4} + q_{A2}q_{B3} - q_{A3}q_{B2} + q_{A4}q_{B1})i \\ +(-q_{A1}q_{B3} + q_{A2}q_{B4} + q_{A3}q_{B1} + q_{A4}q_{B2})j \\ +(q_{A1}q_{B2} - q_{A2}q_{B1} + q_{A3}q_{B4} + q_{A4}q_{B3})k \\ +(-q_{A1}q_{B1} - q_{A2}q_{B2} - q_{A3}q_{B3} + q_{A4}q_{B4}) \end{aligned} \tag{4.7}$$

where $\otimes$ is used to define quaternion multiplication and to distinguish it from the vector cross product. It should also be noted that quaternion multiplication is not commutative (i.e. $q_A \otimes q_B \neq q_B \otimes q_A$).

The motivation behind quaternion multiplication is to define a rigid body rotation from one coordinate frame to another. For example, using the quaternion q_A to represent the current orientation of a rigid body and quaternion q_{AB} to describe the rotation from orientation A $\rightarrow$ B, the new orientation quaternion, q_B, is calculated by

$$q_B = q_A \otimes q_{AB} \tag{4.8}$$

Equation 4.8 defines the significance of quaternion multiplication. It can be modified and applied to control aircraft attitude as seen in the following subsection.

4.4.3 Error Quaternion

Attitude control requires a measurement of the current orientation of the platform, a commanded or desired orientation, and the calculated difference between the two orientations. Towards this, three quaternions are defined, namely the commanded, measured, and error quaternions

- q_c: the commanded quaternion represents the desired aircraft orientation (e.g. the hovering flight mode).
- q_m: the measured quaternion describes the current orientation of the aircraft and is acquired from an onboard sensor.
- q_e: the error quaternion represents the required rotation to move from the measured attitude to the commanded attitude.

Equation (4.8) can be used to define the relationship between the parameters listed above. To get to the orientation defined by the commanded quaternion, the measured quaternion must be multiplied by the quaternion describing the rotation between the two frames (i.e. the error quaternion)

$$q_c = q_m \otimes q_e \tag{4.9}$$

Equation (4.9) must be solved for the error quaternion since its parameters will dictate the amount of control surface deflection needed to drive the vehicle to the commanded attitude. This is achieved by isolating q_e

$$q_e = q_m^{-1} \otimes q_c \tag{4.10}$$

An inherent property of unit quaternions is that the inverse is equivalent to the quaternion conjugate which is computationally simpler to calculate. The conjugate of a quaternion is represented by taking the negative of the vector components

$$q^* = -q_1 - q_2 - q_3 + q_4 \tag{4.11}$$

where q^* represents the quaternion conjugate. Therefore, Equation (4.10) becomes

$$q_e = q_m^* \otimes q_c \tag{4.12}$$

Equation (4.12) defines the error quaternion in the body frame of the aircraft. Therefore, the angular errors about each axis can be extracted from q_e and used in a control scheme (e.g. PID) to generate aileron, elevator, and rudder deflection to control the aircraft's attitude. This process is implemented in the autonomous hovering algorithm discussed in the next subsection.

4.5 Hovering Error Quaternion

The autonomous hovering algorithm begins by defining the commanded quaternion, q_c, which describes the MAV's orientation during a hover (i.e. vertical with belly facing north). The rotation is about the y axis and thus, the eigenaxis is represented by

$$(e_x, e_y, e_z) = (0, 1, 0)$$

With a rotation angle of ninety degrees, the quaternion representation of this attitude

is given by

$$q_{c_1} = e_x sin(\Theta/2) = 0 * sin(\pi/4) = 0.000i$$
$$q_{c_2} = e_y sin(\Theta/2) = 1 * sin(\pi/4) = 0.707j$$
$$q_{c_3} = e_z sin(\Theta/2) = 0 * sin(\pi/4) = 0.000k$$
$$q_{c_4} = cos(\Theta/2) = cos(\pi/4) = 0.707$$

To calculate the error quaternion using Equation (4.12), the measured quaternion must first be defined. Ultimately, the measured quaternion will be acquired with an attitude sensor (e.g. IMU) mounted onboard the aircraft. Initially however, it was assumed that the aircraft would start at orientations close to the hovering flight mode. For example, a simulation was created where the initial orientation of the aircraft was at roll, pitch, and yaw angles of 0, 75, and 0 degrees respectively, or

$$q_m = 0.0i + 0.609j + 0.0k + 0.793$$

Taking the conjugate of q_m and multiplying it by q_c results in the following error quaternion

$$q_e = (-0.0i - 0.609j - 0.0k + 0.793) \otimes (0.0i + 0.707j + 0.0k + 0.707)$$
$$q_e = 0.0i + 0.131j + 0.0k + 0.991$$

Once the error quaternion is calculated, the angular error about the x, y, and z axes can be extracted from q_e by first normalizing the vector component and then

multiplying by the angle

$$E_x = 2\cos^{-1}(q_{e_4})\, q_{e_1}/\|q_{e_v}\| \tag{4.14a}$$

$$E_y = 2\cos^{-1}(q_{e_4})\, q_{e_2}/\|q_{e_v}\| \tag{4.14b}$$

$$E_z = 2\cos^{-1}(q_{e_4})\, q_{e_3}/\|q_{e_v}\| \tag{4.14c}$$

where $\|q_{e_v}\|$ is the norm of the vector part of the error quaternion. When Equation (4.14) is applied to the error quaternion from above, it yields a pitch error of 15 degrees. Proportional-derivative (PD) control is then used to send signals to the elevator and rudder control servos. This, in turn, drives the aircraft orientation back to the hovering attitude. Although this algorithm seems to work effectively when the aircraft starts from orientations close to vertical, it was soon realized that it is not optimal for the transition from cruise to hover flight.

4.6 Cruise-to-Hover Transition

During autonomous hovering, the commanded quaternion represents the aircraft in the vertical orientation with the belly facing north (using a north-east-down coordinate frame). When autonomous hovering is initiated, the aircraft is already close to the vertical orientation but may or may not be facing north. This will result in a small amount of control effort from the elevator and rudder to get the plane vertical and a large control effort about the x-axis to roll the aircraft until the belly faces north. This makes the commanded quaternion used for autonomous hovering (i.e. q_c = 0.0i + 0.707j + 0.0k + 0.707) sufficient when releasing the aircraft in near-hovering orientation. However, when dealing with large initial errors like when transitioning from cruise to hover flight, this algorithm is not preferred.

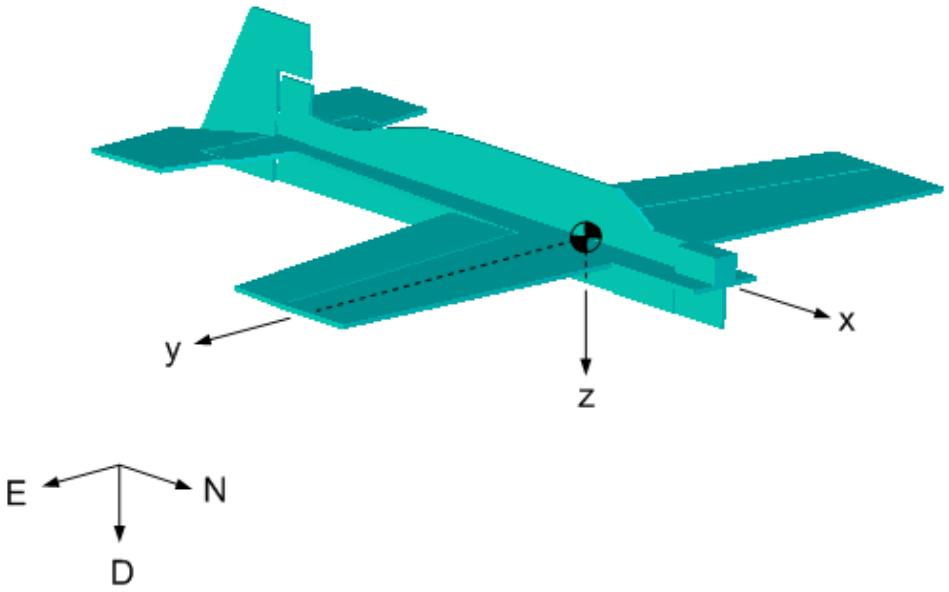

Figure 4.1: The MAV in cruise flight heading north.

4.6.1 Orientation Issues

Using a north-east-down reference frame, imagine the MAV to be flying in cruise mode heading north (i.e. body and reference frames are aligned). This is shown in Figure 4.1. If the commanded quaternion used for autonomous hovering was also used for the transition from cruise (heading north) to hover flight, the commanded, measured, and error quaternions would be

$$q_c = 0.0i + 0.707j + 0.0k + 0.707 \tag{4.15a}$$

$$q_m = 0.0i + 0.0j + 0.0k + 1.0 \tag{4.15b}$$

$$q_e = 0.0i + 0.707j + 0.0k + 0.707 \tag{4.15c}$$

where q_m represents cruise mode heading north.

Normalizing q_e and finding the angular error about each axis using Equation (4.14)

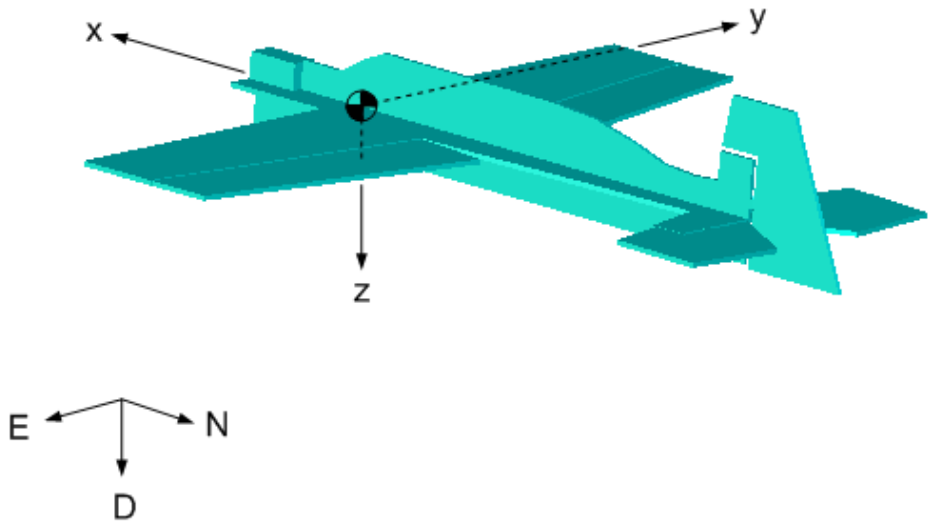

Figure 4.2: The MAV in cruise flight heading south.

results in a ninety degree pitch error and zero error about the roll and yaw axes. As desired, the controller would respond with large elevator deflection causing the aircraft to pitch up towards the vertical orientation.

However, if the MAV was flying in cruise mode and heading south (see Figure 4.2), the same commanded quaternion will not result in a pure pitch up maneuver. That is, if the same commanded quaternion was used, the commanded, measured and error quaternions would now be

$$q_c = 0.0i + 0.707j + 0.0k + 0.707 \tag{4.16a}$$

$$q_m = 0.0i + 0.0j + 1.0k + 0.0 \tag{4.16b}$$

$$q_e = 0.707i + 0.0j - 0.707k + 0.0 \tag{4.16c}$$

where q_m represents cruise mode heading south.

Normalizing q_e and finding the error about each axis results in large roll and yaw

errors and zero pitch error. This is because a combination of roll and yaw will yield the minimum rotation to get the aircraft to the commanded quaternion (vertical with belly of aircraft facing north) rather than pitching up 90 degrees and then rolling 180 degrees. While this maneuver will most likely work, it was desired to have a pure pitching motion to transition from cruise to hover when heading in any direction. That is, if the aircraft is in cruise mode heading south, the transition from cruise flight to hover mode should leave the aircraft in the vertical orientation with the belly facing south. This method was desired because it primarily required control about a single axis rather than two axes simultaneously. Furthermore, when put into practical use, the aircraft will most likely be flying towards its target with a camera mounted on the belly of the airframe. Ideally, the aircraft would pitch up and have the belly still facing the target. To achieve this, a delta quaternion is introduced which generates a new commanded quaternion based on the aircraft's heading when the cruise-to-hover algorithm is initialized.

4.6.2 Cruise-to-Hover Error Quaternion

When the transition from cruise to hover is initialized, there is an angular error between the x axis of the aircraft and a vertical vector expressed in the reference frame. Assuming perfect cruise conditions (i.e. ϕ=0, θ=0, and -180 $\leq \psi \leq$ 180 degrees), this error is equal to ninety degrees about the pitch axis. As mentioned above, the commanded quaternion for hovering cannot be used because it will not result in the desired pitch up maneuver to reach the vertical orientation [28]. Instead, vector and quaternion mathematics will be used to generate a delta quaternion which represents a rotation from the initial aircraft attitude in quaternion form to the vertical orientation. Using the delta and measured quaternions, a commanded quaternion can then be calculated which represents the vertical orientation with the belly facing the

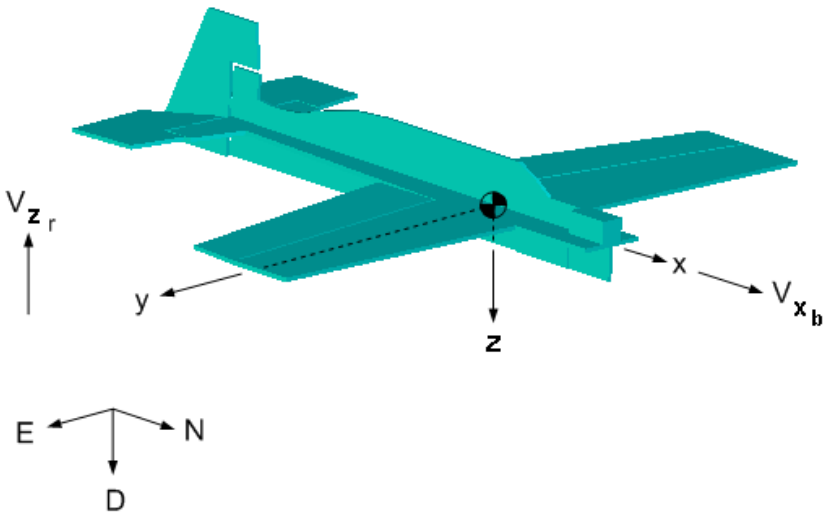

Figure 4.3: The vertical vector in the reference frame is shown along with the x axis vector in the body frame.

same direction as the aircraft was heading when the algorithm was initialized. Upon obtaining the commanded quaternion, the error quaternion can then be computed for each new measured quaternion (i.e. each control loop iteration) which will generate a pure pitching maneuver despite the initial aircraft heading.

Assuming the cruise-to-hover program has been initialized and the first measured quaternion has been acquired, the process to calculate the delta quaternion starts by defining the vertical vector in the reference (NED) frame, V_{z_r}

$$V_{z_r} = 0.0i + 0.0j - 1.0k \tag{4.17}$$

and the aircraft's x axis in the body frame, V_{x_b}, as seen in Figure 4.3.

$$V_{x_b} = 1.0i + 0.0j + 0.0k \tag{4.18}$$

It is desired to keep the error quaternion in the aircraft's body frame such that the angular errors can be directly used to control the aileron, elevator, and rudder surfaces. Therefore, all calculations will be performed in the body frame. As such, the first step is to transform the vertical vector (V_{z_r}) from the reference frame to the body frame using the measured quaternion. This is performed by

$$V_{z_b} = q_m^* \otimes V_{z_r} \otimes q_m \tag{4.19}$$

where V_{z_b} represents V_{z_r} transformed to the body frame. It should be noted that in the above equation, V_{z_r} is first converted to a fourtuple by adding a zero to act as the scalar component. This is done to make it compatible with quaternion multiplication. V_{z_b} is then converted back to a vector by removing the scalar portion of the resulting fourtuple.

Now that the vertical vector and the aircraft's x-axis are both represented in the body frame, vector mathematics can be used to find an orthogonal rotation axis and angle between the two vectors. The cross product is calculated to find the rotation axis, or the axis which is orthogonal to both vectors

$$V_{rot} = V_{x_b} \times V_{z_b} \tag{4.20}$$

Next the angle between the MAV's x axis and vertical vector in the body frame can be found by using the dot product

$$\gamma = \cos^{-1}(V_{x_b} \cdot V_{z_b}) \tag{4.21}$$

The axis and angle representing the rotation to have the aircraft's x axis coincide with the vertical vector are now known and can be converted into a quaternion, which

will be referred to as the delta quaternion, q_Δ.

$$q_{\Delta_1} = V_{rot_1} \sin(\gamma/2) \tag{4.22a}$$

$$q_{\Delta_2} = V_{rot_2} \sin(\gamma/2) \tag{4.22b}$$

$$q_{\Delta_3} = V_{rot_3} \sin(\gamma/2) \tag{4.22c}$$

$$q_{\Delta_4} = \cos(\gamma/2) \tag{4.22d}$$

The newly calculated delta quaternion, q_Δ, and the first measured quaternion from Equation (4.19) can be used to calculate the new commanded quaternion, q_c'

$$q_c' = q_m \otimes q_\Delta \tag{4.23}$$

The new commanded quaternion represents the vertical orientation with the belly of the aircraft facing in the same direction as the heading in cruise mode. The entire process to calculate q_c' is performed once at the initialization of the cruise to hover maneuver. The resulting commanded quaternion remains constant and is used in every iteration along with a new measured quaternion to compute the error quaternion. The equation for the error quaternion (4.12) is restated below

$$q_e = q_m^* \otimes q_c'$$

Finally, since the error quaternion is calculated in the body frame of the aircraft, the angular error about each axis can be used to control the aileron, elevator, and rudder surface deflection. The angular errors are calculated using the relationships

from Equation (4.14)

$$E_x = 2\cos^{-1}(q_{e_4})\, q_{e_1}/\|q_{e_v}\|$$
$$E_y = 2\cos^{-1}(q_{e_4})\, q_{e_2}/\|q_{e_v}\|$$
$$E_z = 2\cos^{-1}(q_{e_4})\, q_{e_3}/\|q_{e_v}\|$$

Again, the angular errors about each axis can be used in a proportional-derivative (PD) control scheme to generate aileron, elevator, and rudder deflections.

$$\delta_e = K_{p_e} E_y + K_{d_e} \dot{E}_y \tag{4.25a}$$
$$\delta_r = K_{p_r} E_z + K_{d_r} \dot{E}_z \tag{4.25b}$$

5. Attitude Control of the Hybrid Platform

The algorithms discussed in Chapter 4 to calculate the error quaternions will be incorporated into an attitude controller and embedded onto the onboard flight control system. In order to acquire the aircraft orientation in quaternion form, the flight control system will be interfaced with a small and lightweight inertial measurement sensor. The integrated system is able to achieve the first documented success[1] of autonomously hovering a fixed wing micro air vehicle [18]. In addition, data is captured during both manual and autonomous hovering and is used to compare the controller performance to that of an expert human pilot. Next, the cruise-to-hover error quaternion from the previous chapter is used in a slightly different controller to achieve the transition from cruise to hover flight autonomously [17]. These novel experiments revealed new challenges which are addressed in the latter part of this chapter. For example, in order for the video from the MAV's onboard camera to be useful in surveillance applications, the torque roll effect during hover must be eliminated. This is accomplished by mounting small motorized propellers on the tip of each wing to create a counter-rotating force. Also, an altitude controller was incorporated into the system and used to demonstrate full autonomous hovering of the hybrid prototype.

5.1 Attitude Sensor

Autonomous control of the hybrid prototype requires an inertial sensor capable of measuring aircraft attitude during unconventional maneuvers and orientations. The two most critical parameters are the output mode and gyro range capabilities of the sensor. Ideally, the sensor will have more than a single Euler output mode because of their singularity at $\pm$ 90 degrees. A direction cosine matrix can be converted to

[1] To the best of the author's knowledge

a quaternion and used in the algorithms of Chapter 4; however, this requires a lot of unnecessary computations. An inertial sensor which outputs quaternions directly will be more computationally efficient. The other parameter which factors into sensor selection is the gyro range. Typically, this is specified at 150 or 300 deg/s for most MEMs gyros. Careful consideration must be given in selecting this parameter because of the fast transition from cruise to hover flight. The gyro range must be greater than the speed of the transition. That is, orientation errors will arise if the transition occurs at a rate of 200 deg/s. and the gyro range is specified at 150 deg/s.

Before investing in an expensive inertial measurement unit (IMU), the speed of the transition had to be measured. FMA Direct makes a pitch and roll sensor for less than $100 called the F8 Copilot (see Figure 5.1a). It works on the principle that the earth is much warmer than the surrounding air. With four infrared heat sensors covering a panoramic view of the environment, temperature readings are acquired and processed. The F8 Copilot then classifies the region of the highest temperature gradient as the horizon. The attitude of the aircraft can then be calculated relative to the horizon. The sensor was mounted on the aircraft during a manual cruise-to-hover transition and the pitch angle data from this flight was plotted against time (see Figure 5.1b). It can be seen that the transition from 0 to 90 degrees occurs in approximately 0.75 seconds, or at a rate of 120 deg/s. It should also be noted that in the last trial, the aircraft is hovering in 10 mph wind and must pitch forward to compensate.

After processing the flight data during the transition, it was determined that a sensor with a gyro range of at least 150 deg/s. was required. Using this specification and a desired output mode in quaternion form, an inertial measurement unit (IMU) by Microstrain was selected. Figure 5.2 shows the Microstrain IMU which outputs a gyroscopically stabilized four component quaternion describing the MAV's orientation

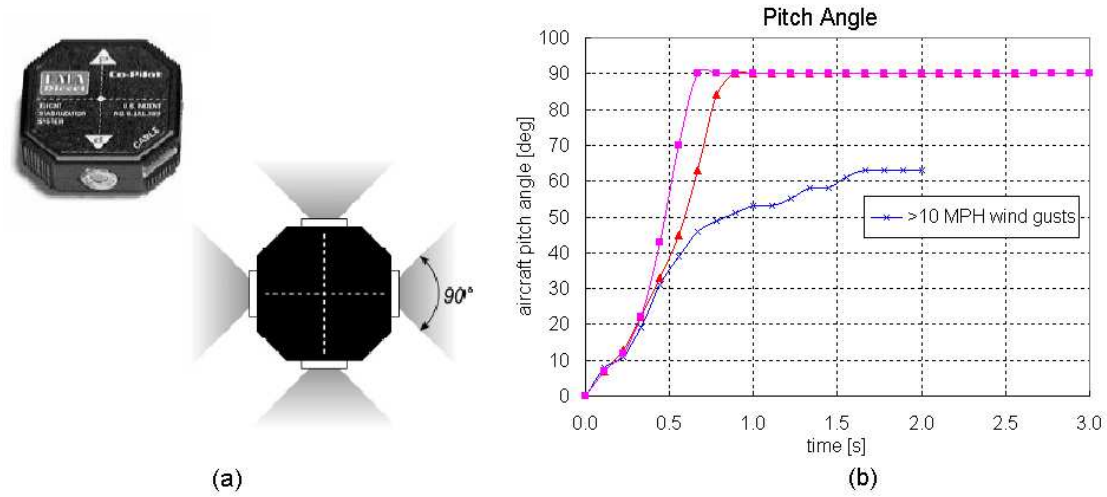

Figure 5.1: (a) FMA Direct's F8 Copilot is used to measure the pitch rate of the hybrid prototype. Reprinted from *www.fmadirect.com*. (b) Data captured during the transition from cruise to hover flight is used to determine the rate of the maneuver.

with respect to the fixed earth coordinate frame. It weighs just 30 grams out of its protective casing and is comprised of three triaxial accelerometers and angular rate gyros as well as three orthogonal magnetometers. The gyro range is 300 deg/s which is more than enough to handle the transition from cruise to hover flight. It uses RS-232 protocol for communication and transmits attitude information in data packets. For example, a four component quaternion would consist of 11 bytes of data in the following format

- Byte 1: Header byte
- Bytes 2 and 3: q_0 MSB and LSB
- Bytes 4 and 5: q_1 MSB and LSB
- Bytes 6 and 7: q_2 MSB and LSB
- Bytes 8 and 9: q_3 MSB and LSB
- Bytes 10 and 11: Timer MSB and LSB
- Bytes 12 and 13: Checksum MSB and LSB

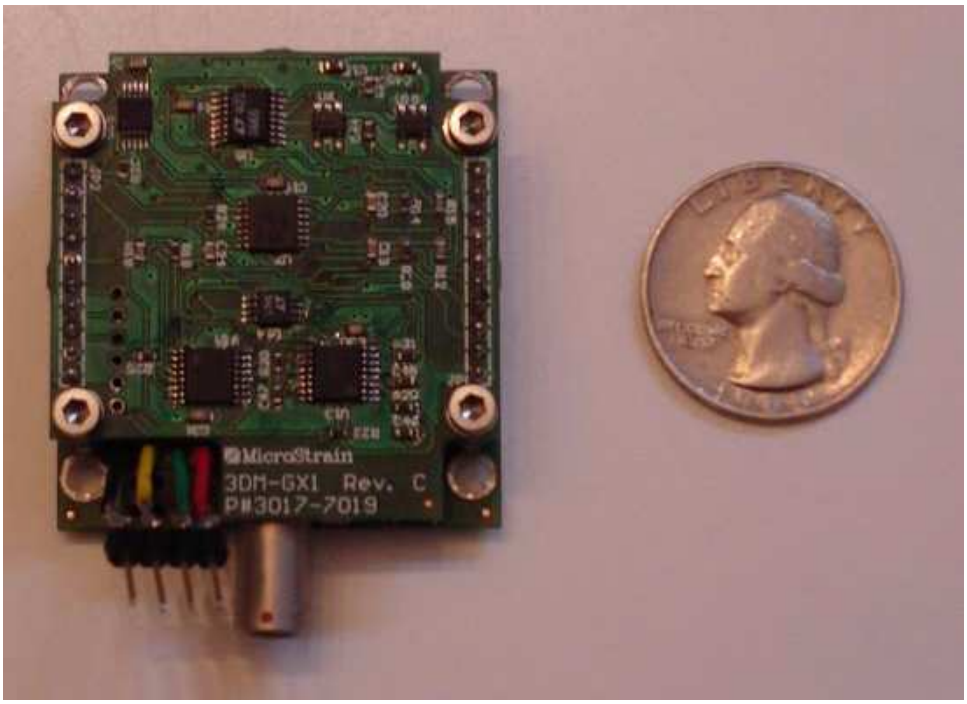

Figure 5.2: Microstrain's 30 gram IMU sensor was used to feedback attitude information to the onboard control system.

A data packet of this length can be acquired at a rate up to 100 Hz. Mounting the IMU at the MAV's center of gravity and interfacing it with a flight control system will enable autonomous attitude control of the aircraft.

5.2 Flight Control System

The hovering flight mode of the hybrid platform enables it to fly in urban areas and other cluttered environments. The characteristics of these flying domains such as tall buildings and enclosed areas make communication difficult. This makes controlling the aircraft from a remote base station a perilous task. To eliminate the risk of communication dropouts, a flight control system (FCS) was designed to fit onboard the aircraft. Furthermore, the FCS was designed to weigh less than 25 grams in order to reserve half of the 100 gram payload for navigational sensors.

5.2.1 Components

The most critical component of the flight control system is the microcontroller. It has several responsibilities including acquiring attitude data from the IMU, implementing the control algorithm for autonomous hovering or the transition into hover mode, and generating the corresponding pulse width modulated (PWM) servo signals to control the amount of aileron, elevator, and rudder deflection. Microchip's PIC series microcontrollers were investigated because of their robustness and availability. In addition, Custom Computer Services (CCS) has developed a software package enabling the user to write PIC applications in the C programming language with floating point math capabilities. A PIC18F8722 was selected for the FCS because of its large amount of program (e.g. 128 KB) and data (e.g. 3.9 KB) memory, multiple Capture-Compare-PWM pins to decode PWM signals, several RS-232 transmit and receive pins, I^2C capabilities to write data to external memory, and surface mount packaging to reduce size and weight.

The two other significant components of the FCS include an RS-232 converter chip and external memory. The IMU transmits RS-232 data at $\pm$ 12 volt levels while the PIC microcontroller can only communicate with serial devices at TTL voltage levels. Therefore, a MAX235 RS-232 converter chip was incorporated between the IMU and the microcontroller and also allows for four additional RS-232 devices to be interfaced with the FCS. The FCS also includes 65 KB of Electronically Erasable Programmable Read-Only Memory (EEPROM). Altitude data for each flight is sent to the EEPROM chip via I^2C communication and is downloaded and analyzed post-flight. Also, the FCS was designed to be modular and includes six input and five output ports for connecting servos or other DC motors. Therefore, it can easily be disconnected from one air or ground vehicle and used as the control system for another by simply reprogramming the microcontroller. The complete system weighs 25 grams

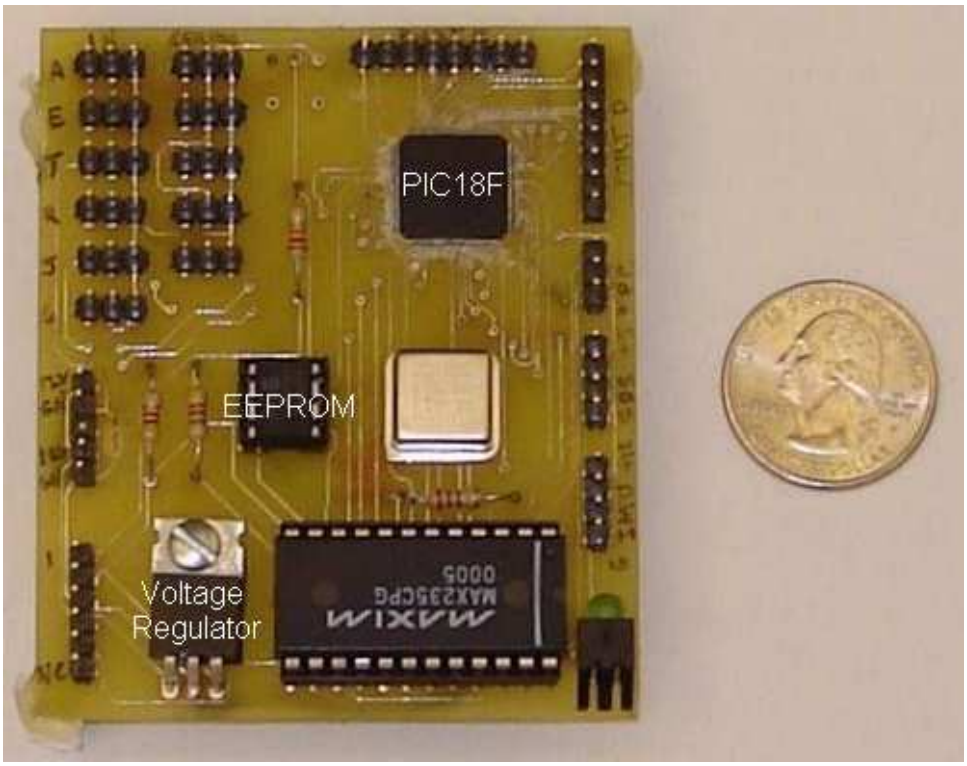

Figure 5.3: A 25 gram flight control system was developed for controlling the hybrid prototype.

and is shown in Figure 5.3.

5.2.2 Manual Override

The manual override feature of the flight control system played an integral role in the evolution of the control algorithms. It enabled new algorithms to be tested and optimized with minimal risk to the airframe. If during a live flight test, the aircraft exhibited an unexpected response, the expert human pilot would flick a switch on the R/C transmitter to override the flight control system. Upon taking over, the pilot has full control of the aircraft. This feature extended the life of the aircraft on several occasions.

The implementation of the manual override feature was done in software in order to

eliminate the need for any additional hardware. Additional hardware such as switches and multiplexers add weight to the avionics system and also increase the chance of failure. The switch shown in Figure 5.4 is linked to channel 6 on the aircraft receiver. When the switch is flicked towards the pilot to enable manual control, a 2 ms PWM signal is generated at the receiver end. When the switch is pushed away from the pilot to engage autonomous control, a 1 ms PWM signal is formed at the receiver end. The function of the FCS microcontroller is to decode the PWM signal and determine the length of the incoming pulse from channel 6.

Figure 5.4: A switch on the remote-controlled transmitter was used to toggle back and forth between manual and autonomous control.

The microcontroller comes equipped with five capture-compare-PWM (CCP) modules. These allow an interrupt to be triggered when the incoming signal goes from

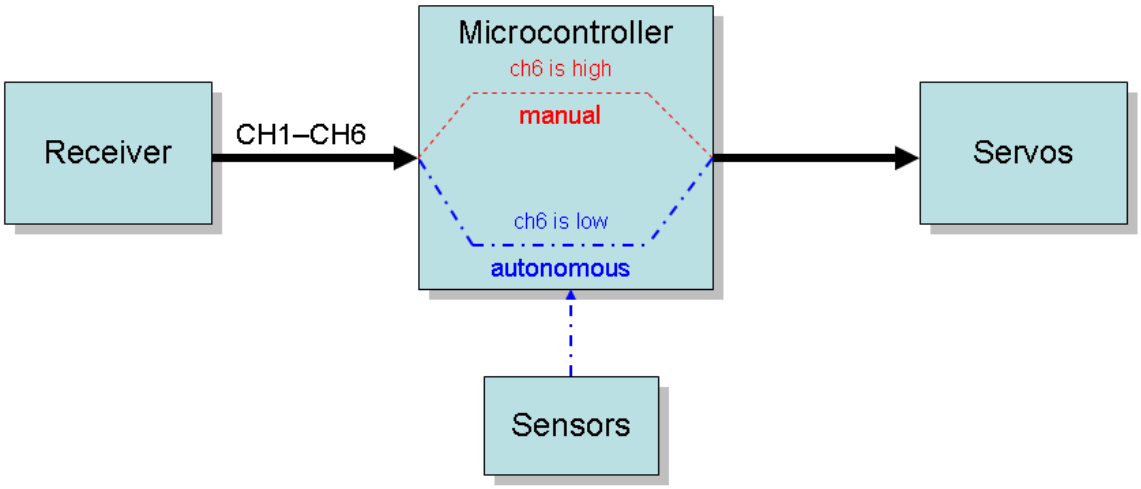

Figure 5.5: During manual mode, the signals from the receiver are passed directly to the servos. When in autonomous mode, the control signals are sent to the servos based on sensor data.

low to high or high to low. To determine the length of the pulse, the high time must be measured. As such, the interrupt is set up to trigger when the incoming channel 6 pulse goes from low to high. Inside the interrupt routine, a 16-bit timer module (TIMER1) is initiated and begins counting while the pulse remains high. When the pulse goes low, the timer value is read, converted to milliseconds, and stored in a global variable to be accessed in the main program. Within the main loop, a 1.5 ms threshold is set. If the pulse length is above this threshold, the microcontroller passes the incoming signals from the receiver directly to the servos. Otherwise, the FCS generates servo signals based on the output of the attitude controller (see Figure 5.5). With the manual override feature operating efficiently, autonomous hovering experiments were ready to be performed.

5.3 Autonomous Hovering Experiments

After mounting the IMU at the aircraft's center-of-gravity and interfacing it with the flight control system, the control algorithms could now be programmed to the microcontroller and tested. A series of experimental hypotheses are created to assess the outcome of the experiments, which take place inside urban structures as well as outdoors in moderate wind conditions. The hypotheses are discussed along with the experimental procedures and results in the ensuing subsections.

5.3.1 Autonomous Hovering Hypothesis 1

The first hypothesis for the autonomous hovering experiments was that using the error quaternion from Chapter 4 in a simple proportional-derivative controller will stabilize (i.e. maintain a vertical orientation) the aircraft during a hover.

The first autonomous hovering experiments were conducted inside an urban structure with limited flying space (i.e. 3m x 3m area) to demonstrate that hovering can be sustained within small areas. The MAV is released in near-hovering orientation (i.e. the fuselage is close to vertical) and manually given enough thrust to balance the weight of the aircraft. The quaternion algorithm from Chapter 4 begins by sampling the measured quaternion, q_m, from the IMU and multiplying the conjugate of it by the commanded quaternion, q_c, to get the error quaternion. The angular errors about each axis are then extracted from the error quaternion. Proportional-derivative control is performed on the pitch and yaw errors to keep the aircraft vertical. Figure 5.6 shows the control loop which repeats continuously and is synchronized with the IMU clock cycle (i.e. every 10 ms).

Initial experiments demonstrated that the MAV was able to successfully sustain a hover for several minutes before draining the battery (see Figure 5.7). This confirms the first hypothesis in that a PD pitch and yaw controller was able to stabilize the

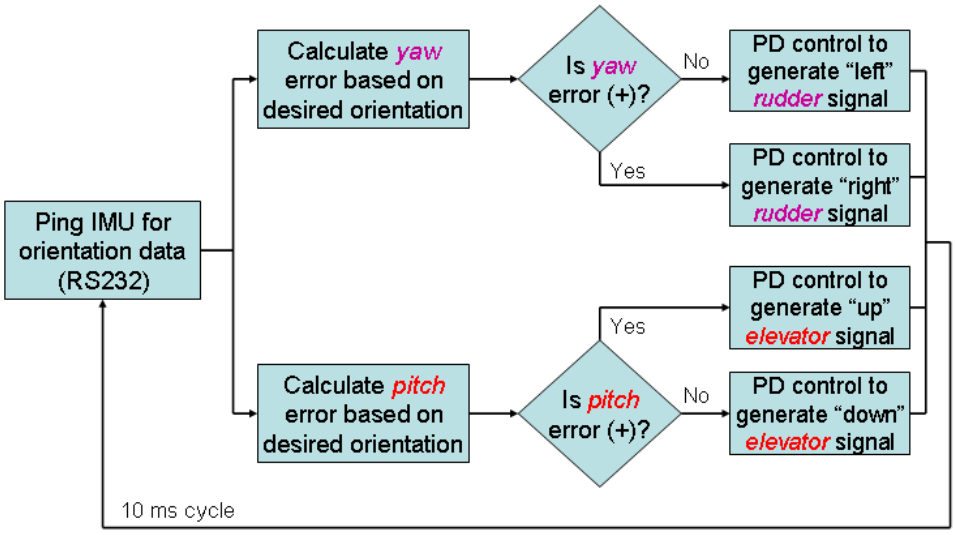

Figure 5.6: Flow chart describing the autonomous hovering code.

aircraft during hover mode.

5.3.2 Autonomous Hovering Hypothesis 2

The reactive torque from the motor (i.e. torque roll) is beneficial because it provides a panoramic view from the onboard wireless camera.

The reactive torque, which results from the rotational force the motor exerts on the propeller, causes the plane to rotate about the vertical axis when hovering. When mounting a wireless camera on the belly of the aircraft, the rotation about the vertical axis will provide panoramic images of the environment. To evaluate this hypothesis, a 12 gram, 2.4 GHz wireless camera system and 2-cell lithium polymer battery were interfaced and mounted on the hybrid prototype. The aircraft was released in near-hovering orientation and was able to sustain a hover for several minutes. The wireless video transmitted to the ground-based receiver was recorded and the roll angle of the aircraft was logged to the flight control system's external memory.

When playing back the video offline, it was instantaneously realized that the

Figure 5.7: MAV performing a *hands-off* autonomous hover inside an urban structure.

second hypothesis was incorrect. The aircraft is rotating so quickly that the video had a dizzying effect on the viewer. This phenomenon is easier to justify with the flight data as opposed to image stills extracted from the video. Figure 5.8 shows the flight data with no torque roll control. With the plane constantly rotating, a plot of the angular data would grow rapidly. To make each revolution more visible, the roll angle was bounded between -180 and 180 degrees. It can be seen that the plane completes 7 full revolutions in 16 seconds, or is torque rolling at a rate of 26 rpm. The net result is that the torque roll had to be controlled. Therefore, the second hypothesis is revisited in section 5.5.

5.3.3 Autonomous Hovering Hypothesis 3

When comparing the performance of the flight control system to that of an expert human pilot, the FCS will surpass the human.

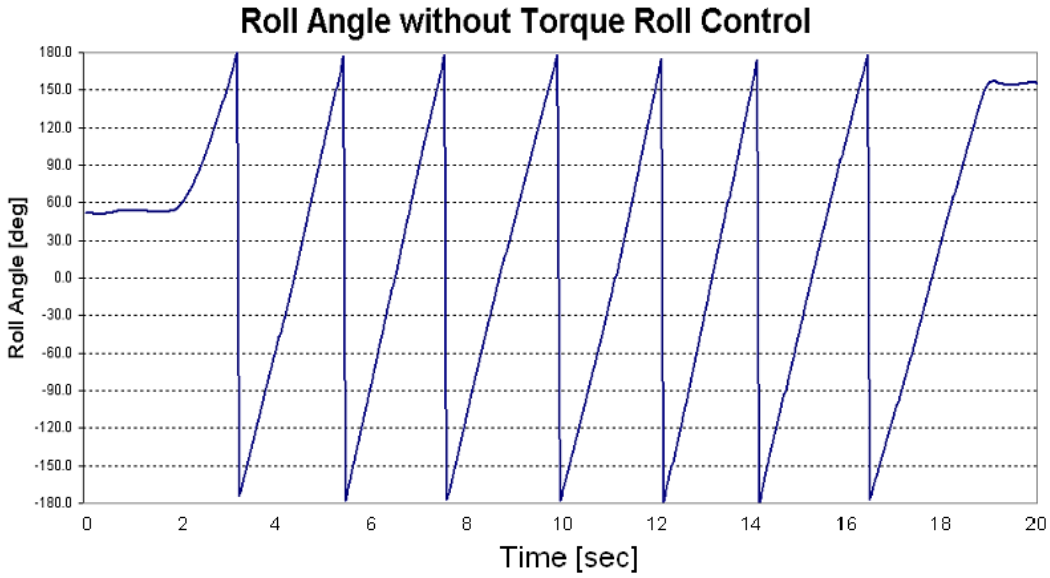

Figure 5.8: Roll angle captured during autonomous hovering without torque roll control.

To assess this hypothesis, an experiment was performed to contrast hovering under both manual and autonomous control. The metrics used were

1. Duration of the hover before the FCS/human loses control

2. Stability of the aircraft while in hovering mode

A skilled human pilot was initially given control of the aircraft and was instructed to fly around a gymnasium in cruise configuration, transition from cruise to hover flight, and attempt to hover the aircraft for as long as possible. The video stills[2] in the top of Figure 5.9 show the pilot struggling to keep the fuselage vertical, but is able to keep the aircraft positioned over a small area. Out of a few trials, the human pilot was able to sustain a hover for several minutes before draining the battery. However, the aircraft's pitch and yaw angles oscillated significantly as the pilot tried to keep the

[2]The video sequence shows three images extracted once a second for a period of three seconds. With the plane rotating at a rate of 0.25 revolutions per second, this is enough to show two quarter rotations.

Figure 5.9: A skilled human pilot hovers a fixed-wing aircraft in a small gymnasium and struggles to maintain a vertical orientation (top). Under autonomous control, the same aircraft is able to sustain a hover while remaining fixed in the vertical position (bottom).

aircraft in the vertical orientation. This is supported with a portion of the captured flight data, labeled *human-controlled*, in Figure 5.10.

A second trial was conducted where the pilot was instructed to again fly in cruise configuration and manually transition from cruise to hover flight. However, instead of trying to hover the aircraft manually, the pilot flicked a switch on the transmitter which enabled the onboard control system. This time, the aircraft is fixed in a vertical position and is able to hover for several minutes before exhausting the battery (see bottom of Figure 5.9). Again, the flight data was captured and a fraction of it is shown in Figure 5.10. The length of the hover for the flight controller was comparable to that of the human, however, the FCS was able to achieve a higher margin of stability as seen from the flight data.

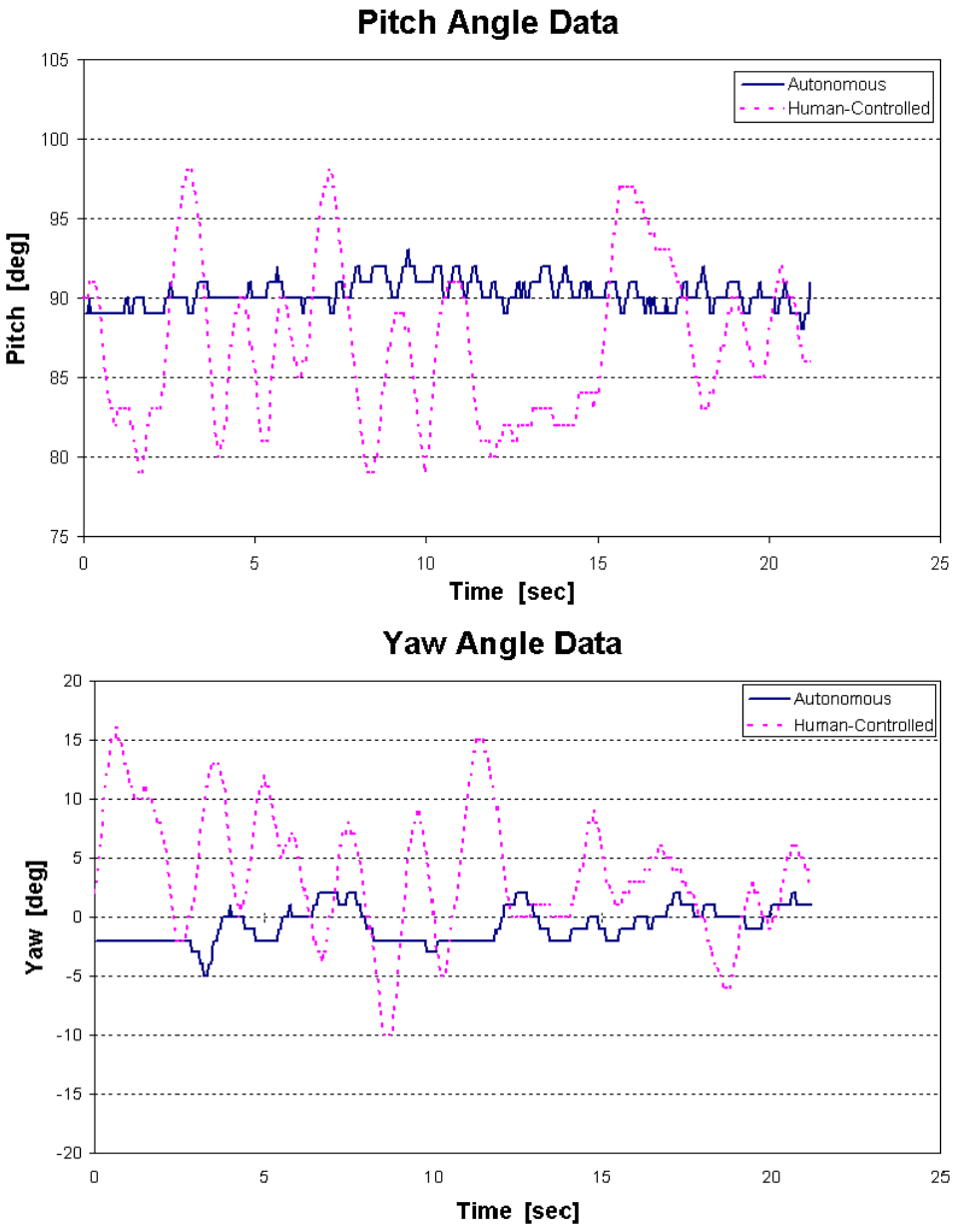

Figure 5.10: Pitch and yaw angles captured during both human-controlled and autonomous hovering.

5.4 Autonomous Cruise-to-Hover Experiments

Another series of experimental hypotheses were created to assess the autonomous cruise-to-hover (CTH) transition. The experiments are conducted outside in an open field and inside an urban structure. The hypotheses are discussed along with the experimental procedures and results in the following subsections.

5.4.1 Autonomous CTH Hypothesis 1

Multiplying the elevator derivative gain by a factor of 3 is enough to kill the momentum when arriving at the hovering orientation.

In the autonomous hovering experiments, the aircraft is released close to the desired orientation. Therefore, the angular errors extracted from the hovering error quaternion are less than 30 degrees in most cases. As such, the elevator and rudder control surfaces are rarely at full deflection. However, the pitch error extracted from the cruise-to-hover error quaternion is approximately 90 degrees. Incorporating the angular error into a proportional-derivative controller yields full elevator deflection from the start. As a result, the aircraft will rapidly gain momentum as it pitches from cruise mode to the hovering orientation. To kill the momentum, the derivative gain is multiplied by a factor of 3. The hypothesis is that this will prevent the aircraft from overshooting the hovering orientation, ending in a fatal result.

To test this hypothesis, an experiment was conducted outdoors in an open field. The human pilot loitered around the field in cruise mode and then flicked a switch on the transmitter to enable the onboard controller. This signaled the start of the autonomous transition and full elevator deflection was given by the controller. By substantially increasing the derivative gain, the rotation rate became the primary control factor. Therefore, the controller damped the rotation rate by cutting back on the elevator deflection, thus killing the momentum. The transition takes about a

Figure 5.11: The transition from cruise flight (left), through the stall regime (center), and into hover mode (right) is achieved autonomously.

second and is shown in Figure 5.11. From the experiments, the first hypothesis was confirmed. The aircraft did not exceed a pitch angle of ninety degrees when pitching up into the hovering flight mode.

5.4.2 Autonomous CTH Hypothesis 2

The transition from cruise flight to a hovering orientation can be achieved inside an urban structure.

When the aircraft is in horizontal flight just before starting the transition, it has maximum kinetic energy. As the plane makes the transition and begins to gain altitude, the kinetic energy is converted to potential energy. It is not until all of its kinetic energy is converted to potential that the plane reaches a maximum altitude. With the human pilot controlling the throttle, however, it is believed that the vertical momentum can be regulated, thus allowing the maneuver to be pulled off in an enclosed area.

To test this hypothesis, a basketball gymnasium with a 25 foot ceiling was utilized. The procedure was similar to the outdoor flight tests in that the pilot manually flew the aircraft around the gymnasium in cruise mode. However, just before flicking the switch to enable the onboard attitude controller, the pilot had to precisely control the throttle. This was much different than the outdoor case where there was no risk

of the aircraft crashing into the ceiling.

As the pilot enabled the autonomous flight controller, the plane began the transition to hover mode autonomously. However, it was noticed that the transition was not as smooth as it was outdoors. That is, there was a significant amount of overshoot in the aircraft's pitch angle (see Figure 5.12). The controller was still able to recover and stabilize the aircraft in the hovering orientation. The reason for the overshoot was that as the aircraft started gaining altitude, the pilot cut back significantly on the throttle to compensate. This resulted in a large decrease in airflow over the control surfaces and thus the elevator could not provide enough force to completely kill the momentum as the plane reached the hovering orientation. It seems there may be a need for autonomous altitude hold and this is also revisited in the section 5.5.

5.5 Hypotheses Revisited

Based on the initial hovering and cruise-to-hover experiments, additional challenges were revealed. First, it was obvious that while the torque roll during a hover did provide panoramic footage, it was impossible to interpret in real time because of the fast rotation rate. Second, the autonomous cruise-to-hover transition experiments showed the need for altitude control. These two demands are addressed and incorporated into the low level flight controller.

5.5.1 Torque Roll Control

As originally thought, the torque roll did not affect the stability of the aircraft during a hover. That is, the MAV was still able to remain in the vertical position despite the rotations resulting from the motor torque. However, if the hybrid MAV was to be used in the field for surveillance and reconnaissance purposes, the view from the onboard wireless camera would have a dizzying effect as the plane was rotating

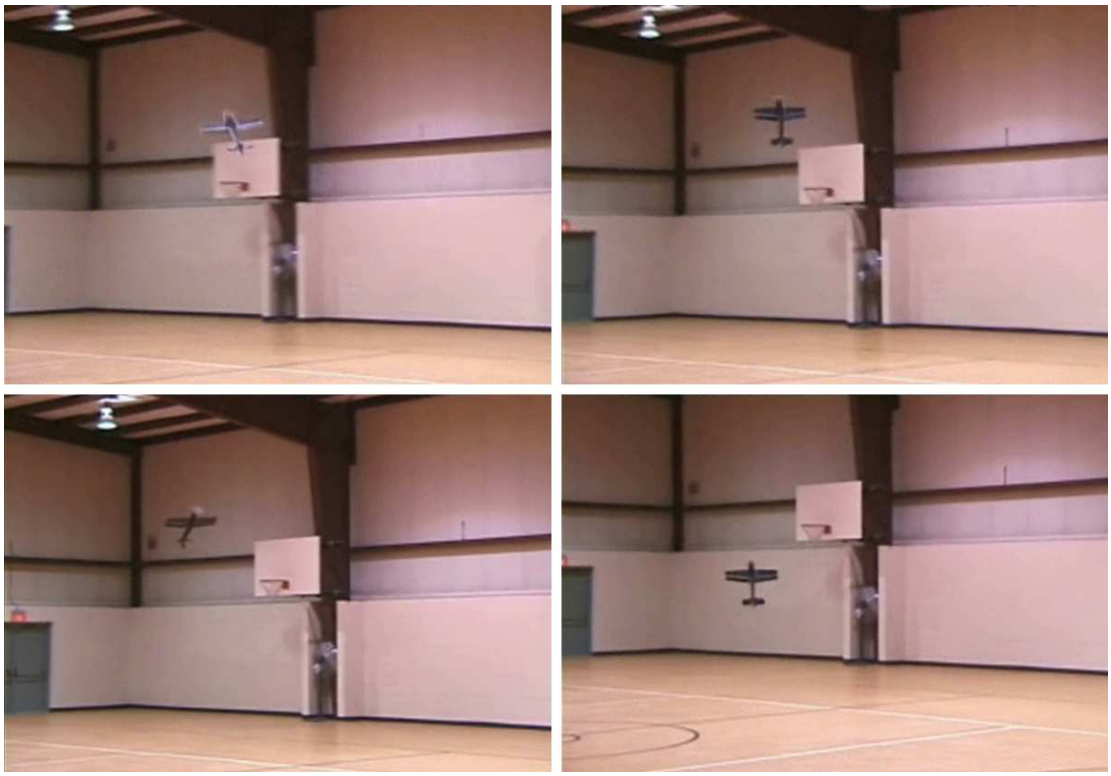

Figure 5.12: The transition from cruise flight into hover mode is demonstrated inside an urban structure (top). During the transition, the throttle is decreased to prevent the plane from colliding with the ceiling. This causes the aircraft to overshoot the vertical orientation (bottom left). The flight controller is able to recover and stabilize the MAV in its hovering orientation (bottom right).

at a rate of more than 20 rpm. Since the original aileron surface area did not create enough torque to counter the rotation when fully deflected, other alternatives had to be investigated. Also, to keep the cost and weight of the aircraft at a minimum, counter-rotating propeller were to be used as a last resort.

The first and most obvious approach was to increase the aileron surface area by lengthening them in the direction of the wing chord. However, this was not effective for several reasons. The first is that the propeller wash during a hover only flowed over approximately 40 percent of the ailerons. Second, a longer aileron when fully extended caused some airflow to completely miss the tail. This significantly affected

attitude regulation during a hover. Finally, fully deflecting the ailerons created an adverse yaw effect which caused the airplane to drift when hovering.

The second approach was to mount miniature DC motors with propellers on each wingtip. The motors were positioned to produce a thrust force in opposite directions which generated a rotational force countering the motor torque (see Figure 5.13). The wingtip motors are GWS EDP-20s which provide 23 grams of thrust with a 2510 direct drive propeller at 7.2 volts. With the same error quaternion used in the autonomous hovering experiments, the angular error about the aircraft's x-axis was now incorporated into the flight controller. Using this parameter, PID control was implemented on the error. This determined the length of the PWM signal being output to the brushed speed controller. A schematic of the system components and interface for autonomous hovering with torque roll regulation is shown in Figure 5.14.

With the above setup, autonomous hovering experiments were conducted with torque roll control. Figure 5.15 shows the torque-controlled condition in which the plane remains in a relatively constant orientation. This can be compared to Figure 5.8 in which the MAV completes 7 full revolutions in the same amount of time.

5.5.2 Altitude Hold

Without reliable GPS signals in these environments, altitude control is a challenging task. Furthermore, the scope of the MAV's flying domain includes the insides of urban structures and thus altimeters are inefficient. Both ultrasonic and infrared sensors were investigated for altitude hold. The infrared sensors proved to be too noisy (even after filtering) to achieve successful results and thus ultrasonic sensing was selected. The MaxSonar EZ-1 ultrasonic sensor was selected because of its 6 meter range, 2.5 cm resolution, digital output, and 4.5 gram weight.

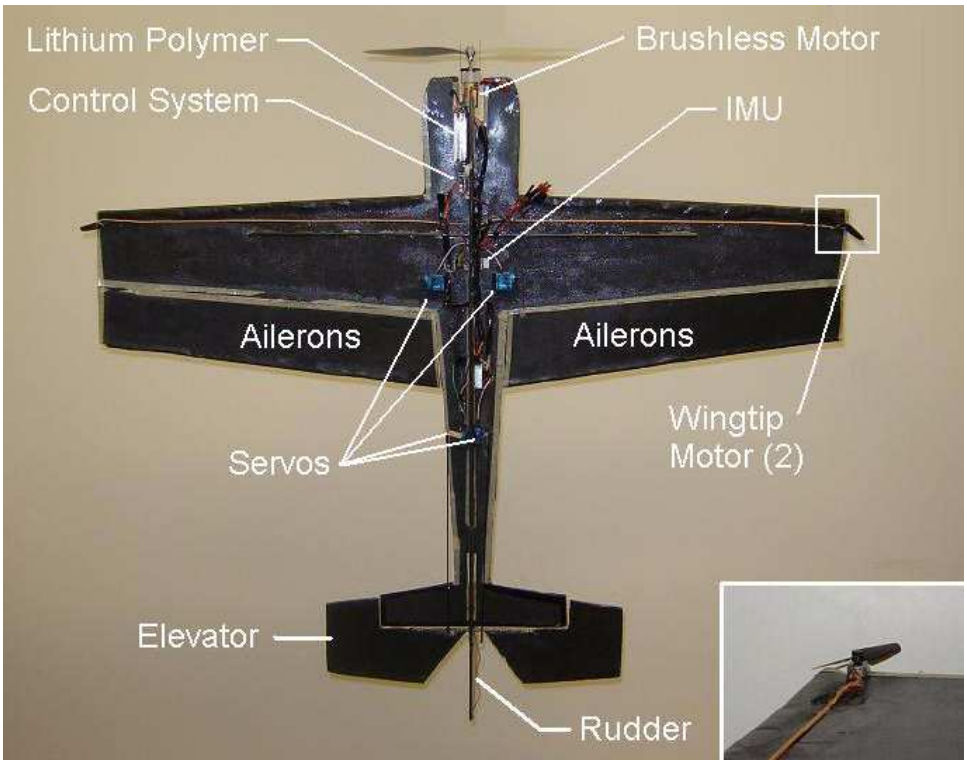

Figure 5.13: Two DC motors are added on each wingtip to counter the motor's reactive torque. *Inset*: Zoomed in view of the wingtip motor.

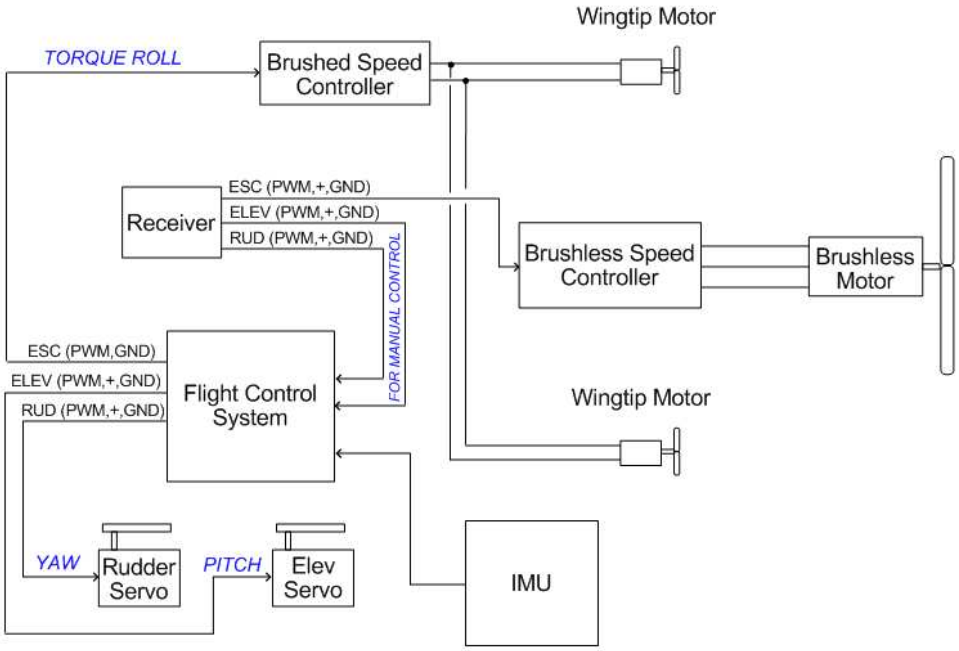

Figure 5.14: Schematic showing the system interface during an autonomous hover with torque roll control.

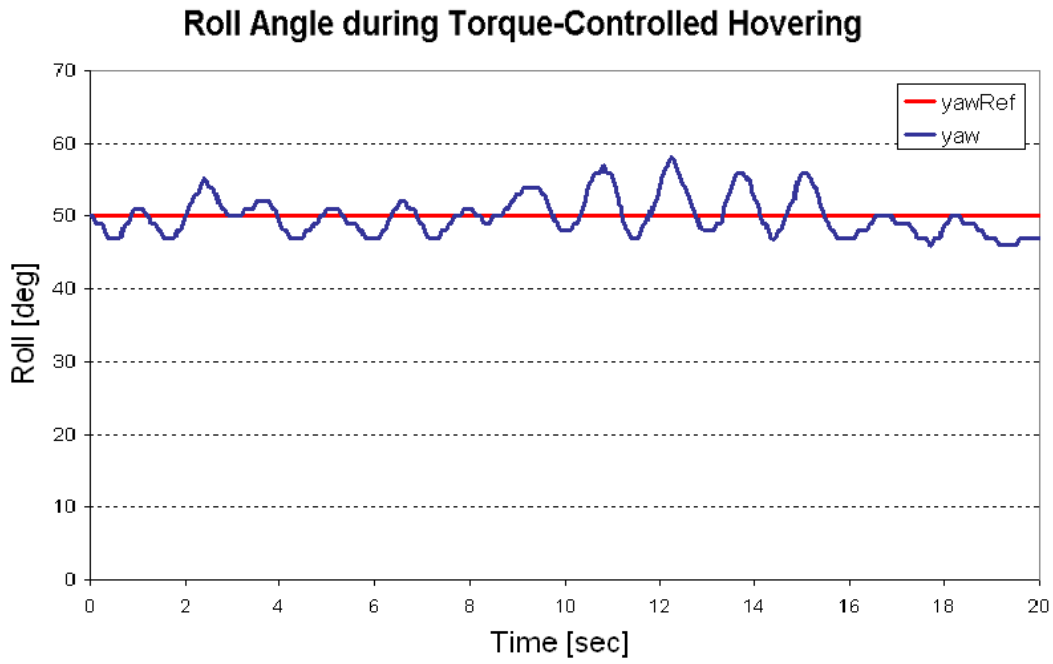

Figure 5.15: Roll angle captured during autonomous hovering with torque roll control.

The ultrasonic sensor had to be mounted on the hybrid prototype so that it would not be occluded when the elevator and rudder control surfaces were deflected. Furthermore, the mounting arm had to be designed so that it did not obstruct elevator and rudder deflection. The arm was created out of balsa wood and is shown in Figure 5.16.

With the ultrasonic sensor securely mounted on the tail, a controller for fully autonomous hovering could now be implemented and tested. A PID controller with a setpoint height of 36 inches was built upon the torque-controlled hovering algorithm of Section 5.5. Initial experiments showed that a noisy sample would randomly penetrate the ultrasonic height data making it difficult for the controller to regulate altitude. As such, an Exponentially Weighted Moving Average (EWMA) filter was implemented

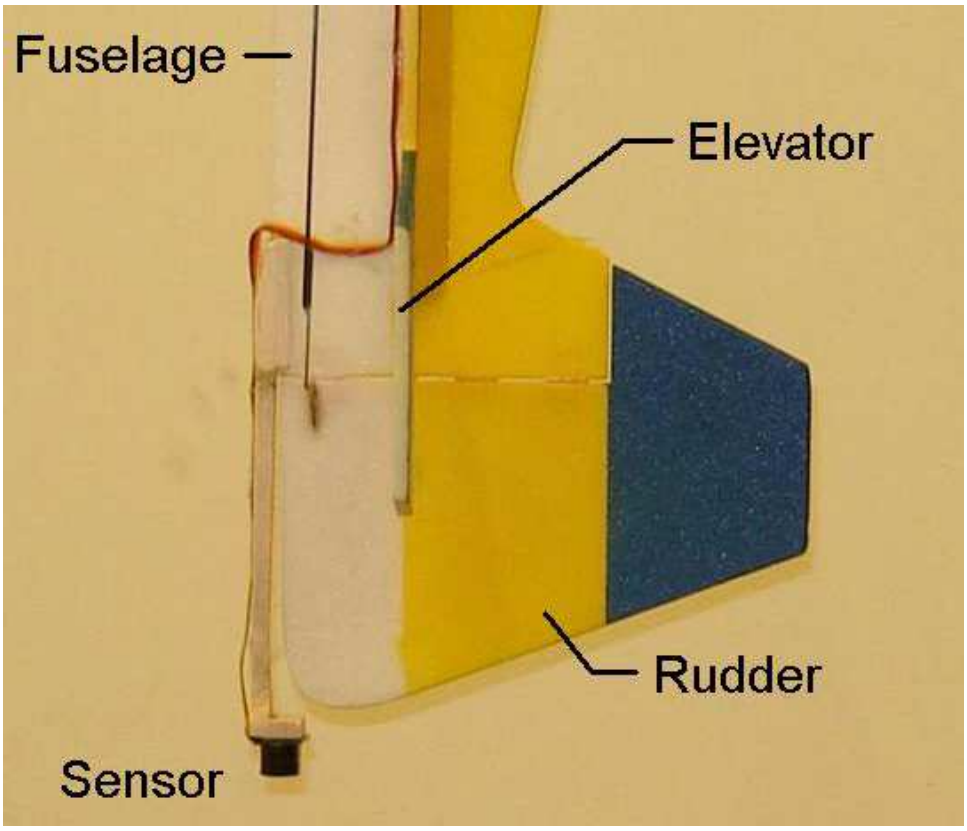

Figure 5.16: A mount was created for the sonar sensor so that it would not interfere with the elevator and rudder control surfaces.

to dampen the response to the outliers.

$$x_k = \alpha x_{k-1} + (1 - \alpha)x_k \tag{5.1}$$

where $0 \leq \alpha \leq 1$ represents the effect the filter has on the output. The higher the value of α, the more the data is filtered and vice versa. A value of 0.80 was used to filter the ultrasonic sensor data. Furthermore, the throttle input was bounded to prevent the aircraft from losing or gaining altitude too quickly.

The next set of experiments were performed using filtered ultrasonic data and

Figure 5.17: The first two images in the above sequence show the hybrid MAV in a fully autonomous hover at a height of 36 inches at 6 seconds apart. In the third image, a board was placed under the MAV's tail which caused the controller to adjust the MAV's height to 36 inches above the board. This was used to show that a constant throttle setting was not used to perform altitude hold.

represent the first documented results[3] of fully autonomous hovering of a fixed wing MAV. The results of the experiment are shown in the first two images of Figure 5.17. Furthermore, to show that the throttle was not set at a fixed position to balance the aircraft weight, a board is placed under the tail. This causes the FCS to adjust the aircraft's height to 36 inches above the board as seen in third image of Figure 5.17. The ultrasonic data from the tail mounted sensor is shown in Figures 5.18.

[3]To the best of the author's knowledge

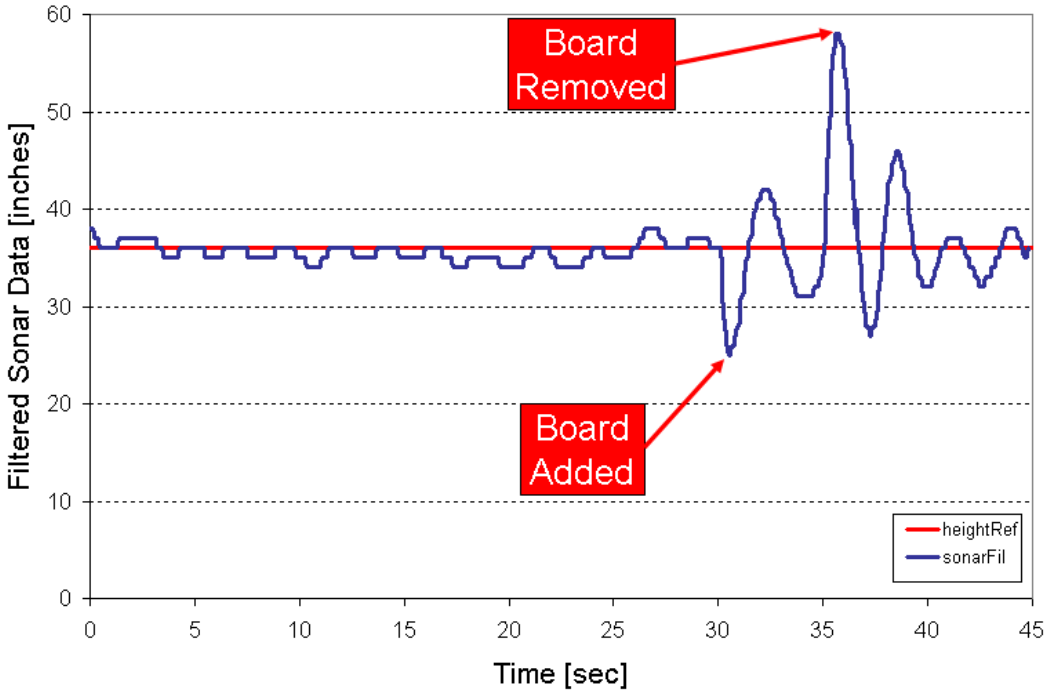

Figure 5.18: The raw sonar data is plotted over the course of 20 seconds of fully autonomous hovering. The reference height value was set to 36 inches. In the next 20 seconds, a board is placed under the aircraft to prove that the throttle is not set at a constant value to balance the aircraft weight.

6. Sensing and Control in Near-Earth Environments

The multiple flight modes of the hybrid platform make it well suited for achieving reconnaissance missions in near-Earth environments. This chapter describes a collision avoidance sensor suite used in conjunction with a high level navigational controller to detect an open doorway along the exterior of an urban structure. Furthermore, the integrated system is able to traverse the doorway to gather reconnaissance inside the building. The navigational controller is built on top of the low level attitude controller discussed in the previous chapter. The following sections describe the mission in more detail, sensor selection, and the multimodal controller used to achieve the building ingress and reconnaissance mission autonomously.

6.1 The Notional Mission

> There is suspicious activity reported at a large one-story building. The environment is potentially hostile and the hybrid platform is called upon to gather reconnaissance of the area. The MAV loiters around the perimeter of the building in cruise mode and streams wireless video back to a command and control station. An open doorway is detected in the video and the hybrid prototype is commanded to transition to hover mode and gently maneuver itself through the doorway and into the building for a closer look. Once inside, video from the MAV's onboard wireless camera was transmitted to a ground station located outside the target perimeter. This mission is demonstrated by an expert human pilot under full manual operation (see Figure 6.1).

Figure 6.1: A fixed-wing MAV transitions to hovering mode to gently maneuver itself through a small opening of an urban structure. *Inset*: once inside, the onboard wireless camera is used to capture and transmit surveillance images.

The final goal of this thesis is to perform this mission autonomously. However, it will be broken down into a combination of wall following, doorway detection, and reactive control to enter the building. Looking at the building from the top view as in Figure 6.2, the MAV will begin by implementing a wall following algorithm to translate along the exterior wall of the building towards the doorway. Once the door opening is detected, the aircraft must stabilize itself in the hovering orientation and kill any forward momentum. Finally, the MAV will traverse the doorway and gather reconnaissance inside the building. A sophisticated sensor suite and control system is required to achieve this mission without any human intervention. Several sensing technologies will be investigated including optic flow, LADAR, ultrasonic, and infrared. Once a sensor suite is selected, it will be mounted on the MAV, interfaced with the flight control system, and used to achieve the mission autonomously.

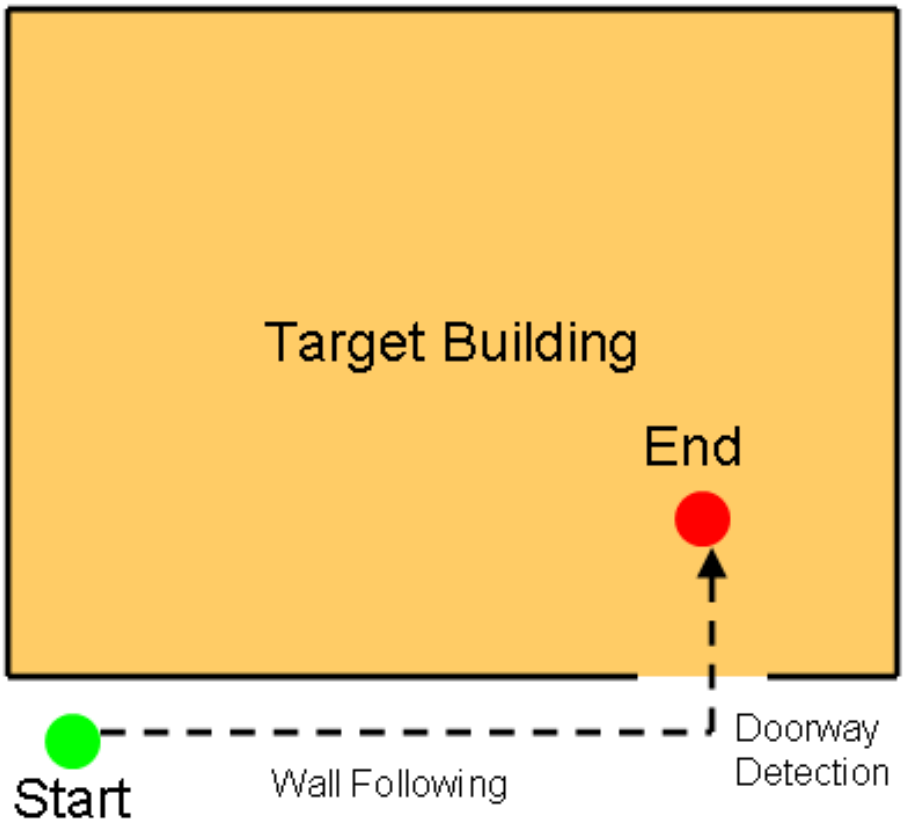

Figure 6.2: The top view of the target building is shown to help visualize the goal of the final experiment.

6.2 Sensing

For inspiration towards autonomous MAV navigation in near-Earth environments, the authors looked to nature. Flying creatures such as insects, birds, and bats have unique sensing capabilities to navigate in complex and dynamic surroundings. For example, flying insects such as honeybees and fruit flies use optic flow [15]. By leveraging previous research used to perform autonomous collision avoidance and landing with a MAV [20], optic flow will be investigated as a viable option for the hybrid prototype. Furthermore, it is well known that bats navigate in caves and forests by emitting ultrasonic pulses. Small and lightweight ultrasonic sensors can

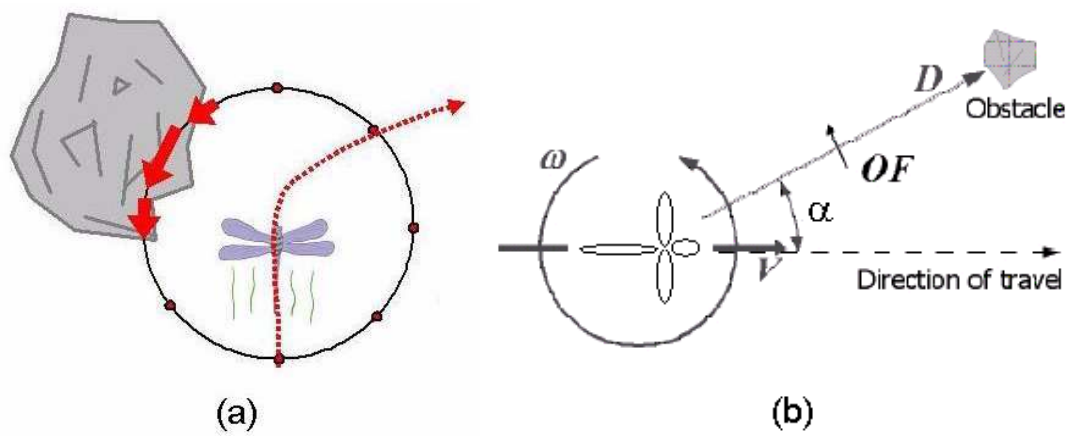

Figure 6.3: (a) Dragon fly saccading away from regions of high optic flow in order to avoid a collision. (b) One-dimensional optic flow during insect flight.

be arranged in an array to cover a large field of view around the MAV and mimic the sensing capabilities of bats [26]. In addition, other sensing alternatives will be investigated such as laser scanners, laser rangers, and infrared sensors.

6.2.1 Optic Flow

Insects perform tasks such as collision avoidance and landing by perceiving the optic flow of their surroundings [53]. Optic flow refers to the apparent motion of texture in the visual field relative to the insect's body. Through several experiments with honeybees [52] and fruit flies [57] [58], it is suggested that flying insects avoid collisions by turning away from regions of high optic flow (see Figure 6.3a).

This can be seen theoretically from the one-dimensional optic flow equation originally derived in [60]

$$OF = \frac{V}{D}\sin\alpha - \omega \tag{6.1}$$

where optic flow is measured in rad/sec and is a function of the insect's forward velocity, V, angular velocity, ω, distance D from an obstacle, and the angle, α, between the insect's direction of travel and the obstacle (see Figure 6.3b). As the

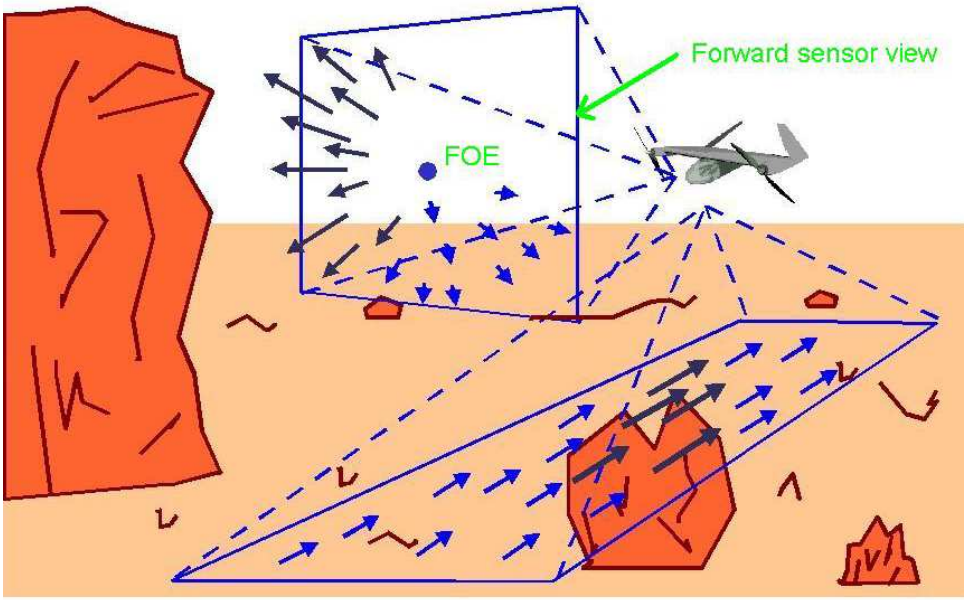

Figure 6.4: Optic flow as seen by aerial robot flying above ground. Reprinted from *www.centeye.com*.

obstacle approaches (i.e. D decreases), the optic flow magnitude increases.

This same principle can be applied to MAVs traveling in straight paths [3] as shown in Figure 6.4. If an optic flow sensor is mounted on the nose of the MAV, the focus of expansion (FOE) in the forward sensor view indicates the direction of travel. If the FOE is located inside a rapidly diverging region, then a collision is imminent. A rapidly expanding region to the right of the FOE like the one seen in the Figure 6.4, corresponds to an obstacle approaching on the right side of the MAV. Thus, the MAV should turn left to avoid the collision, or away from the region of high optic flow. Similarly, the MAV can estimate its height from a downward-facing optic flow sensor mounted on the belly of the aircraft (e.g. faster optic flow indicates a low flight altitude). By equipping a MAV with sensors capable of measuring the optic flow in front of and below the aircraft, the above flight patterns can be embedded in a control system for autonomous collision avoidance and landing.

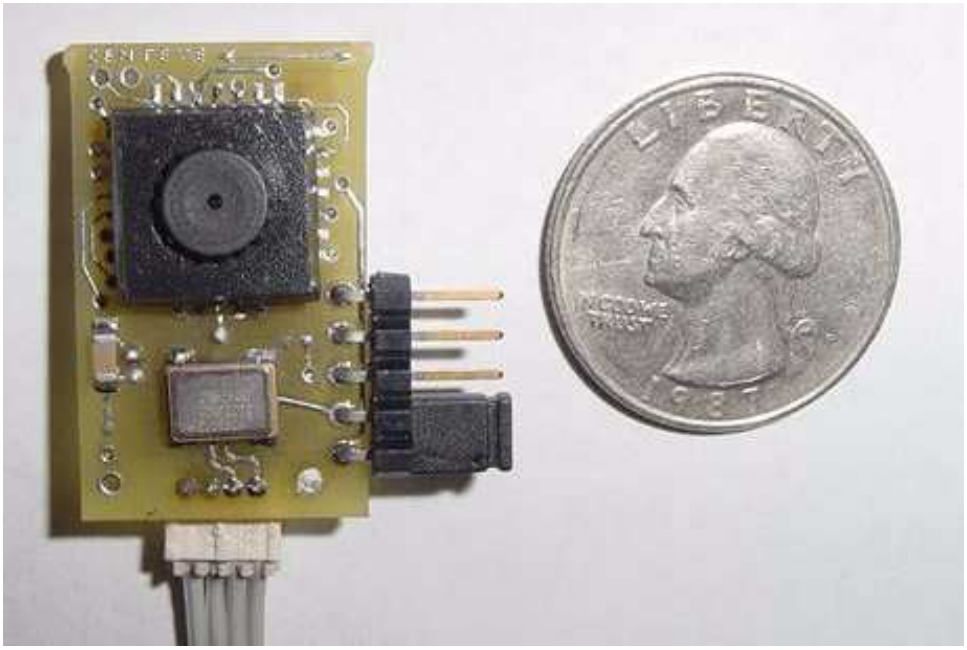

Figure 6.5: mixed-mode VLSI optic flow microsensor is slightly bigger than a US quarter. Reprinted from *www.centeye.com*.

Autonomous Collision Avoidance

Mimicking behaviors of flying insects required optic flow to be measured in front of the aircraft to detect oncoming collisions. Optic flow microsensors developed by Centeye, Inc. [5] were used in the experiments. The sensors weighed 4.8 grams, grabbed frames up to 1.4 kHz, and measured optic flow up to 20 rad/s (see Figure 6.5). By orienting the sensors at $\pm$ 45 degrees from the fuselage, optic flow fields were detected on each side of the aircraft. Equation (6.1) was used to set an optic flow threshold that corresponded to D being twice the turning radius of the aircraft. The threshold assumed cruise conditions (i.e. V=const. and ω=0) and was preset experimentally.

The aircraft was then flown towards different obstacles and an approaching object on either side of the MAV would generate an increase in optic flow as seen in Equation (6.1). The output of each of these sensors was fed into an early version of the onboard

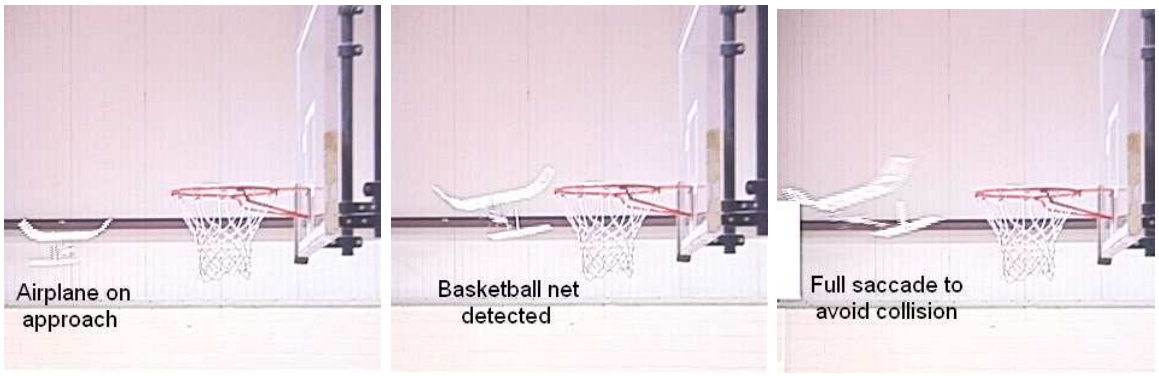

Figure 6.6: Optic flow is used to sense when an obstacle is within two turning radii of the aircraft. The aircraft avoids the collision by fully deflecting the rudder.

flight control system described in Chapter 5. If the values from either of the sensors exceeded the threshold, the processor would apply full deflection to the rudder to avoid the collision. By implementing this reactive-based method, autonomous collision avoidance was successfully demonstrated (see Figure 6.6).

Autonomous Landing

Flying insects, such as honeybees, land by keeping the optic flow on the landing surface constant. It is possible to autonomously land a MAV by mimicking this behavior. When measuring the optic flow on the landing surface, the obstacle in Figure 6.3b is now the ground and thus $\alpha = 90$ degrees. To further simplify this task, the rotational component of optic flow arising from changes in aircraft pitch are assumed smaller than the translational component. Thus, Equation (6.1) reduces to

$$OF_{ground} = \frac{V}{D} \tag{6.2}$$

Keeping Equation (6.2) constant demands the aircraft's control system decrease forward speed (V) in proportion to altitude (D). When approaching a landing, the embedded microcontroller will implement a function to gradually throttle down the

motor while continuing to take optic flow readings throughout the landing process. The control algorithm (see Figure 6.7) starts by computing the error between the desired and measured optic flow. When the optic flow on the landing surface becomes larger than the desired optic flow, the error is negative and two conditions are possible. One, the forward velocity, V, could be significantly increasing which is not possible based on the motor function. Two, the altitude (D) can be decreasing at a faster rate than the forward velocity (V). Here, the controller sends a signal to the elevator to decrease the vehicle's descent rate based on the error magnitude. The other possibility is that the measured optic flow could start to dip below the desired value causing the error to be positive. The two possible cases that arise here are one, the altitude (D) is increasing but again this is not possible while in landing mode and two, the velocity (V) is decreasing faster than altitude (D). In this case, the controller commands the elevator to increase the descent rate. Figure 6.8 shows the results of the autonomous landing experiments.

Optic Flow Limitations

The proof-of-concept experiments showed promising results for using optic flow as a means of perception in near-Earth environments, however, there are some limitations. For example, when two optic flow sensors are aligned at 45 degrees from the fuselage like in the experiments above, smaller objects such as poles could remain outside the sensor's field of view (see left part of Figure 6.9). Similarly, optic flow-based collision avoidance is also inefficient when flying directly towards larger, homogenous obstacles such as walls (see right part of Figure 6.9). Surfaces which are low in texture and uniform in color will yield small optic flow fields. These scenarios are most likely why honeybees never fly a straight line towards a target, but rather make a slight zigzag pattern. This generates an artificial parallax that will yield optic flow values for smaller oncoming obstacles and large surfaces which are low in texture.

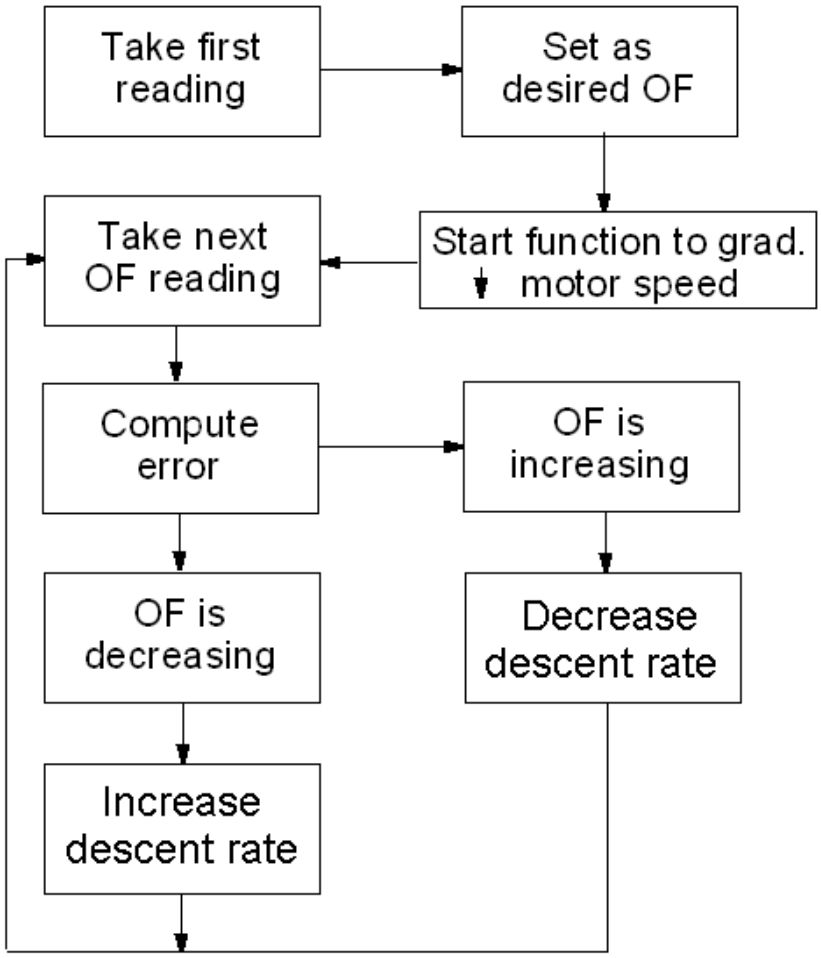

Figure 6.7: Flow chart of landing control system.

These limitations are further evidenced in [62], where the diverging optic flow field generated by the wall was used to trigger a warning two meters before the collision. However, the experiment was performed in an artificially textured environment (i.e. alternating white and black sheets were used as walls). Walls are often homogeneous and have little texture. Therefore, this method alone will not be sufficient in more realistic environments. Also, in one experiment in [22], optic flow sensors were used to calculate the distance to obstacles on the side of the MAV. In the second experiment where the MAV started out by heading right towards a building, a laser ranger was

Figure 6.8: The optic flow on the basketball gym floor is kept constant by the control system. That is, the aircraft (encircled) forward velocity is decreased in proportion with its altitude to land smoothly. Left: Aircraft just after hand launch. Middle: Aircraft midway through landing sequence at proportionally lower altitude and velocity. Right: Aircraft comes to a smooth landing within 25 *meters* from starting point.

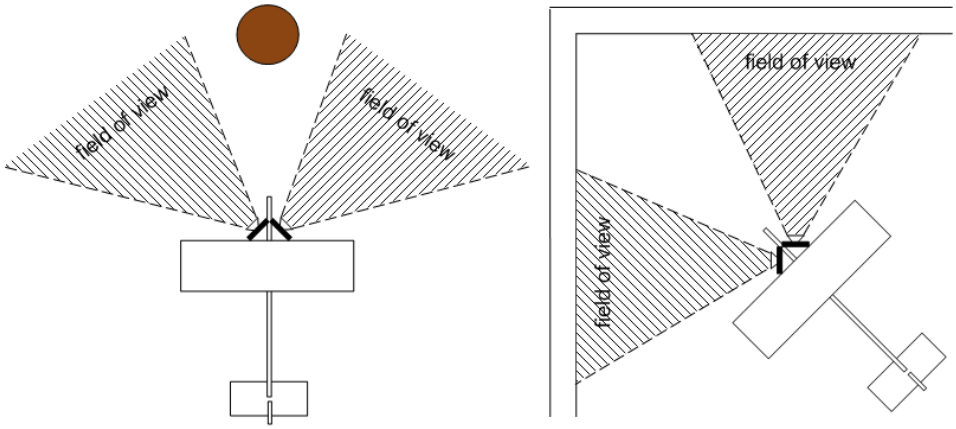

Figure 6.9: Limitations of using optic flow for navigation.

used instead of optic flow for obstacle detection. Furthermore, this experiment was performed outdoors with lots of flying space.

In addition to the limitations discussed above, optic flow is a computer vision technique and is thus affected by changing or poor lighting conditions. Also, optic flow sensors will not be suitable for wall following because an accurate measurement of the MAV's velocity is required to calculate distance in Equation 6.1. Therefore, other alternatives will be investigated for the building ingress and reconnaissance mission.

6.2.2 Laser Scanners and Rangers

Laser scanners are range and bearing sensors that can acquire large slices of a robot's environment multiple times per second. The most widely used version of these sensors in robotics is the SICK Laser Measurement Sensor (LMS) [1] [2] [4] [7] [24] [54]. The SICK LMS scans 180 degrees of the environment and can detect objects out to 80 meters. At an angular resolution of 1 degree, scans can be acquired at a rate of 75 Hz. Higher angular resolutions are achievable but at the expense of the scan frequency. The SICK LMS is a very robust and useful sensor for collision avoidance in near-Earth environments, but its 4.5 kg mass exceeds the payload capacity of most miniature UAVs including the hybrid prototype.

Recently, a smaller and lighter laser scanner was released by Hokuyo. The URG-04LX weighs 160 grams and occupies a volume which is 35 times smaller than the SICK scanner. With a 240 degree scan angle, the Hokuyo covers a larger range than the SICK but only has a 10 Hz scan rate. It can detect objects which are 4 meters away with a measurement and angular resolution of 1mm and 0.4 degrees, respectively. Even though the Hokuyo sensor weighs significantly less than the SICK laser scanner, it is still beyond the payload capacity of the hybrid prototype. Furthermore, tests with the Hokuyo sensor revealed it was extremely sensitive when compared to its SICK counterpart [48].

Another option that was investigated was to use the MAV's torque roll and a simple laser ranger to mimic the more expensive and heavier laser scanners. That is, a one-dimensional laser ranging sensor could be mounted on the aircraft's belly and rotating the aircraft around the vertical axis during a hover would simulate the rotating mirror effect of the laser scanner. However, controlled translation while the MAV was torque rolling would be very challenging and thus, this concept was not selected. The net result is that while laser scanners have helped push the field

of robotics forward, a small laser scanner as robust as the SICK LMS and within payload limitations of miniature UAVs does not yet exist.

6.2.3 Ultrasonic and Infrared Sensing

Ultrasonic and infrared sensing have played an integral role in robotics research for environmental perception. The advantages and disadvantages of each sensor are well known. For example, the wide beam transmitted by ultrasonic sensors results in poor angular resolution. This causes small openings such as doorways to be overlooked by the sensor. Furthermore, small obstacles such as a 1-inch diameter pole can appear to be 3 feet in width due to the sensor's poor angular resolution.

Alternatively, infrared sensors have a very narrow transmission beam and are therefore effective at detecting small openings and edges. However, they can be fairly inaccurate or unstable when it comes to measuring distance. The disadvantages of infrared and ultrasonic sensors can be improved by fusing the two sensing technologies together. This was shown in [12] where infrared and ultrasonic sensors were used in a complementary fashion to map out walls, doors, and windows of a residential basement.

These same principles will be applied to perform wall following and doorway detection in the final experiment. However, since more than one of each sensor will be used for panoramic perception, small and lightweight packages must be selected. The same ultrasonic sensor used for altitude hold (i.e. MaxSonar EZ-1) will be used for lateral distance estimation to the wall. The infrared sensor selected was the Sharp Long Range Distance Measuring Sensor (e.g. GP2Y0A02YK). It is an analog sensor with a range of 20-150 cm and weighs just 10 grams.

6.3 Sensor Suite

To achieve the experiment discussed earlier in this chapter, the hybrid MAV must be able to follow the exterior wall of the building until it detects the doorway, stabilize itself in the hovering flight mode so that its momentum does not carry it past the doorway, and traverse the doorway to enter the building. Based on the evaluation of various sensors in the previous section, an ultrasonic and infrared sensor suite will be developed and interfaced with the flight control system.

In addition to the IMU and tail-mounted ultrasonic sensor for altitude control, two MaxSonar EZ-1 ultrasonic sensors and two Sharp GP2Y0A02YK infrared sensors will be incorporated into the sensor suite for wall following and doorway detection. When determining where to mount the sensors, there were two critical factors that had to be evaluated. The first was determining which orientation the plane should be in during wall following and the other was the minimum detection distance of the sensors.

6.3.1 Wall Following Orientation

Two options were possible when determining which orientation the MAV should follow the wall in. The MAV's wing axis could be parallel to the wall where a yawing motion would create translation in the direction parallel to the wall (see Figure 6.10a). The other option was to have the wing plane perpendicular to the wall being followed (see Figure 6.10b). This meant that a slight rotation about the pitch axis would result in translation parallel to the wall.

The orientation shown in Figure 6.10a would require a pitch forward maneuver to traverse a doorway. This meant that the width of the doorway would have to be slightly larger than the MAV's wingspan. However, the cross section for the orientation shown in Figure 6.10b is significantly smaller. Therefore, when yawing

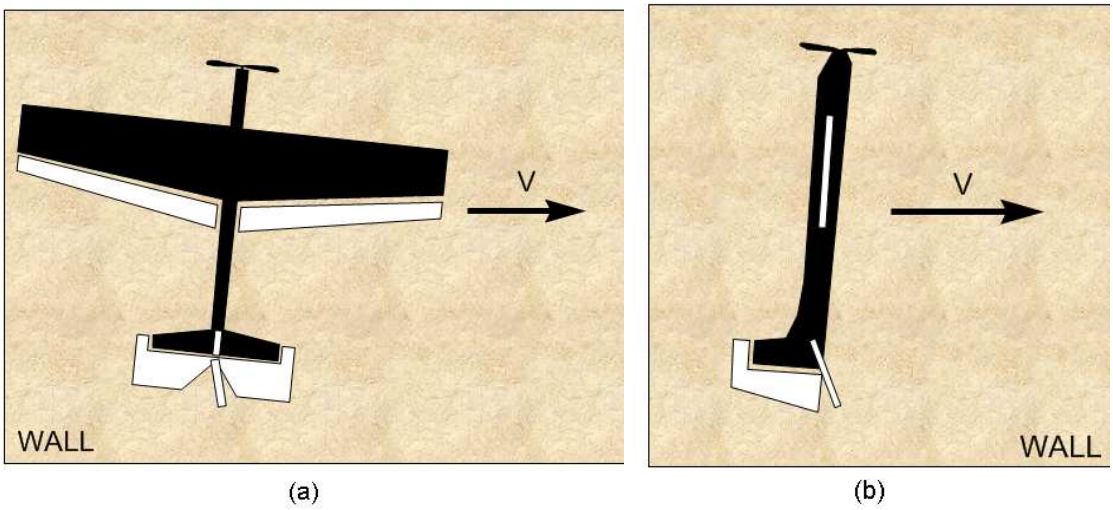

Figure 6.10: (a) One possible orientation the MAV can perform wall following is with the wings parallel to the wall. (b) The other is with the wing plane perpendicular to the wall.

through a doorway, there would be more room for error. Furthermore, the aircraft is more stable when following a wall with the wing plane perpendicular to it and was therefore chosen as the wall following orientation.

6.3.2 Sensor Location

Both the ultrasonic and infrared sensors have a minimum detection, or blind, distance. The blind distance for the ultrasonic sensors is 15 cm which means the sensor will return 15 cm for any obstacle that is within 0-15 cm from it. Therefore, mounting it on the tip of each wing could have fatal results. For example, if the aircraft is flying in hovering mode and an obstacle is dangerously close to the wing (i.e. 3 cm), the ultrasonic sensor would still return a value of 15 cm. To prevent this, the sensor was initially mounted on the fuselage near the aircraft's center of gravity. At this location, the blind distance of the sensor was shielded by the wing. However, it was later realized that the propeller wash and frequency were severely affecting the

performance of the sensor.

This phenomenon was further investigated in a repeatable experiment. An ultrasonic sensor was mounted on the aircraft's fuselage about 30 cm away from the propeller. The aircraft is oriented such that the sensor is aimed directly at a flat wall. The sensor is initially 75 cm from the wall and is carried on a straight path perpendicular to the wall until it reaches a distance of 280 cm. It is then carried back towards the wall on the same path until it reaches the starting point (i.e. 75 cm from the wall). Each trial was conducted with the propeller off and then again with the propeller spinning at the approximate angular velocity of the hovering flight mode. It can be seen in Figure 6.11 that the propeller has a large effect on the raw sensor output. Both high frequency noise and inaccuracies are introduced into the measurements. It was therefore concluded that the sensor should be mounted as far away from the propeller as possible. With an ultrasonic sensor already mounted on the tail for altitude hold, the most optimal position for the wall following ultrasonic sensors was at the base of the fuselage (see Figure 6.12). Like in the previous mounting position, the minimum detection distance does not become a factor because the wing extends out 0.5 meters and is therefore used as the threshold for the sensor.

The minimum detection distance for the infrared sensors is 20 cm. However, they are not affected by the propeller and can therefore be mounted on the aircraft's wings. To account for the 20 cm blind spot, the infrared sensors are moved in this exact distance from the tip of the wing (see Figure 6.12). Therefore, the wing prevents any object from entering the sensor's blind region.

6.4 Dual Processor Flight Control System

The flight control system was upgraded to a dual processor board (see Figure 6.13). The additional PIC16F877 microcontroller acts as a low level processor by performing

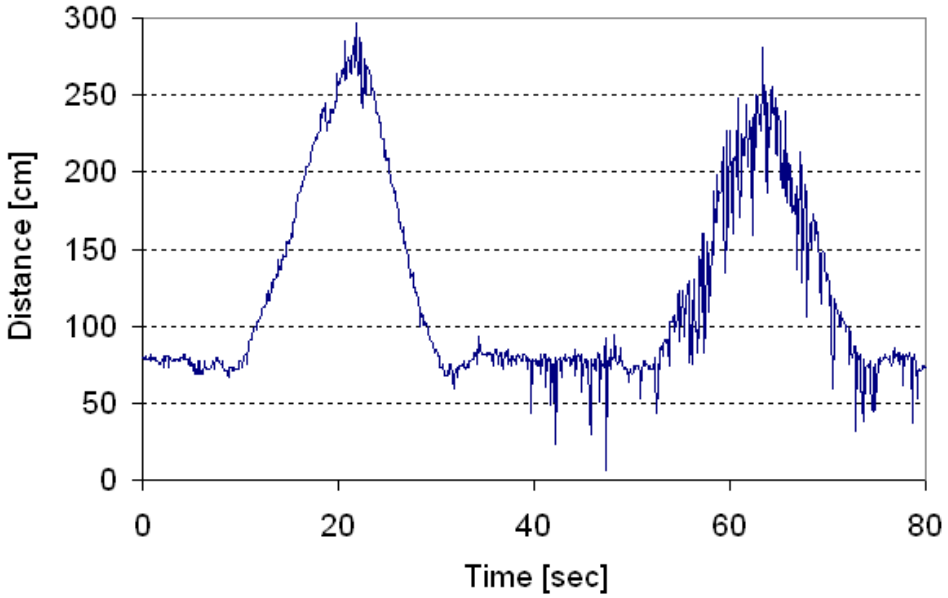

Figure 6.11: Raw ultrasonic data is collected with the propeller on and off. It can be seen that the propeller severely affects the performance of the sensor.

sensor data acquisition and communicating the raw sensor data back to the main processor via RS-232 protocol. While the IMU is still interfaced directly to the main processor, the low level processor is responsible for three digital ultrasonic and four analog infrared sensor ports.

The communication between the low and high level processors is achieved with RS-232 cross-communication and hardware interrupts. The low level processor will acquire data from a sensor and send it and an identifying signature to the main processor. These two bytes of data are transmitted sequentially. For example, the first byte sent to the main processor would be a value of 1 identifying it as sensor 1. The next byte would be the raw value from sensor 1. A hardware interrupt is set up in the main processor to collect the data from the low level processor when it is transmitted. This avoids having the main processor hang while it waits for data from the low level processor.

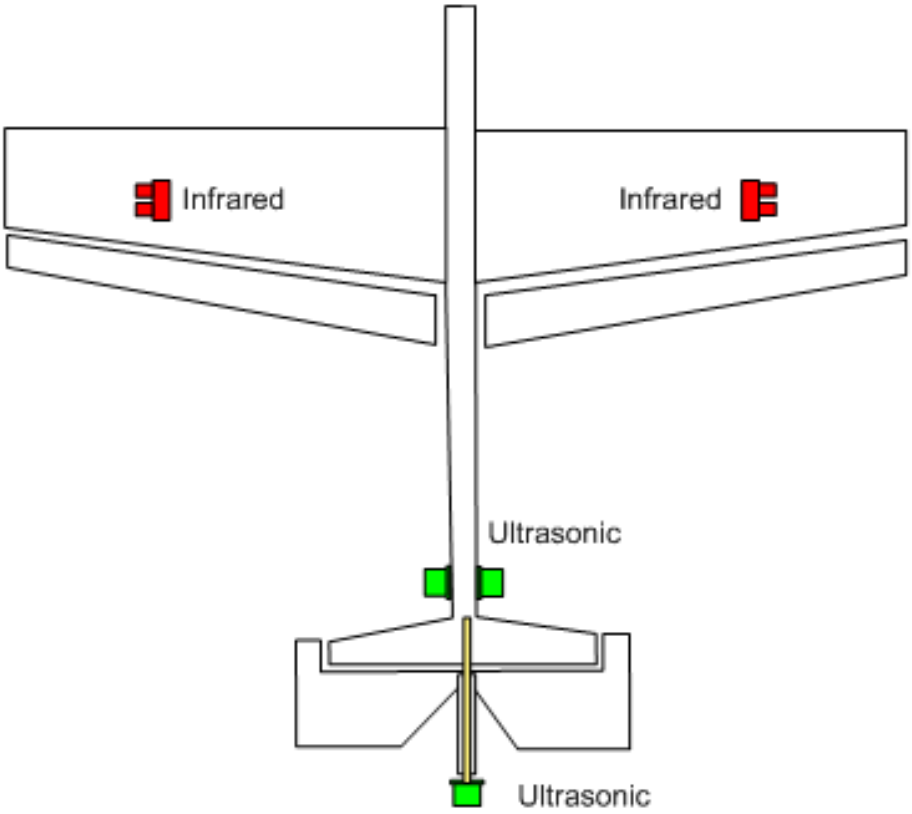

Figure 6.12: An infrared sensor is mounted on each wing pointing out from the fuselage. Also, an ultrasonic sensor is mounted at the base of the fuselage pointing outward. This is so the propeller wash does not affect the sensor reading.

6.5 Navigational Controller

The control algorithm for building ingress and reconnaissance consists of three different control modes including wall following, stabilizing, and traversing. Each control mode sends different commands to the pitch and yaw control surfaces while the wingtip motors and main motor are continuously being adjusted to keep the MAV's roll angle and altitude constant, respectively. The general structure of the navigational controller is illustrated in the following steps

1. Acquire IMU data to determine the current orientation of the aircraft.

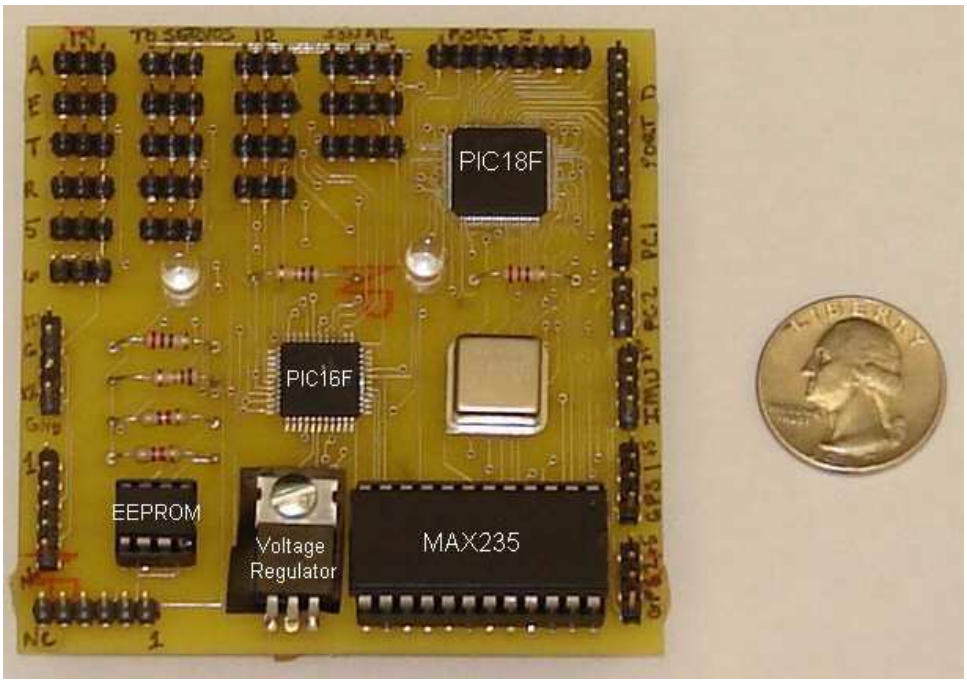

Figure 6.13: A flight control system was developed with dual processing; one for data acquisition and the other for control.

2. Use the angle about the roll axis of the MAV as the setpoint value for torque roll control (this step is only performed once).

3. Acquire sensor data from the low level microcontroller including the wing mounted infrared sensors, fuselage mounted ultrasonic sensors, and tail mounted ultrasonic sensor.

4. Filter and process the wing and fuselage mounted sensor data from (2) to determine the state of the navigational controller (e.g. wall following, stabilizing, or traversing).

5. Based on the navigational controller's state in (3), send the commanded pitch and yaw values to the attitude controller.

6. Filter the tail ultrasonic data and send to the altitude controller.

7. Return to (1).

The different modes of the controller are determined by the ultrasonic and infrared sensor data and are described in the next few subsections.

6.5.1 Wall Following Mode

Data from both the infrared and ultrasonic sensors are acquired by the low level microcontroller at a rate of 15 Hz. Because ultrasonic sensors have a wide beam and are therefore inefficient at detecting edges or doorways, the infrared sensor is primarily responsible for determining the mode of the controller. The controller enters *wall following mode* if an obstacle is detected by both sensors and is less than 1.4 meters away. The 1.4 meter threshold was set based on the 1.5 meter maximum detection distance of the infrared sensor. If the sensor detects an object within the 1.4 meter threshold, it is assumed to be a wall. If the sensor does not detect anything, it will output a value corresponding to 1.5 meters. In this case, the assumption is that there is an opening for the plane to transition through and the controller will then move to *stabilizing mode*. Once in *wall following mode*, the FCS still acquires data from both sensors but the control algorithm heavily weights the ultrasonic data to keep the MAV at a constant distance from the wall. This is because the ultrasonic sensor is much more accurate in measuring distance than the infrared sensor.

The wall following algorithm consists of two levels for yaw control and is shown in Figure 6.14. The high level yaw controller starts by using a setpoint distance, Y_{ref}, of 75 cm from the tip of the wing to the wall. This is compared to the filtered value from the ultrasonic sensor to calculate the error between the desired and actual distance from the wall. Proportional-derivative control is implemented on the error to determine the commanded yaw angle value, ψ_c. The commanded yaw angle is saturated between $\pm$ 5 degrees and added to the reference yaw angle (ψ_{ref} is the yaw angle for pure hovering and is calculated during the calibration process; ideally, this will be zero degrees). The resulting angle is then fed into the low level attitude controller from Chapter 5.

As the yaw controller is being implemented during each control loop, the aircraft

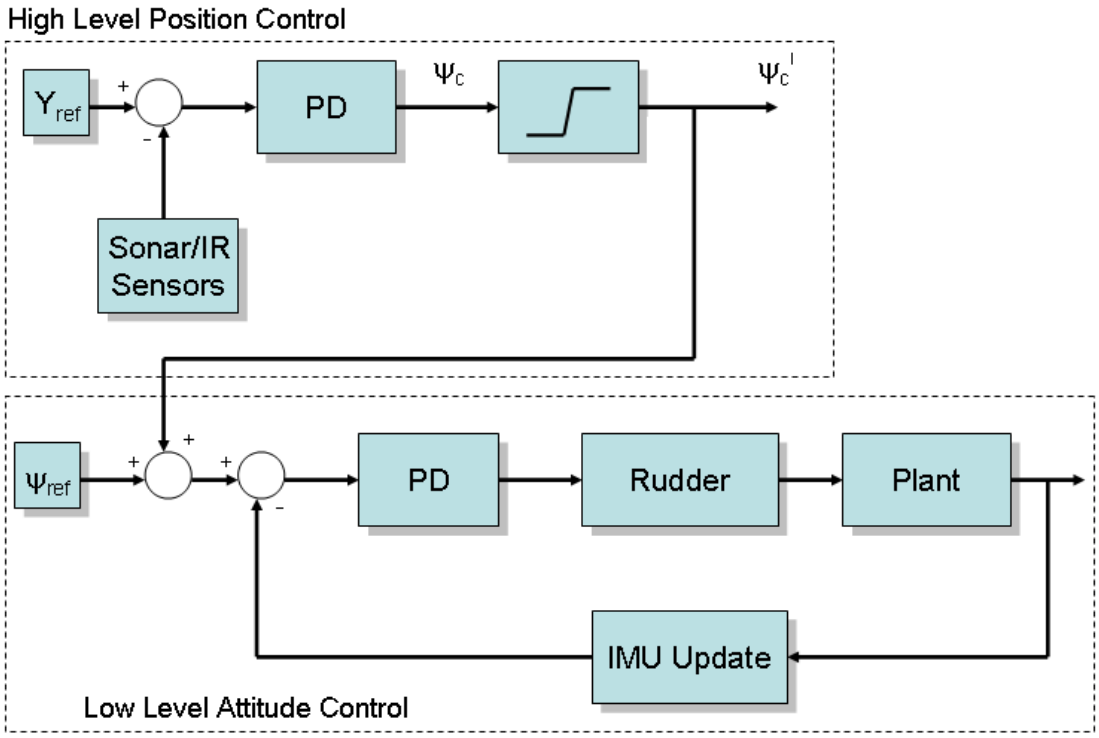

Figure 6.14: Two nested PD loops are used in the yaw controller during wall following.

must also be translating in the forward direction (i.e. parallel to the wall). For this part of the controller, a constant commanded pitch angle, θ_c, of negative 8 degrees (i.e. the negative pitch direction is forward from the vertical) is added to the reference pitch angle and fed into the low level attitude controller. Negative 8 degrees was chosen for the commanded pitch value because it corresponds to a translation speed of approximately 1 m/s.

6.5.2 Stabilizing Mode

Ultrasonic and infrared data is constantly being analyzed during *wall following mode* to determine when the transition to *stabilizing mode* should occur. This initiates when the infrared sensor exceeds a distance threshold of 1.4 meters for five consecutive control loop iterations. This is to allow the MAV extra translation time to get its

entire frame past the wall and also to rule out any noisy measurements.

The stabilizing control mode has two main functions. The first is to diffuse the forward momentum of the MAV so it dos not move past the doorway and the second is to get the aircraft back to the hovering orientation. To kill the forward momentum of the MAV, the controller increments the commanded pitch value by 0.75 degrees per control loop iteration. Initially at negative 8 degrees, it will take 11 loop iterations or close to 0.4 seconds to get back to the vertical orientation (i.e. $\theta_c = 0$). However, to ensure that forward momentum is eliminated, the controller pitches the aircraft a few degrees past the vertical orientation before bringing it back to a hover. Throughout this process which takes just over a second, the commanded yaw value (ψ_c') is set to zero. The controller then enters *traversing mode*.

6.5.3 Traversing Mode

After regaining stability in the vertical orientation, the *traversing mode* is executed. The traversing controller is just a simple reactive control algorithm used to yaw the aircraft into the detected opening, thus traversing the doorway. This process also acts as a failsafe to the wall following controller. That is, if the wall following controller allows the aircraft to get more than 1.5 meters away from the wall (i.e. an error of more than 75 cm), this will exceed the range of the infrared sensor causing the controller to incorrectly enter *stabilizing mode*. However, it will then enter *traversing mode* which will just bring the MAV back towards the wall until it reenters the detection range of the sensors. This will then force the controller back into *wall following mode*.

The process is initiated by setting the commanded pitch value to 0 degrees such that the MAV remains stationary in the direction parallel to the wall. The commanded yaw value is set to negative 7 degrees which corresponds to a translation

speed of about 1 m/s in the direction perpendicular to the wall (i.e. through the doorway). After maintaining a yaw left orientation for a few seconds, the traversing mode controller orients the aircraft back in the vertical attitude to acquire situational awareness of the building's interior.

6.6 Initial Experiments

The initial experiments were conducted inside an urban structure at Drexel University. These experiments were used to fine tune the gains for wall following and doorway detection.

6.6.1 Wall Following

The first experiment was used to evaluate the wall following portion of the controller. The trials were conducted along a wall 13 meters in length where the objective of the experiment was to maintain a 75 cm distance between the tip of the MAV's left wing and the wall, for the length of the wall. Because the ultrasonic sensor is located on the fuselage, this has to be factored into the setpoint distance. Furthermore, as the flight control system directs the aircraft toward the end of the wall, its wall following efficiency will be tested as it must negotiate a 2.5 meter passageway. With a wingspan of 1 meter, this leaves only 75 cm of error on each side of the aircraft's wing as it moves through the narrow opening.

The experiment begins with the human pilot orienting the aircraft's wings perpendicular to the surface of the wall. Then, the pilot flicks the auto/manual switch on the transmitter to enable fully autonomous operation. Upon releasing the aircraft, the high level microcontroller will perform the steps listed in Section 6.5. Figure 6.15 shows a sequence of images from the experiment. As the plane follows the 13 meter wall, it maintains its setpoint distances from the wall and floor as well as its attitude

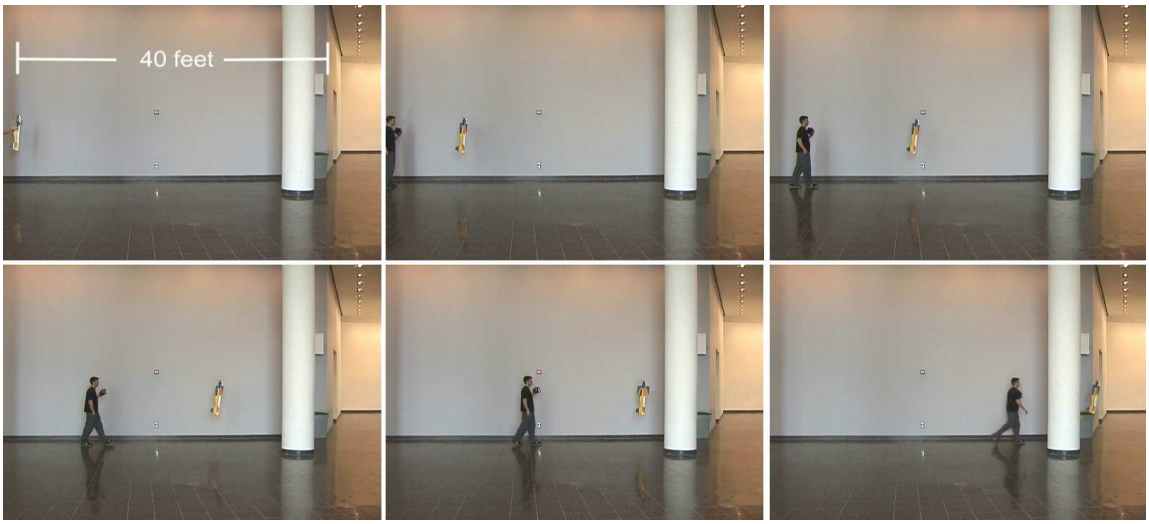

Figure 6.15: The hybrid MAV performs fully autonomous wall following using an ultrasonic and infrared sensor suite.

with high effectiveness and stability.

6.6.2 Evasive Wall Following

The evasive wall following experiments were used to demonstrate the navigational controller's ability to perform wall following on more complex surfaces. Furthermore, the navigational controller should be able to differentiate between a wall cavity and a doorway to some extent. That is, if a wall cavity is deeper than the maximum detection distance of the infrared sensor, the controller will initially declare it as a doorway. However, as it begins to move towards the wall in *traversing mode*, it will detect the wall when it's within the range limitations of the sensors and the controller will reenter *wall following mode*.

The procedure for this experiment will be the same as in the wall following experiments. The aircraft will be released in near hovering orientation and will be under full autonomous control. The goal of the experiment is to maintain a constant 75 cm distance between the tip of the MAV's left wing and the wall. As the plane ap-

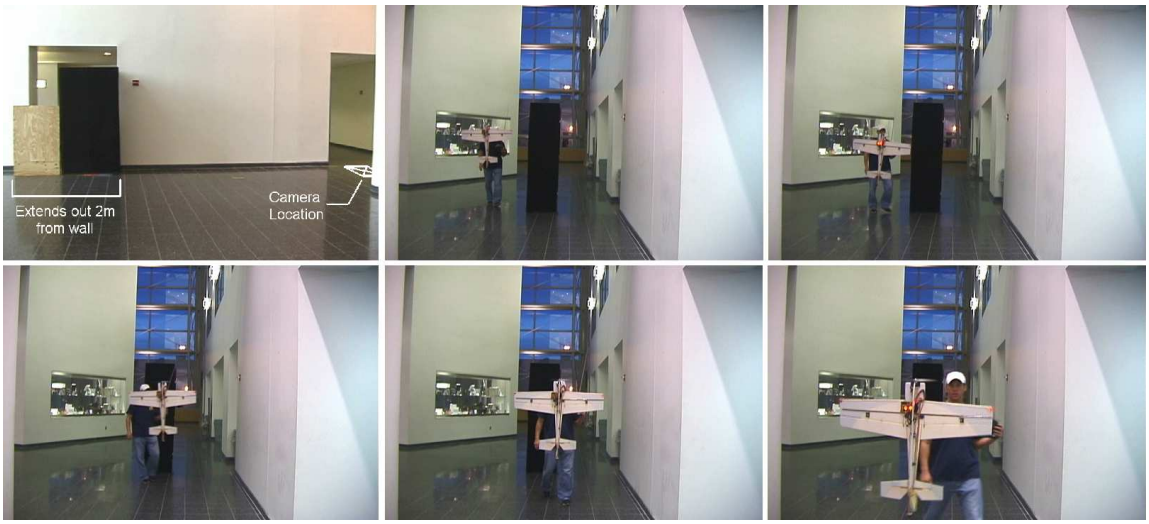

Figure 6.16: The hybrid MAV performs fully autonomous cavity following using an ultrasonic and infrared sensor suite.

proaches the cavity, the data from both the infrared and ultrasonic sensors is critical. The infrared sensor is responsible for determining if the rapid change in distance is a result of a doorway or a wall cavity. Once declared as a wall cavity, the navigational controller will maintain its *wall following mode* and use the ultrasonic sensor to veer the aircraft towards the cavity to maintain that 75 cm distance. The wall used in the experiments and results are shown in Figure 6.16. The perspective of the camera was changed from the previous experiment in order to capture the controller's ability to sustain a constant distance from the wall as it moves along the different surfaces.

6.7 Building Ingress and Reconnaissance Experiment

The final experiment is a culmination of the work presented throughout this thesis. It integrates the quaternion algorithms discussed in Chapter 4, the flight control system and attitude and altitude controllers described in Chapter 5, and the multiple mode, high level controller used to demonstrate wall and cavity following in this chapter. In addition, the navigational controller will also have to detect and move

Figure 6.17: The hybrid MAV autonomously follows the exterior wall of the building until detecting an open passageway. It then traverses the doorway to gather reconnaissance inside the building.

through a doorway to acquire situation awareness[1].

The experimental procedure will be the same as the previous two experiments. The aircraft is released in a near hovering attitude and under full autonomous control, will follow the wall of the building. As it approaches the doorway, the controller will switch from wall following mode to stabilizing mode as discussed in Section 6.5. After it has regained stability in a hover, it will then transition to traversing mode. The MAV will move through the doorway and again stabilize itself in hovering mode. The results of the experiment are shown in Figure 6.17.

[1]Access to the original building shown in Figure 6.1 could not be granted. Therefore, a similar wall and doorway were used in the final experiment.

7. Conclusions and Future Work

7.1 Summary and Achievements

Autonomously flying in near-Earth environments such as caves, tunnels, and urban areas demands a highly maneuverable platform with high endurance and hovering capabilities. The fixed wing hybrid platform was designed with a high thrust-to-weight ratio enabling it to transition into a vertical flight mode. This mode can then be sustained to hover the vehicle using the propeller wash and enlarged elevator and rudder control surfaces. Therefore, the endurance and maneuverability characteristics of fixed wing aircraft are preserved while adding the hovering advantage of helicopters.

To automate the hovering flight mode and the transition into it, a quaternion attitude controller was developed. Typically, quaternions are used for spacecraft attitude control, but were applicable here because of the large angle-of-attack maneuvers of the hybrid platform (i.e. an alternative to Euler angles was needed). It was shown in Chapter 4 that the product of the commanded quaternion and the conjugate of the measured quaternion resulted in the error quaternion. The angular errors about each axis could then be extracted from the error quaternion and used in the flight controller.

The final version of the flight control system consists of a dual processor board that interfaces with the inertial measurement unit. The FCS acquires the measured quaternion from the IMU, calculates the error quaternion and then implements a classical PID controller to regulate the aircraft's attitude. Using this integrated system, autonomous hovering experiments were conducted. The captured flight data showed that the controller's performance exceeded that of an expert human pilot. Further experiments demonstrated that a slightly modified algorithm was able to achieve the

transition from cruise to hover flight autonomously.

The experiments above, however, revealed some additional challenges. The torque rolling effect resulting from the motor's reactive torque was originally thought to be beneficial because it would allow the MAV's bellycam to capture a panoramic view of the target area. However, the plane torque rolled at a rate of 20-25 rpm. This created a dizzying effect when viewing the video from the onboard wireless camera. To counter this, two DC motors with propellers were mounted on each wing tip and oriented such that the thrust vectors had an angular separation of 180 degrees. This created a counter-rotating force and by controlling the speed of the wingtip motors, the torque roll was regulated. It was also realized that there was a need for altitude control. An ultrasonic sensor was mounted on the tail of the aircraft and height-above-ground measurements were used to close the loop for altitude control. Experiments were then conducted which demonstrated the first documented success of fully autonomous hovering of a fixed wing micro air vehicle.

With a robust low level attitude controller, navigational sensing and control techniques could be investigated. For inspiration towards autonomous MAV navigation in near-Earth environments, flying insects and bats stratagems were researched. Optic flow sensors were used previously to demonstrate autonomous collision avoidance and landing, but some limitations of the sensor were revealed. For example, if the sensor's optical axis is moving in a path perpendicular to a flat surface such as a wall, a diverging optic flow field will radiate from the focus of expansion. However, with a wall homogeneous in color and texture, this diverging field will be difficult to detect. Other alternatives were investigated and it was concluded that an ultrasonic and infrared sensor suite is best suited for the building ingress and reconnaissance experiment. The high level control algorithm for this experiment was built on top of the low level controller. The final system was able to achieve a fully autonomous

reconnaissance mission in a near-Earth environment.

7.2 Applications

A hybrid platform that combines the endurance and maneuverability of fixed wing platforms with hovering capabilities of helicopters has a diverse range of potential applications. The small airframe is easily transportable and can be rapidly deployed to perform missions such as reconnaissance, surveillance, bomb damage assessment, and search and rescue. The hybrid MAV can gather reconnaissance in loiter mode high above a target area by performing simple GPS waypoint navigation (see Appendix A). Also, it can autonomously transition into hover mode, descend to a lower altitude, and more easily navigate in cluttered environments.

Furthermore, near-Earth environments also pose severe communication challenges. By developing an onboard flight control system, the integrated system eliminates the risk of communication dropouts with a ground control station. In addition, line of sight to GPS satellites is often occluded and therefore cannot be relied upon. The ultrasonic and infrared sensor suite can be used to perform high level control in the absence of GPS.

7.3 Promising Areas for Future Research

This work presented a well suited platform for flight in near-Earth environments. The primary flight mode can be used in high altitudes where open airspace is vast while the secondary flight mode can be utilized to navigate cluttered areas. Towards fully autonomous flight in this domain, a flight control system was interfaced with an IMU for attitude control and a ultrasonic and infrared sensor suite for navigational control.

While a novel reconnaissance experiment was achieved with the sensor suite, the

integrated system is not capable of autonomously navigating in more cluttered, unknown environments. There are challenges that have not yet been addressed and offer some promising research opportunities including

- *Localization in the absence of GPS.* The hovering experiments conducted in this thesis did not address localization. In indoor environments, the calibrated flight control system can sustain a hover over a small area. However, the MAV would begin to drift when performing experiments outdoors in windy conditions. Typically, this is countered using GPS-based position control, but GPS signals are faint in near-Earth environments and thus an alternative is needed. A proposed solution is to mount a two-dimensional optic flow sensor on the tail, pointing in the downward direction. Measuring the ground's image velocity and integrating may be an effective method for position controlled hovering with GPS.

  Another alternative to this problem could be through simultaneous localization and mapping, or SLAM. SLAM is a revolutionary concept enabling a robot in an unknown environment at an unknown location to simultaneously build a map of the environment and localize itself within the map.

- *Omnidirectional field of view.* In the building ingress and reconnaissance experiments, the sensor suite was oriented specifically for wall following and doorway detection. It was assumed that there would be no obstacles in the MAV's flight path as it moved along the exterior wall of the building. For full autonomous flight in these environments, a 360 degree field of view is desired. SICK laser scanners have a 180 degree scan angle so two of them would be required. However, one sensor is too heavy for miniature UAV payload capacities. Furthermore, the scan plane is two-dimensional and thus a rotation mechanism would also have to be integrated to determine the height of detected obstacles. Hokuyo

laser scanners are significantly lighter, but are less effective when compared to their SICK counterparts. A possible alternative is to position two laser ranging sensors on the belly of the hybrid prototype; one at the nose and one at the tail of the MAV. The aircraft could then complete a single controlled revolution while scanning the environment. This would provide a 360 degree scan of the area while also providing the third dimension (i.e. obstacle height).

- *Sensor performance in the presence of obscurants.* While the SICK laser measurement sensor is a well proven device, little research has been done in determining their effectiveness in the presence of obscurants. In [9], experiments were conducted to demonstrate how fog severely affected the performance of ultrasonic sensors. More recently in [48], experiments showed that laser scanners were affected by fog, rain, and sand. These results must be considered when designing a sensor suite for autonomous flight in near-Earth environments.

Bibliography

[1] Arras, K.O., Persson, J., Tomatis, N., Siegwart, R., "Real-Time Obstacle Avoidance for Polygonal Robots with a Reduced Dynamic Window", *IEEE International Conference on Robotics and Automation*, pp. 3050-3055, Washington, D.C., 2002.

[2] Aufrere, R., Gowdy, J., Mertz, C., Thorpe, C., Wang, C.C., Yata, T., "Perception for Collision Avoidance and Autonomous Driving", *Mechatronics*, Vol. 13, No. 10, pp. 1149-1161, 2003.

[3] Barrows, G., "Mixed-Mode VLSI Optic Flow Sensors for Micro Air Vehicles", *Ph.D. Dissertation*, University of Maryland, College Park, MD, 1999.

[4] Brock, O., Khatib, O., "High-Speed Navigation Using the Global Dynamic Window Approach", *IEEE International Conference on Robotics and Automation*, pp. 341-346, Detroit, MI, 1999.

[5] Centeye, Inc., *Ladybug Optic Flow Microsensor*, *http* : *//www.centeye.com/pages/products/products.html*.

[6] Choi, H., Sturdza, P., Murray, R.M., "Design and Construction of a Small Ducted Fan Engine for Nonlinear Control Experiments", *American Control Conference*, pp. 2618-2622, Baltimore, MD, 1994.

[7] Cole, D., Harrison, A., Newman, P., "Using Naturally Salient Regions for SLAM with 3D Laser Data", *European Conference on Mobile Robots*, Ancona, Italy, 2005.

[8] Corke, P., "An Inertial and Visual Sensing System for a Small Autonomous Helicopter," *Journal of Robotic Systems*, Vol. 21, No. 2, pp. 43-51, 2004.

[9] Danko, T.W., Kellas, A., Oh, P.Y., "Robotic Rotorcraft and Perch-and-Stare: Sensing Landing Zones and Handling Obscurants," *IEEE International Conference on Advanced Robotics*, pp. 296-302, Seattle, WA, 2005.

[10] Ettinger, S.M., Nechyba, M.C., Ifju, P.G., Waszak, M., "Vision-Guided Flight Stability and Control for Micro Air Vehicles", *IEEE/RSJ International Conference on Intelligent Robots and Systems*, pp. 2134-2140, Lausanne, Switzerland, 2002.

[11] Fearing, R., Chiang, K.H., Dickinson, M., Pick, D.L., Sitti, M., Yan, J., "Wing Transmission for a Micromechanical Flying Insect", *IEEE International Conference on Robotics and Automation*, pp. 1509-1516, San Francisco, CA, 2000.

[12] Flynn, A.M., "Combining Sonar and Infrared Sensors For Mobile Robot Navigation", *International Journal of Robotics Research*, pp. 5-14, 1988.

[13] Garratt, M., Chahl, J., "Visual Control of an Autonomous Helicopter," *41st Aerospace Sciences Meeting and Exhibit*, Reno, NV, 2003.

[14] Gavrilets, V., Shterenberg, A., Dahleh, M.A., Feron, E., "Avionics System for a Small Unmanned Helicopter Performing Agressive Maneuvers," *Digital Avionics Systems Conference*, 2000.

[15] Gibson, J.J., "The Ecological Approach to Visual Perception", Houghton Mifflin, 1950.

[16] Grasmeyer, J.M., Keennon, M.T., "Development of the Black Widow Micro Air Vehicle", *39th AIAA Aerospace Sciences Meeting and Exhibit*, Reno, NV, 2001.

[17] Green, W.E., Oh, P.Y., "Optic Flow Based Collision Avoidance on a Hybrid MAV", *IEEE Robotics and Automation Magazine*, 2006 (in press).

[18] Green, W.E., Oh, P.Y., "Autonomous Hovering of a Fixed-Wing Micro Air Vehicle", *IEEE International Conference of Robotics and Automation*, pp. 2164-2169, Orlando, FL, 2006.

[19] Green, W.E., Oh, P.Y., "A MAV That Flies Like an Airplane and Hovers Like a Helicopter", *IEEE/RSJ International Conference on Advanced Intelligent Mechatronics*, pp. 699-704, Monterey, CA, 2005.

[20] Green, W.E., Oh, P.Y., Barrows, G., "Flying Insect Inspired Vision for Autonomous Aerial Robot Maneuvers in Near-Earth Environments", *IEEE International Conference of Robotics and Automation*, pp. 2347-2352, New Orleans, LA, 2004.

[21] Greenwood, D.T., "Principles of Dynamics", Prentice-Hall, Inc., 1988.

[22] Griffiths, S., Saunders, J., Curtis, A., Barber, B., McLain, T., Beard, R., "Maximizing Miniature Aerial Vehicles", *IEEE Robotics and Automation Magazine*, Vol. 13, No. 3, pp. 34-43, 2006.

[23] Guenard, N., Hamel, T.; Moreau, V., "Dynamic Modeling and Intuitive Control Strategy for an X4-Flyer", *IEEE International Conference on Control and Automation*, Vol. 1, pp. 141-146, Budapest, Hungary, 2005.

[24] Guivant, J., Nebot, E., Baiker, S., "Autonomous Navigation and Map Building Using Laser Range Sensors in Outdoor Environments", *Journal of Robotic Systems*, Vol. 17, No. 10, pp. 565-583, 2000.

[25] Hamel, T.; Mahony, R., Chriette, A., "Visual Servo Trajectory Tracking for a Four Rotor VTOL Aerial Vehicle", *IEEE International Conference on Robotics and Automation*, pp. 2781-2786, Washington, D.C., 2002.

[26] Horiuchi, T., Hynna, K., "A VLSI-Based Model of Azimuthal Echolocation in the Big Brown Bat, *Autonomous Robots*, 11(3), pp. 241-247, 2001

[27] Hough, R., "THIS IS NOT A TOY: Micro Air Vehicle Weighs Less, Flies Longer", $http://www.military.com/soldiertech/0,14632,Soldiertech_Wasp,,00.html$, 2005.

[28] Hughes, N., Informal communication, Research Scientist, Analex Corporation, January 2006 - January 2007.

[29] Johnson, E.N., Kannan, S.K., "Adaptive Flight Control for an Autonomous Unmanned Helicopter," Proceedings of the AIAA Guidance, Navigation, and Control Conference, 2002.

[30] Kellog, J., et al "The NRL MITE Air Vehicle", *16th Bristol International Conference on Unmanned Air Vehicle Systems*, Bristol, UK, 2001.

[31] Knoebel, N.B., Osborne, S.R., Snyder, D.O., Mclain, T.W., Beard, R.W., Eldredge, A.M., "Preliminary Modeling, Control, and Trajectory Design for Miniature Autonomous Tailsitters", *AIAA Guidance, Navigation, and Control Conference and Exhibit*, Keystone, CO, 2006.

[32] Lengyel, E., "Mathematics for 3D Game Programming and Computer Graphics", Charles River Media, 2001.

[33] Marek, P., L. Smrcek, "Development of DART MAV Fixed Wing Hover-Capable Micro Air Vehicle," *Advanced Engineering Design Conference*, Prague, CZ, 2006.

[34] McIntosh, S.H., Agrawal, S.K., Khan, Z., "Design of a Mechanism for Biaxial Rotation of a Wing for a Hovering Vehicle", *IEEE/ASME Transactions on Mechatronics*, Vol. 11, No. 2, pp. 145-153, 2006.

[35] Mettler, B., Tischler, M.B., Kanade, T., "System Identification Modeling of a Small-Scale Unmanned Helicopter," *Journal of the American Helicopter Society*, pp. 50-63, 2001.

[36] Michelson, R.C., "The Entomopter," *Neurotechnology for Biomimetic Robots*, The MIT Press, pp. 481-509, 2002.

[37] Mueller, T.J., "Aerodynamic Measurements at Low Reynolds Numbers for Fixed Wing Micro-Air Vehicles," Proc. of the Development and Operation of UAVs for Military and Civil Applications Short Course, Belgium, September 13-17, 1999, published in Rto-EN-9 by NATO, 2000.

[38] Murphy, R., Casper, J., Hyams, J., Micire, M., Minten, B., "Mobility and sensing demands in USAR", *IEEE Industrial Electronics Conference (IECON)*, V1, pp. 138-142, 2000.

[39] Naval Research Laboratory, "MITE", *UAV Info Sheets*, $http://www.nrl.navy.mil/techtransfer/exhibits/uavinfosht.html$.

[40] Nelson, R.C., "Flight Stability and Automatic Control", McGraw-Hill, Inc., 1989.

[41] Nicoud, J.D., Zufferey, J.C., "Toward Indoor Flying Robots", *IEEE/RSJ Int Conf on Robots and Systems*, Lausanne, pp. 787-792, October 2002.

[42] Oh, P.Y., Green, W.E., "Closed Quarter Aerial Robot Prototype to Fly In and Around Buildings", *Int. Conference on Computer, Communication and Control Technologies*, Vol. 5, pp. 302-307, Orlando, FL, 2003.

[43] Ostrander, D., "An Engineer's Approach to Quaternions", *Internal Seminar at Martin Marietta*, 1986.

[44] Peremans, H., Muller, R., "A Comprehensive Robotic Model for Neural and Acoustic Signal Processing in Bats", *IEEE International EMBS Conference on Neural Engineerings*, pp. 458-461, Capri Island, Italy 2003.

[45] Phillips, W.F., Hailey, C.E., "Review of Attitude Representations Used for Aircraft Kinematics" *Journal of Aircraft*, Vol. 38, No. 4, pp. 718-737, 2001.

[46] Pornsin-sirirak, T.N., Lee, S.W., Nassef, H., Grasmeyer, J., Tai, Y.C., Ho, C.M., Keennon, M., "MEMS Wing Technology for a Battery-Powered Ornithopter", *The 13th IEEE Annual International Conference on MEMS*, pp. 709-804, Miyazaki, Japan, 2000.

[47] Saripalli, S., Montgomery, J.F., Sukhatme, G.S., "Vision-based Autonomous Landing of an Unmanned Aerial Vehicle", *IEEE International Conference on Robotics and Automation (ICRA)*, pp. 799-2804, Washington, D.C., 2002.

[48] Sevcik, K., "Laser Scanner Characterization and its Application to UAV Terrain Mapping in the Presence of Obscurants", *M.S. Thesis*, Drexel University, Philadelphia, PA, June 2007.

[49] Sharp, C.S., Shakernia, O., Sastry, S.S., "A Vision System For Landing an Unmanned Aerial Vehicle" *IEEE International Conference on Robotics and Automation (ICRA)*, pp. 1720-1727, Seoul, Korea, 2001.

[50] Shim, D.H., Chung, H., Sastry, S.S., "Conflict-Free Navigation in Unknown Urban Environments" *IEEE Robotics and Automation Magazine*, Vol. 13, No. 3, pp. 27-33, 2006.

[51] Simons, M., "Model Aircraft Aerodynamics", Special Interest Model Books Ltd., 2002.

[52] Srinivasan, M. V., Zhang, S.W., Lehrer, M., and Collett, T.S., "Honeybee Navigation En Route to the Goal: Visual Flight Control and Odometry", The Journal of Experimental Biology, pp 237-243, 1996.

[53] Srinivasan, M.V., Chahl, J.S., Weber, K., Venkatesh, S., Nagle, M.G., Zhang, S.W., Robot Navigation Inspired By Principles of Insect Vision, *Robotics and Autonomous Systems*, Vol 26, pp. 203–216, 1999.

[54] Stachniss, C., Burgard, W., "An Integrated Apporach to Goal-Directed Obstacle Avoidance Under Dynamic Constraints for Dynamic Environments", *IEEE International Conference on Intelligent Robots and Systems*, pp. 508-513, Lausanne, Switzerland, 2002.

[55] Steltz, E., Wood, R.J., Avadhanula, S., Fearing, R.S., "Characterization of the Micromechanical Flying Insect by Optical Position Sensing", *IEEE International Conference on Robotics and Automation*, pp. 1252-1257, Barcelona, Spain, 2005.

[56] Stone, R.H., "Control Architecture for a Tail-Sitter Unmanned Air Vehicle", *5th Asian Control Conference*, vol. 2, pp. 736-744, 2004.

[57] Tammero, L.F., Dickinson, M.H., "The influence of visual landscape on the free flight behavior of the fruit fly Drosophila melanogaster", *Journal of Experimental Biology*, v205, pp. 327-343, 2002.

[58] Tammero, L.F., Dickinson, M.H., "Collision Avoidance and Landing Responses are Mediated by Separate Pathways in the Fruit Fly, Drosophila Melanogaster", *Journal of Experimental Biology*, v205, pp. 2785-2798, 2002.

[59] Wertz, J.R., "Spacecraft Attitude Determination and Control", D. Reidel Publishing Co., 1978.

[60] Whiteside, T.C., Samuel, G.D., "Blur Zone" *Nature*, 225:94-95, 1970.

[61] Wie, B., Weiss, H., Arapostathis, A., "Quaternion Feedback Regulator for Spacecraft Eigenaxis Rotations", *Journal of Guidance, Control, and Dynamics*, vol. 12, no. 3, pp. 375-380, 1989.

[62] Zufferey, J.C., Floreano, D. "Fly-inspired Visual Steering of an Ultralight Indoor Aircraft", *IEEE Transactions on Robotics*, Vol. 22, No. 1, pp. 137-146, 2006.

[63] Zufferey, J.C., Floreano, D. "Toward 30-gram Autonomous Indoor Aircraft: Vision Based Obstacle Avoidance and Altitude Control", *IEEE International Conference on Robotics and Automation*, pp. 2594-2599, Barcelona, Spain, 2005.

Appendix A. GPS Waypoint Navigation

A.1 Interpreting the GPS Data

The National Marine Electronics Association (NMEA) has developed a standard for all GPS devices. The string containing the most relevant information is the $GPRMC data line which is the Recommended Minimum Specific GPS/TRANSIT Data. The $GPRMC data string contains 12 pieces of information separated by commas within the string:

1. Time Stamp
2. Validity: A for OK, V for invalid
3. Current Latitude
4. North or South
5. Current Longitude
6. East or West
7. Speed (in knots)
8. True Course
9. Date Stamp
10. Variation
11. East or West
12. Checksum

The most useful pieces of data are the latitude (3), longitude (5), and true course (8). The true course is the current heading of the aircraft in degrees and is measured clockwise from the north direction. If the MAV is heading east, for example, then the true course would be equal to 90 degrees. This single value saves an enormous amount of computation. Otherwise, a vector would have to be drawn from the previous latitude/longitude point to the current latitude/longitude point. The angle it forms with the north direction would then have to be calculated.

The waypoint heading is not given in the $GPRMC data string and must be calculated. Before determining the bearing to the next waypoint, the distance between the current

location of the aircraft and the waypoint must be determined using the great circle distance formula

$$d = cos^{-}1(sin(Lat1)xsin(Lat2) + cos(Lat1)xcos(Lat2)xcos(Lon1Lon2)) \tag{A.1}$$

where (Lat1,Lon1) and (Lat2,Lon2) are the latitude and longitude coordinates of the current and next waypoints, respectively. To calculate the bearing to the next waypoint, the classical bearing formula is used

$$d = cos^{-}1(\frac{sin(Lat2) - sin(Lat1)xcos(d)}{cos(Lat1)xsin(d)}) \tag{A.2}$$

where d is the great circle distance. One last problem remains, however, as the angle yielded will take the counter-clockwise direction as positive. To change the positive direction to clockwise in order to coincide with the true heading value (8), the following two lines of code are added to the algorithm

$$\begin{aligned} if \quad & (sin(Lon2 - Lon1) > 0.0) \\ & waypointHeading = 360.0 - waypointHeading * (180.0/Pi); \\ else & \\ & waypointHeading = -waypointHeading * (180.0/Pi); \end{aligned}$$

A.2 Turning Algorithm

Now that the current heading of the MAV and the heading to the next waypoint are known, the turning control signal can now be determined to head towards the next waypoint (i.e. which way and by how much the MAV should turn). A simple algorithm can be used which says that if the aircraft heading is less than the waypoint heading, turn right; otherwise turn left. Figure A.1 shows a graphical representation of this algorithm. Both the

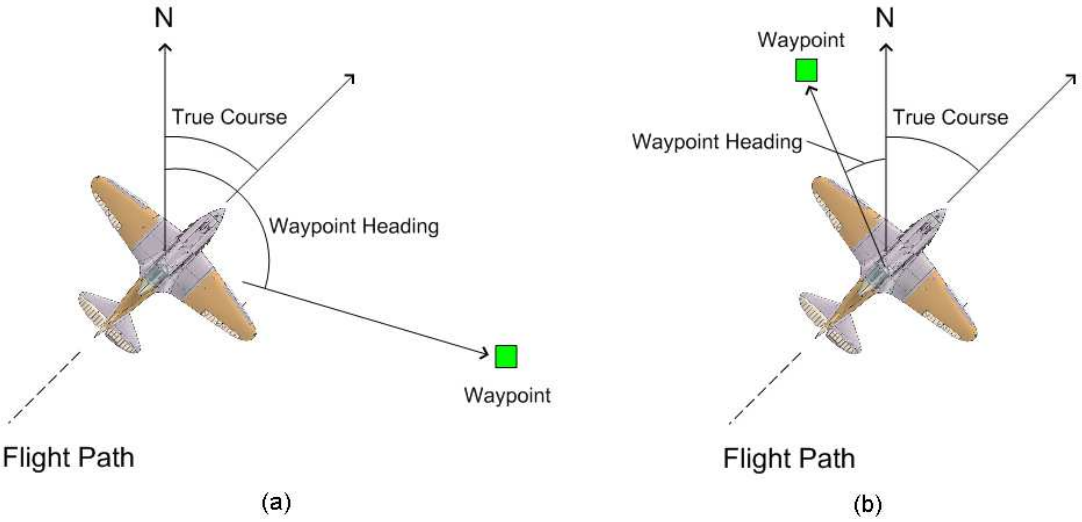

Figure A.1: (a) Subtracting the true course heading from the waypoint heading will give the bearing to the next waypoint. (b) The same formula will get the MAV to the next waypoint, but not before turning in a complete circle.

waypoint heading angle and the true course angle are measured from the north direction.

Intuitively, it is obvious the aircraft should turn right in Figure A.1a and left in Figure A.1b. However, with the algorithm from above, the plane will get to the waypoint but not before flying in a complete circle. The algorithm used instead is a simple proportional controller using the error between the aircraft heading and the waypoint heading. However, a limitation is imposed on the error to confine the MAV into taking the shortest possible turn (in terms of degrees) to the next waypoint. That is, it will not make a 300 degree right turn when it can make a 60 left turn to head toward the next waypoint.

$$if(error >= 180) error = error - 360;$$

$$if(error <= -180) error = 360 + error;$$

An experiment was implemented using a Garmin 18 5Hz GPS receiver. The receiver was interfaced with an earlier version of the dual processor flight control system. The experiment was conducted over a large field and a path was mapped out a priori consisting

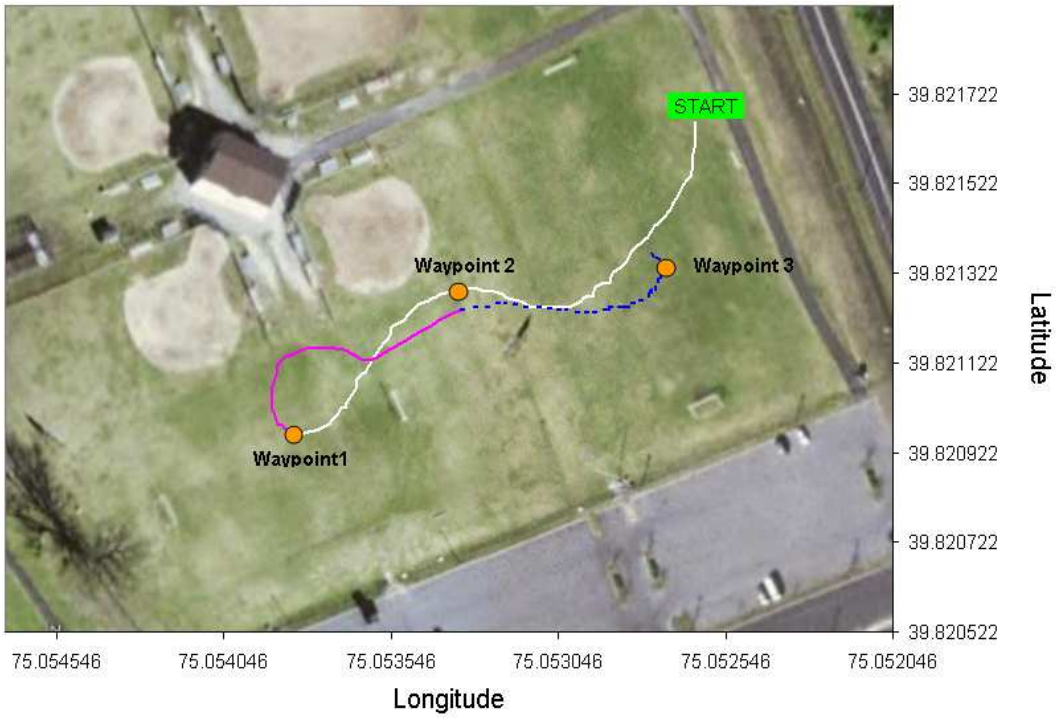

Figure A.2: A Garmin GPS 18 5Hz receiver is interfaced with the FCS to perform autonomous waypoint navigation.

of three waypoints. The plane was hand launched and manually flown to cruise altitude. The expert human pilot would then flick the auto/manual switch on the transmitter to enable the autonomous GPS waypoint navigation. The elevator was set in the neutral position to keep the aircraft at a relatively constant altitude and the proportional controller sent control signals to the rudder in order to steer the aircraft to the next waypoint. The path the MAV followed during the experiment is shown in Figure A.2.

Vita

Education

Ph.D. Mechanical Engineering, 2007, Drexel University, Philadelphia, PA

M.S. Mechanical Engineering, 2006, Drexel University, Philadelphia, PA

B.S. Mechanical Engineering, 2002, Drexel University, Philadelphia, PA

Research Experience

Graduate Research Assistant, DASL, Drexel University, 2002-2007

Teaching Experience

Instructor/Teaching Assistant, MEM Dept., Drexel University, 2002-2007

Awards and Honors

Lockheed Martin George Law Fellowship (1 year), 2005

Koerner Fellowship, Drexel University (1 year), 2004

Honorable Mention, NSF Graduate Research Fellowship, 2003, 2004

Deans Fellowship, Drexel University (5 years), 2002

A.J. Drexel Scholarship, Drexel University (5 years), 1997

Publications

The following is a selective list of 18 refereed conference papers, journals, and book chapters in the areas of control systems, sensing, collision avoidance, and aircraft design.

1. Green, W.E., Oh, P.Y., ‘‘The Integration of a Multimodal MAV and Biomimetic Sensing for Autonomous Flight in Near-Earth Environments’’, Advances in Unmanned Aerial Vehicles, ed. K. Valavanis, Springer 2007.
2. Green, W.E., Oh, P.Y., ‘‘Optic Flow Based Collision Avoidance on a Hybrid MAV’’, IEEE Robotics and Automation Magazine, (in press).
3. Oh, P.Y., Green, W.E., ‘‘CQAR: Closed Quarter Aerial Robot Design for Reconnaissance, Surveillance and Target Acquisition in Urban Areas’’, Intl. Journal of Computational Intel., V1, No. 4, pp. 353-360, 2004.
4. Oh, P.Y., Green, W.E., ‘‘A Mechatronic Kite and Camera Rig to Rapidly Acquire, Process and Distribute Aerial Images’’, IEEE/ASME Transactions on Mechatronics, Vol. 9, No. 4, pp. 671-678, December 2004.
5. Green, W.E., Oh, P.Y., Barrows, G., ‘‘Flying Insect Inspired Vision for Autonomous Aerial Robot Maneuvers in Near-Earth Environments’’, IEEE ICRA, New Orleans, LA, pp. 2347-2352, April 2004.
6. Green, W.E., Oh, P.Y., ‘‘An Aerial Vision Platform for Acquiring Situational Awareness’’, CCCT, Orlando, FL, pp. 289-295, July 2003.